climate change initiative

European Space Agency

Algorithm Theoretical Basis Document Version 0 (ATBDv0)

glaciers cci

Prepared by: Glaciers_cci consortium

Contract: 4000101778/10/I-AM
Name: Glaciers_cci-D2.3_ATBDv0
Version: 1.0
Date: 02.04. 2012

Contact:
Frank Paul
Department of Geography
University of Zurich
Winterthurerstr. 190
CH-8057 Zurich
frank.paul@geo.uzh.ch

Technical Officer:
Stephen Plummer
ESA ESRIN

University of Zurich UZH

UNIVERSITY OF OSLO

University of BRISTOL

GAMMA

enveo

UNIVERSITY OF LEEDS

Document status sheet

Version	Date	Changes	Approval
0.1	07.07. 2011	Initial draft	
0.2	28.09. 2011	First compilation	
0.3	20.10. 2011	Revised compilation	
0.4	09.11. 2011	Revised compilation	
0.5	27.11. 2011	Revised version	
0.6	03.12. 2011	Final version for approval by S. Plummer	F. Paul
0.7	25.03. 2012	Corrected version for final consortium review	
1.0	02.04. 2012	Final feedback from consortium included	

The work described in this report was done under ESA contract 4000101778/10/I-AM. Responsibility for the contents resides with the authors that prepared it.

Author team:
Frank Paul (GIUZ), Andreas Kääb, Christopher Nuth, Torborg Heid (GUIO), Thomas Nagler, Helmut Rott, Kilian Scharrer (Enveo), Andrew Shepherd, Francesca Ticconi (SEEL), Tazio Strozzi (Gamma)

Glaciers_cci Technical Officer at ESA:
Stephen Plummer

Contents

1. Executive Summary

This document is the Algorithm Theoretical Basis Document version 0 (ATBDv0) of the Glaciers_cci project. It focuses on the algorithms to create the three products glacier area, elevation change, and velocity. For each of the products it describes the problems that the algorithms address, the scientific background and mathematics of the algorithms, their expected or known accuracy and performance, input and output data, error budgets, and practical considerations for their implementation.

For glacier area, the document concentrates on band-ratio based algorithms. These were shown in a number of previous studies to be most robust and highly automatic. For glacier elevation change, radar and lidar altimeter based methods are included, as well as DEM differencing. For DEM differencing, the document focuses on the co-registration of the DEMs as this is identified as the major generic error source for this kind of elevation change measurements. For glacier velocities, the document focuses on tracking-based algorithms (SAR and optical) as these have the highest potential for automation and large-scale applicability. Radar interferometry is applied for validation purposes within the Glaciers_cci project and thus shortly explained as well.

2. Introduction

2.1 Purpose of this document

This is the Algorithm Theoretical Basis Document version 0 (ATBDv0) of the Glaciers_cci project. It is the third deliverable of Task 2 (D2.3). The ATBD gives an overview of potential algorithms to generate FCDRs and the derived ECV data products required by the end-users. The ATBDv0 is a 'light' version of the ATBD 'providing a high level description of the scientific background to an algorithm and a functional description of what the algorithm does' (SoW).

This document explains, discusses and reviews satellite-based remote sensing methods for glacier area mapping, glacier elevation change and glacier surface velocity measurements. Since these three tasks are very different in terms of input data, processing and results, the document is mainly structured along these three tasks, and Glaciers_cci product types. Each of the according chapters gives:

- a scope of the problem that the algorithm addresses,
- the scientific background,
- description of processing chains and algorithms,
- a review of expected accuracy and performance differences between the algorithms listed, and others,
- the type and specifications of the input data required,
- the output data,
- error budget estimates, and
- practical considerations for implementation.

2.2 Background to the approaches

Using satellite data to derive **glacier outlines** over large regions or on a global scale from automated image classification techniques is a key recommendation (Tier 5) of the tiered glacier monitoring strategy of GTN-G (e.g. Haeberli, 2006). In view of the demand to further transform these outlines (contiguous ice masses) into a glacier inventory (individual glaciers with topographic attribute information), the application of modern geoinformatic techniques (using a GIS and DEMs) is required for efficient data processing (e.g. Kääb et al., 2002; Paul et al., 2002). With the free availability (and in the case of Landsat already accurately orthorectified) satellite data from USGS combined with the free DEMs from SRTM, the ASTER GDEM, or national DEMs (NEDs), the principle accomplishment of this task is feasible (Paul, 2010). As clearly expressed in the URD (Glaciers_cci, 2011a), the most important task is to complete the global glacier inventory. Since the required technical specifications for the sensors used is described in the DARD (Glaciers_cci, 2011c), we here focus on the data processing algorithms and what is required to understand their physical background. The major post-processing steps are detailed in section 3.5.

Multi-temporal satellite elevation data provides an effective approach to continuously monitor glacier surfaces. Glacier **elevation changes** are often used to characterize glacier mass balance variations, especially in remote areas where field measurements are difficult. Indeed, it is the large spatial and temporal coverage of satellite-derived elevation changes that

increase the desirability and potential of this method for glacier monitoring. Elevation change of a glacier surface is, however, not directly transferrable into mass changes because the surface change is the result of both surface mass balance processes (accumulation, ablation or firn layer variability) and dynamical ice flux components: general downward flow, submergence in the accumulation area, and emergence in the ablation area. This makes the interpretation of short-term glacier elevation changes complicated. Therefore, the products created by Glaciers_cci will focus on uncorrected elevation change measurements as requested in the URD (Glaciers_cci, 2011a). However, a mean elevation change value per glacier entity is a product that is also requested and will thus be generated as well. Elevation changes are derived by two general approaches; (1) repeat altimetry (radar or lidar) with a focus on repeat track measurements that have small spatial offsets, and (2) DEM differencing with a focus on the pre-processing of the DEM pairs. In both approaches, the detection of bias is essential and required corrections should be determined. The details for each of the two methods are presented in chapters 4 and 5, respectively.

The generation of **glacier velocity** measurements from repeat satellite data is highly desirable in the glaciological community to better characterize glacier dynamics and potential changes in the dynamic behaviour of glaciers. Since in-situ measurements of velocity are limited in space due to logistical constraints of deploying GPS instruments, satellite derived velocities provide an significantly larger spatial data set, both in terms of the number of glaciers that can be measured but also providing the spatial distribution of velocity within an individual glacier. Tracking methods based on repeat optical or SAR satellite images, and radar interferometry are efficient approaches to derive surface displacements on glaciers. Tracking algorithms applied include normalized cross-correlation, cross-correlation operated in the Fourier domain, least squares matching, phase correlation, orientation correlation, etc. In addition to the performance of the algorithms themselves, their implementation (e.g. search template sizes, search windows, search strategy), data pre-processing (e.g. interest operators) and post-processing of the results (e.g. outlier filters) are of equal importance.

2.3 General remarks

A major guideline for the algorithms and processing chains included in this document is a high potential for automation. However, it should be mentioned that in many cases at least some degree of human interaction is required in order to derive glaciologically meaningful and reliable data of glacier areas, elevation changes and velocities. For instance, automatic glacier outlines have to be checked and corrected for debris-covered glacier parts, or some remaining velocity outliers have to be corrected manually, depending on the purpose of application. In these cases, the goal of the algorithms and processing chains included here is to minimize the degree of human interaction to support this interaction as much as possible. In the round robin, some of these manual processes are evaluated for their accuracy as well.

3. Glacier area

3.1 Introduction

Compared to the use of aerial photography for glacier mapping in the World Glacier Inventory (WGMS, 1989), the application of satellite data has the special advantage of the much larger area covered combined with a sensor in the shortwave infrared (SWIR) that allows the automated classification of clean to slightly dirty (i.e. optically thin) glacier ice (e.g. Paul and Kääb, 2005). Of course, the spatial resolution is an order of magnitude lower (10 to 30 m) compared to aerial photography (about 1 m), but the smallest glacier entitiy that can still be called glacier (about 0.01 km^2 in size according to Paul et al. (2009)) can still be mapped under good conditions (Andreassen et al., 2008). So in times of rapidly shrinking glaciers the gain in processing speed is really an asset. Under special circumstances it might even be possible to map nearly all glaciers of an entire mountain range within a few weeks, like for the Alps in the summer of 2003 (Paul et al., in revision) or for the western Himalaya within 3 years (Frey et al., in revision). Compared to the 30-year time span that was required to map all glaciers in the Alps in the previous inventory (Zemp et al., 2008), this is an important benefit, in particular for large scale hydrologic modelling (e.g. Zappa and Kan, 2007; Huss, 2011). So the most efficient means for repeat mapping of glaciers on a global scale is indeed provided by satellite data.

So far,'satellite data' refers to optical data with a number of multispectral bands in various parts of the electromagnetic spectrum (from the visible to the thermal infrared). Though the SWIR band (e.g. TM5 on Landsat) allows discrimination of snow from clouds, none of the optical bands can penetrate through clouds, i.e. apart from seasonal snow cover, clouds are a major bottleneck in the operational application of satellite data for glacier mapping. If a scene has clouds over the glaciers to be analysed, the scene has to be excluded or can only partly be processed. In the latter case, the use of multi-temporal datasets might help, as usually the clouds in two, otherwise very good images are often not located at the same position. This gives the possibility to merge two data sets to get a (more or less) cloud free coverage (e.g. Le Bris et al., 2011). Indeed, when cloud boundaries cover only parts of a glacier the issue can get rather complicated as the outline of one glacier entity might then refer to different years.

The other bottleneck is debris cover on glaciers that has the same spectral properties as the surrounding terrain and can thus not be discriminated from multispectral data alone. Though a number of techniques for debris-cover mapping have been developed in the recent past (e.g. Paul et al., 2004; Shukla et al. 2011), they all require manual post-processing to give sufficiently accurate results. With microwave data cloud penetration is not a problem, but the dielectric properties of ice and snow are not sufficiently different from other terrain to precisely map glacier extent automatically (e.g. Hall et al., 2000). However, the recent application of coherence images from ALOS PALSAR acquired during the summer months have revealed new possibilities to precisely delineate debris-covered glaciers in regions where image contrast is poor (e.g. Strozzi et al., 2010; Frey et al., in press). For a part of Alaska even the entire delineation of glaciers from PALSAR coherence worked largely automatically (Atwood et al., 2010).

So in regard to clouds and debris-cover there is still potential for important algorithm improvements by considering also microwave data. When seasonal snow is present (and

hiding parts of the glacier perimeter), the only feasible option is to use a scene from another date. In some regions of the world this reduces the number of useful satellite scenes considerably (Paul et al., 2011), but in our experience product quality would otherwise be below acceptable standards.

Indeed, the best algorithms for automated classification of snow and ice produce results that are only different at the level of individual pixels (e.g. Paul and Kääb, 2005; Paul and Hendriks, 2010). The quality of the generated outlines does thus largely depend on the experience and qualification of the analysts responsible for the post-processing. Errors introduced by the wrong interpretation of debris cover, snow fields, or glacier parts in shadow are much larger than differences in the algorithms (Gjermundsen et al., 2011). For this reason a major task towards improved product quality and consistency is the generation of illustrated guidelines for the analyst. This should not exclude further advances in the automated classification and hence reduce the required post-processing, but in the end the analyst has to decide whether a glacier outline is acceptable or not. Statistical tests or standard error assessments do not provide this information. So the round robin for the glacier area product has a special focus on this issue.

3.2 Scientific background

In the following we focus on the main-processing stage, i.e. the glacier mapping algorithm to be applied. To find a most suitable algorithm, one has to be aware of what a glacier looks like, i.e. the spectral properties of the typical surface characteristics as seen from space. As glaciers result from the metamorphosis and compression of snow, their spectral properties are very similar to snow (e.g. Hall et al., 1988). Of course, dust, debris and liquid water on the surface alter the spectral response and can be found nearly anywhere on the glacier (Fig. 3.1). In this regard the spectral information of a satellite image pixel (in the 10-130 m range) is in most cases a mixed signal with the respective deviations from a pure (laboratory) signal. In Fig. 3.2a and 3.2b a comparison of the spectral reflectance for snow of varying grain size from theoretical considerations (Dozier, 1989) with field-based measurements from Qunzhu et al. (1983) is shown. Besides the high reflectance of snow in the visible part (VIS) of the spectrum (independent of grain size), the strong reflectance drop in the near infrared (NIR) can be seen (Fig. 3.2a). The dependence of the reflectance on grain size is very high in the NIR (with smaller grains having the higher reflectance), indicating the potential to map snow grain size from the reflectance value in this spectral range. In the SWIR the reflectance increases slightly again and is still strongly dependent on grain size. On the other hand, clouds still have a rather high reflectance in the SWIR and thus can be easily discriminated from snow with a SWIR sensor (Dozier, 1989).

In a spectral sense, glacier ice can be seen as snow with very large grain sizes, so that the spectral reflectance curve of pure glacier ice follows the curve of snow very closely. However, impurities in and on the ice (e.g. dust and soot) shift the curve of spectral reflectance downwards (Fig. 3.2b). The spectral reflectance curve of debris is based on the lithology of the material and can thus have any shape.

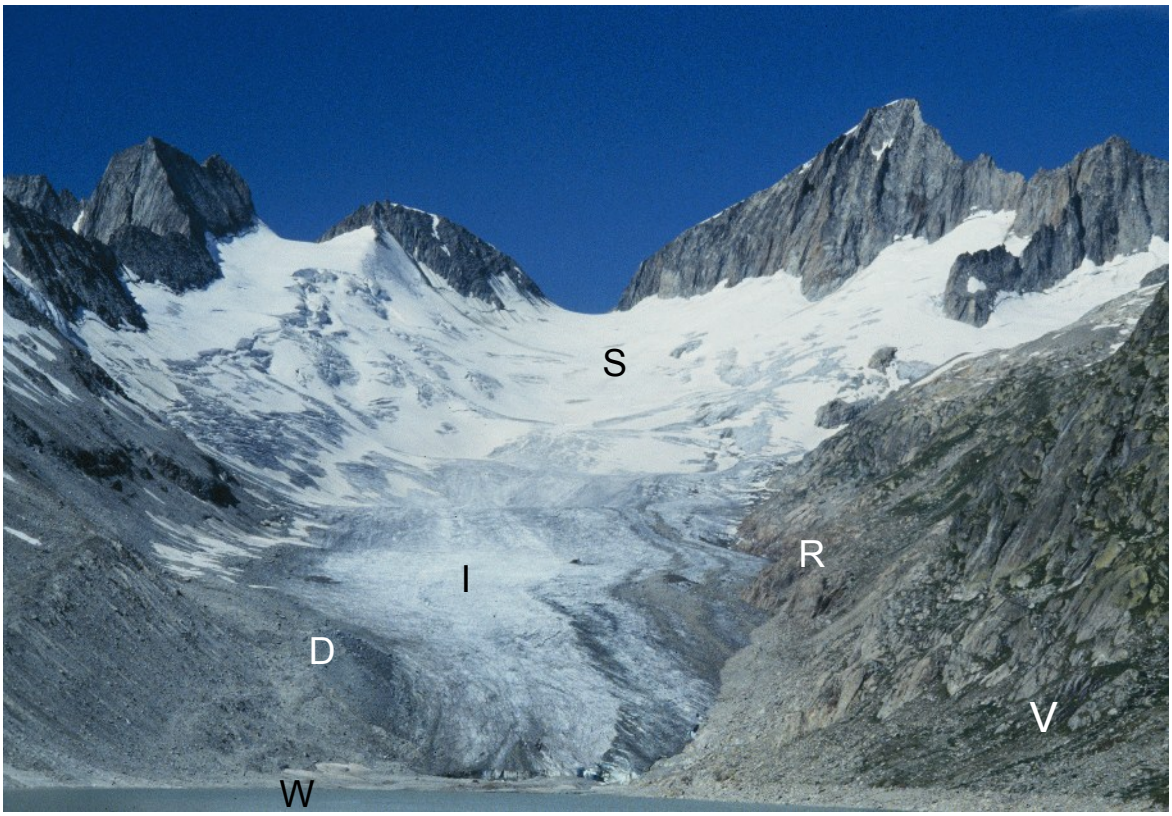

Fig. 3.1: Oberaarglacier in Switzerland. The picture illustrates the spectral reflectance of bare ice (I), debris-covered ice (D), snow (S), rock (R), vegetation (V) and turbid water (W) in the visible part of the spectrum. A spectral discrimination of the debris cover on the glacier and from the lateral moraine (in the lower left of the image) is not possible.

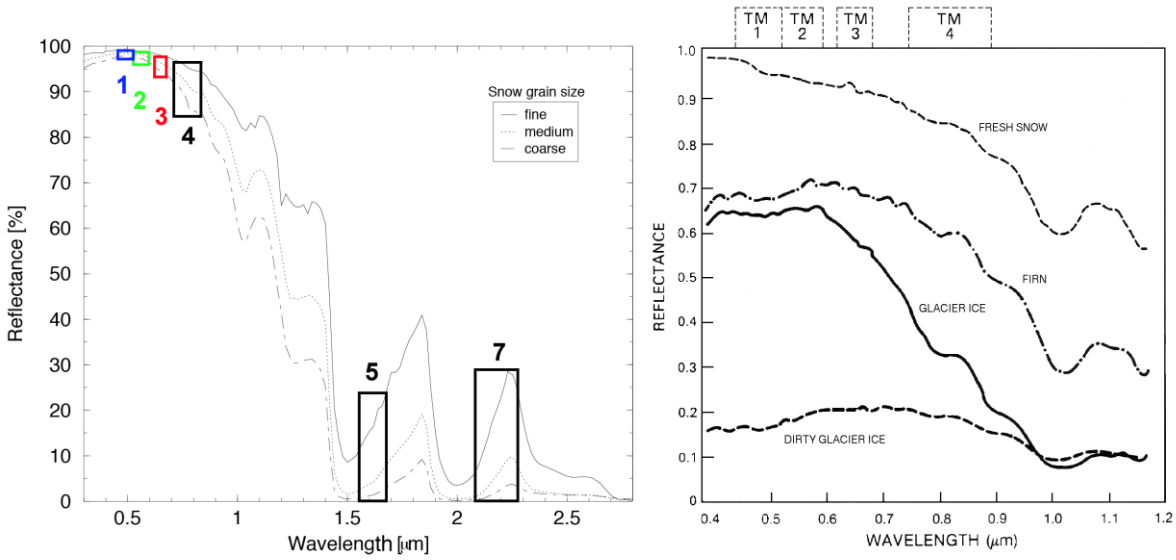

Fig. 3.2: Modelled spectral reflectance curves of snow with three different grain sizes and position of TM spectral bands (left). Spectral reflectance of snow, firn, ice and dirty glacier ice according to field measurements (right). The data for the left figure are taken from the ASTER spectral library (JPL , 2002), the right figure is adapted from Hall et al. (1988).

Apart from the above components, shadow on the glacier surface alters its spectral response as atmospheric scattering (brightening these regions) is dependent on wavelength. The same is true for thin clouds (cirrus or fog). A high impact on the absolute reflectance values results from illumination differences due to the topography (i.e. the sun - target - sensor geometry) and to a lesser extent from atmospheric conditions. The use of absolute reflectance values for glacier classification therefore requires topographic and atmospheric corrections (e.g. Rott and Markl, 1989).

The spectral reflectance of glaciers in the individual spectral bands is shown in Fig. 3.3 for the Landsat TM sensor (ASTER and SPOT look similar, but do not have a TM band 1 equivalent band in the blue part of the spectrum) and a typical high-mountain region (cf. Paul, 2002). In agreement with the spectral curves shown in Fig. 3.2, the high reflectance over snow in the VIS to NIR (VNIR) bands (TM1, TM2, TM3, TM4) and the lower reflectance over glacier ice can be seen. In the NIR the low reflectance of water and the higher reflectance of vegetation becomes obvious. The very low reflectance of glacier ice and snow in the SWIR can be seen in TM 5 and TM 7 (not shown here). The reflectance of water is also very low and vegetation and rock have a very high surface reflectance. Finally, in the thermal infrared band (TIR) of TM6 the digital numbers (DNs) depend on the temperature of the surface. They are thus not reflectance values but characterize surface emission. The higher the temperature is, the higher the DNs are and vice versa. Hence, glacier ice and snow (at the melting point) have rather low DNs, whereas sunlit mountain slopes are already warmed at the time of image acquisition and appear much brighter. Terrain in shadow is also cooler and thus appears somewhat darker. Most noticeable is the much coarser resolution (120 m) of TM band 6 (ETM+: 60 m, ASTER: 90 m) compared to the other bands.

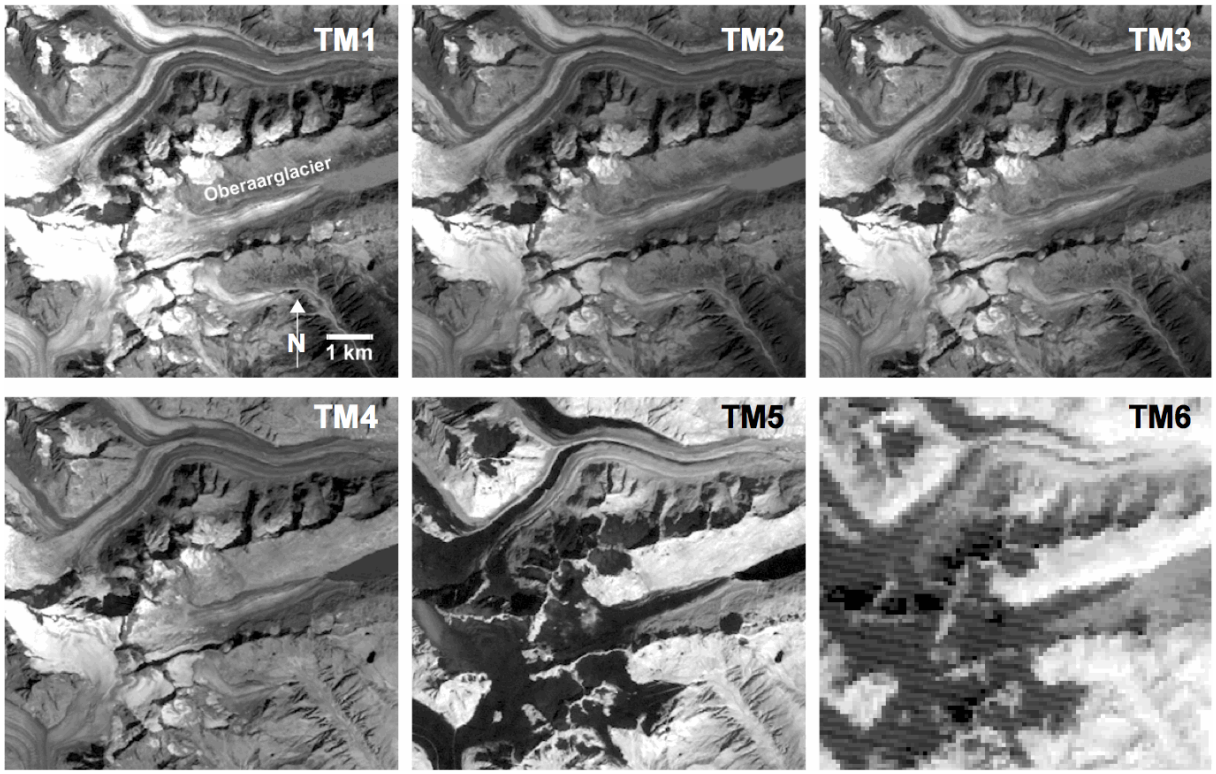

Fig. 3.3: Visualization of reflectance values in TM bands 1 (TM1) to 6 (TM6) for a subset of a Landsat TM scene around Oberaarglacier in the Swiss Alps (image size is 9.5 km by 9 km).

The thermal band was proposed in various publications as being useful to delineate debris-covered glacier parts, due to the cooling of the rocks on the surface from the underlaying ice (e.g. Shukla et al., 2011 and references therein). However, we are sceptical that this really works for alpine type glaciers. In most cases some bare ice is included in the related mixed pixels (strongly reducing the temperature of the respective pixel) and the effect of differential thermal heating of the rocks by the sun is rather obvious. However, in the case of a (thin) volcanic ash layer and comparably large glaciers (e.g. the Vatnajøkull icecap on Iceland), the thermal band could be used as an alternative to the SWIR band (Bishop et al., 2004), i.e. all glacier ice and snow has a similar low reflectance (independent of the ash cover).

The different spectral responses of ice and snow compared to other surface types (water, rock, vegetation) or clouds, allows them to be classified automatically (see section 3.3). However, in the post-processing stage omission and commission errors have to be corrected (e.g. adding debris cover or glacier parts in shadow, removing lakes). For this purpose contrast enhanced RGB composites are created from the different spectral bands that are used in the background to guide the correction process (see examples in Fig. 3.4). The most useful combinations in this regard are the classical band 3, 2, 1 (natural colours with TM) and 4, 3, 2 (false colour infrared) combination, as well as the band 5, 4, 3 false colour composite (FCC). While the 321 composite is best suited to identify ice and snow in shadow, the 432 composite has best contrast to identify water surfaces, vegetation trimlines, snow cover and drainage divides in the accumulation region. The 543 FCC allows a clear identification of glaciers (they appear in light blue), helps to identify clouds (which appear white) and provide good contrast for debris cover identification. Thus all three band combinations are useful and should be generated in the pre-processing stage from the raw data using digital image processing software.

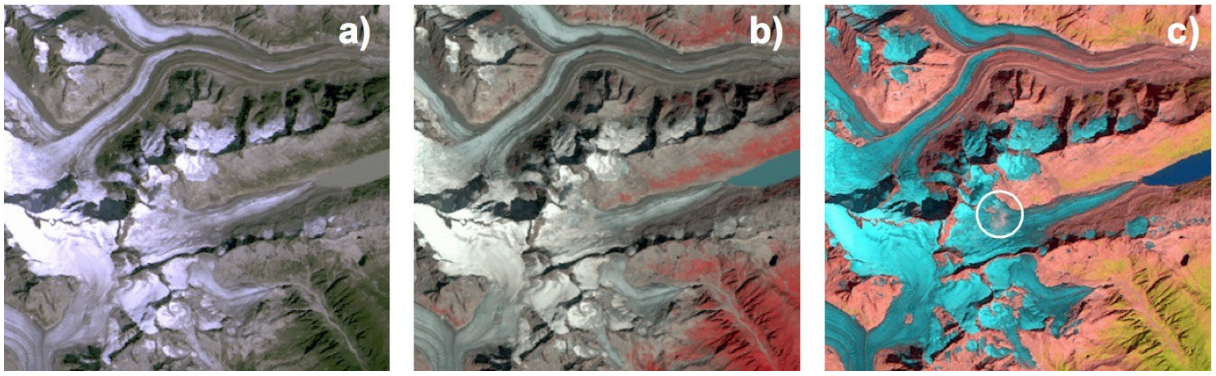

Fig. 3.4: RGB composites of the region shown in Fig. 3.3 with a) bands TM 3, 2, and 1, b) 4, 3, 2, and c) 5, 4, 3. The small cloud is only visible in this image (white circle).

The algorithms presented in the following sections are based on raw DNs, i.e. they are not converted to top-of-atmosphere (TOA) reflectance values or corrected for topographic or atmospheric effects. The main reasons are: (a) the latter requires a DEM that has no artefacts and is perfectly aligned with the satellite image. This is nearly impossible to achieve as the registration error of satellite images is seldom better than +/- 1 pixel (RMSE), in particular in steep high-mountain terrain. Without a proper coregistration, artefacts are introduced to the reflectance values during topographic correction (e.g. due to over correction), which reduce the quality of the classification. At the same time a 'perfect' topographic correction would

remove subtle reflectance differences that are important to classify glaciers accurately (e.g. in shadow). (b) Atmospheric correction requires a number of atmospheric parameters being available (at least visibilities at different altitudes) which is often not the case in remote regions where glaciers are found. (c) The most accurate mapping methods are based on band ratios. They partially normalize topographic and atmospheric conditions within a scene and thus work without this pre-processing step. Using TOA instead of DNs does not improve the classification so this conversion is not required either (Paul, 2001).

3.3 Description of available algorithms

A wide range of glacier classification methods have been developed and compared in the past two decades (e.g. Albert, 2002; Paul et al. 2003; Sidjak and Wheate, 1999). They range from manual delineation to simple band ratios (e.g. Bayr et al., 1994; Jacobs et al., 1997; Paul 2002), to more complex band ratios such as the Normalized Difference Snow Index (NDSI) (e.g. Racoviteanu, 2008), and supervised classification techniques like spectral end members (Klein and Isacks, 1999), maximum likelihood classifiers (Aniya et al., 1996), principal component analysis (PCA) (Sidjak and Wheate, 1999) or fuzzy set theory (e.g. Binaghi et al., 1997). For (operational) glacier mapping on a global scale, the algorithm to be applied must be simple (in terms of the required pre-processing), accurate (compared to a reference data set and/or other algorithms), and robust (transferable to other regions without changing too many of the parameters). Hence, a high pre-processing workload is only justifiable when the results are much better than with less demanding algorithms. In this regard all supervised (e.g. selection of training areas or end members) or scene dependent methods (e.g. PCA) mentioned above are too demanding (see Albert (2002) for a detailed comparison) and are not considered further.

For the same reason, band ratios have become a quasi-standard for glacier mapping in the past decade (e.g. Racoviteanu et al. 2008), given that a SWIR band is available. When only panchromatic or false colour infrared images are available, only manual delineation of the glacier outlines can be applied. However, despite the often much higher resolution of the related panchromatic images (e.g. from aerial photography or high resolution satellite sensors), this could be much more error prone than glacier mapping with a lower resolution SWIR band. The example in Fig. 3.5 illustrates this problem for the Waxeggkees in the Zillertaler Alps (Austria), where the surrounding rock has the same spectral reflectance in the VIS as bare ice. As manual delineation needs to be applied in the post-processing stage in any case, we focus in the following on the description of the band ratios. The characteristics of the three most often applied band ratio classifiers is provided in Table 3.1.

The band ratio method is based on the division of the (high) DNs over ice and snow in the red band by the low DNs in the SWIR yielding high values over glaciers and low values elsewhere. Using a simple threshold the resulting ratio image can be segmented into glacier (black) and other terrain (white). This works for all ratios, either red/SWIR, NIR/SWIR or the NDSI: (green+SWIR)/(green-SWIR). As an example for the red/SWIR band ratio (e.g. TM3/TM5) the algorithm in pseudo code is:

```
IF (red/SWIR) > thr THEN glacier ELSE other
```

The threshold ‘thr’ is often close to 1.8 (+/-0.2) for this band combination. Depending on the software used, the implementation of the algorithm might look slightly different.

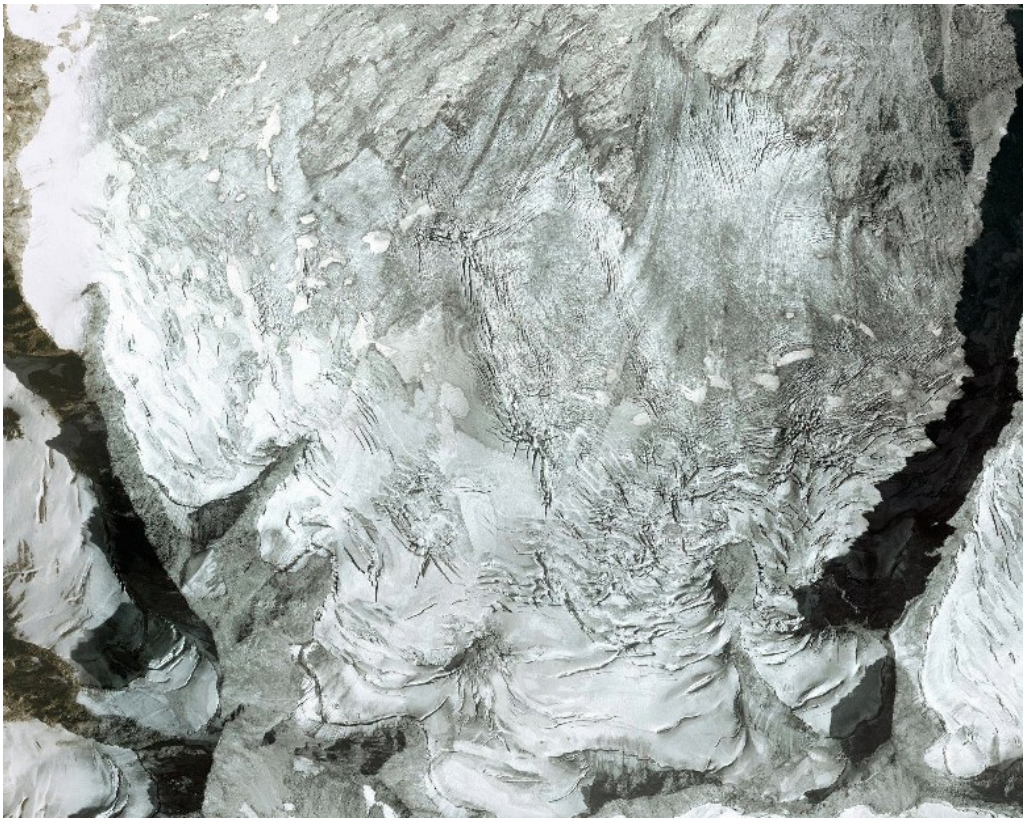

Fig. 3.5: Screenshot from GoogleMaps showing the Waxeggkees in the Zillertaler Alps (Austria). The glacier is nearly invisible in this natural colour image, indicating that a high spatial resolution alone is not always sufficient to accurately map glaciers.

Unfortunately, certain adjustments have to be made to all band ratios. An additional threshold in the blue (TM1) or green (AST1) band is required to improve the often occurring misclassification of rocks in shadow when using the red/SWIR ratio. The latter is due to the atmospheric scattering that is still present in the red band and brightens bare rock in shadow similar to ice in shadow. Band 1 is highly sensitive to atmospheric scattering and is strongly reflected from snow. Snow and ice in shadow is thus in general much brighter than rock in shadow and can be separated by a threshold (Paul and Kääb, 2005).

This correction is not required for the NIR/SWIR ratio as atmospheric scattering (or path radiance) is very low in the NIR. However, the high reflectivity of vegetation in the NIR often results in a misclassification of vegetation in shadow. This can be removed by additionally classifying vegetation, for example using the Normalized Difference Vegetation Index (NDVI). Of course, this step might not apply in regions without vegetation and it has to be considered on a case-by-case basis if red/SWIR or NIR/SWIR gives the better results (e.g. Andreassen et al., 2008; Paul and Kääb, 2005).

The NDSI has problems in regions with cast shadow as the high path radiance present in the green band needs to be subtracted before the NDSI is applied. The lowest DN in the respective scene can be found by histogram analysis and must then be subtracted from all DNs. This method is also named Dark Object Subtraction (DOS) in the literature (Chavez et al., 1988). The results are then very similar to the red/SWIR ratio (cf. Paul and Kääb, 2005).

Abbreviation	**BR RS**
Algorithm	Band Ratio with the red and SWIR bands (e.g. TM3/TM5)
Reference	Paul et al. (2003)
Applications	Paul and Kääb (2005), Andreassen et al. (2008), Paul et al. (2009)
Description	Strong differences in spectral reflectance of ice and snow in the SWIR compared to other terrain and the VNIR bands allows their automated classification (clean to slightly dirty glacier ice) from a simple band ratio.
Advantages	- The algorithm is very simple and the thresholds are robust, i.e. the result is not very sensitive on the exact value and a best value can easily be found.
Disadvantages	- Rock in shadow and turbid lakes are also mapped - An additional threshold in band TM1 is required to improve the shadow classification and wrong lakes need to be removed
Improvements	The thresholds have to be determined interactively, an automated determination of both thresholds should be developed

Abbreviation	**BR NS**
Algorithm	Band Ratio with the NIR and SWIR bands (e.g. TM4/TM5)
Reference	Paul et al. (2003), Paul and Kääb (2005)
Applications	Paul et al. (2002), Paul (2002), Jacobs et al. (1997), Bayr et al. (1994)
Description	Strong differences in spectral reflectance of ice and snow in the SWIR compared to other terrain and the VNIR bands allows their automated classification (clean to slightly dirty glacier ice) from a simple band ratio.
Advantages	- The algorithm is very simple and the thresholds are robust, i.e. the result is not very sensitive on the exact value and a best value can easily be found. - Is less sensitive to lakes
Disadvantages	- also maps vegetation (in shadow) that requires an additional threshold - sometimes misses ice in shadow
Improvements	The threshold has to be determined interactively, might be merged with BR RS

Abbreviation	**NDSI**
Algorithm	Ratio with the green and SWIR bands (e.g. (TM2+TM5)/(TM2-TM5))
Reference	Paul and Kääb (2005)
Applications	Racoviteanu et al. (2008)
Description	Strong differences in spectral reflectance of ice and snow in the SWIR compared to other terrain and the VNIR bands allows their automated classification (clean to slightly dirty glacier ice) from a simple band ratio.
Advantages	None compared to BR RS and BR NS (i.e. results are the same)
Disadvantages	- All rock in shadow and turbid lakes are also mapped when DOS is not applied to the green band before the ratio - Histogram analysis has to be performed manually
Improvements	All thresholds have to be determined interactively, an automated determination of both thresholds should be developed

Table 3.1: Details of the algorithms used for glacier mapping.

To an variable extent, all of the above methods misclassify turbid lakes as glaciers. While there is some potential to also classify lakes automatically from multispectral information alone (e.g. Huggel et al., 2002) and thus remove them from the glacier map, there is some overlap with glaciers that can remove correctly classified glacier pixels. In this regard the safest way is to manually select and delete the lake polygons in the post-processing stage (after vectorization of the outlines).

Finally, in some cases a correct spectral classification does not result in a correct classification of the object. For example, lakes on the surface of a glacier need to be included in the glacier area, whereas ice bergs or sea ice have to be excluded. This is currently most effectively performed in the vector domain of the post-classification stage.

From the comparison of the algorithms listed in Table 3.1 it becomes clear that the threshold selection is the most critical step for the classification. Currently, the advice is (e.g. Racoviteanu et al., 2009) to select this threshold in a most sensitive region (shadow) in a way that the workload for post-processing is minimized. In most cases this means that a rather low value for the TM1 threshold is used to get all ice and snow in shadow properly included. At the same time this increases noise or misclassification at other places. However, these additional (often isolated pixels) either do not matter (e.g. over water) or can be later removed by a noise filter. In some cases it is not possible to include the ice in shadow in one part of the image without including all bare rock in shadow in another part of the image. This can happen as a consequence of special atmospheric conditions (e.g. haze or fog), that locally increases path radiance. In such a case two glacier masks with two different thresholds can be created and digitally combined afterwards. In Fig. 3.6 an example of such a dual classification from the Canadian Rockies is shown.

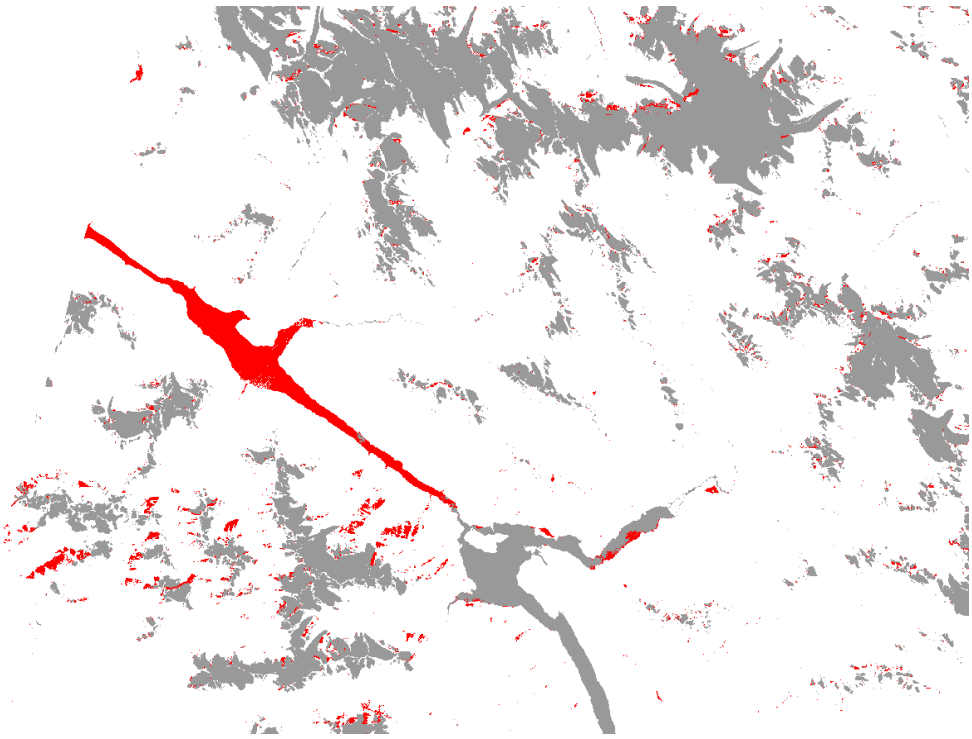

Fig. 3.6: Glaciers as mapped from two different thresholds. Whereas for the region in the lower left the mapped red regions were excluded, they were included for the other regions.

A final processing step is the application of a noise filter (e.g. 3 by 3 median) to eliminate isolated pixels (e.g. snow patches) and close small gaps on a glacier (e.g. in shadow). Whether the application of this filter is really a benefit for the mapping or not has to be decided on a case-by-case basis. In Fig. 3.7 we demonstrate the sensitivity of the algorithm on the threshold value applied and the changes of the glacier map due to the application of a median filter (3 by 3 kernel size). The number of pixels added by lowering the threshold in steps of 0.1 is very small. Moreover they appear in regions that have to be carefully checked and often corrected anyway (debris-cover and shadow). In this regard the threshold value can be considered as robust and good results were likely achieved even with a fixed threshold value (around 1.9 in this case). With a threshold of 1.8 (all colours) already some isolated noisy pixels (red) appear. This indicates that the threshold value should not be much lower than this. The median filter efficiently closes isolated gaps (blue pixels in the right image of Fig. 3.7) but at the same time also deletes isolated pixels or small pixel clusters (red). As the latter are often related to isolated (seasonal) snow patches, this consequence is rather beneficial. However, in regions with many very small glaciers and no seasonal snow, it might be better to proceed with the raw glacier map (e.g. Paul et al., in press).

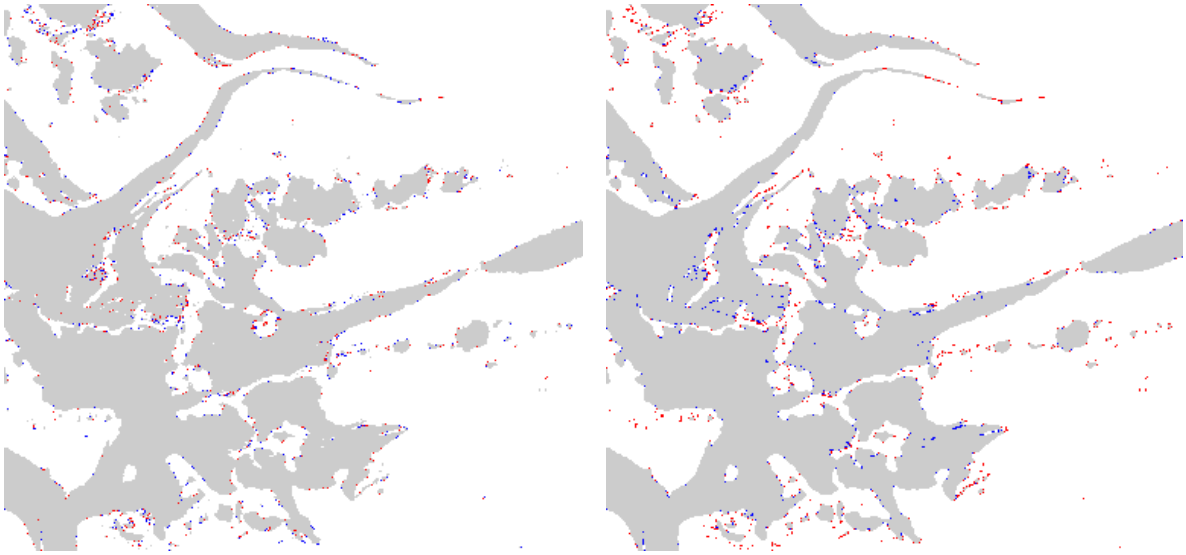

Fig. 3.7: Left: Three glacier maps combined resulting from three threshold values: 1.8 (all colours), 1.9: (grey and blue), 2.0 (grey). Right: Effect of a 3 × 3 median filter: red pixels are removed and blue pixels are added (shown here for the map with the threshold 1.9).

Applications in various regions of the world have shown that also glaciers under thin cirrus clouds (e.g. from aircraft contrails) or other optically thin clouds can be mapped with the TM3/TM5 band ratio (Paul and Andreassen, 2009). More difficult to map is bare ice in the shadow of convective clouds or zones with seracs. For all these regions careful visual inspection and maybe correction of the generated outlines is required, using one of the above mentioned RGB composites in the background. The quality of this step depends on the contrast of the image and the skills of the analyst to interpret subtle features. In any case, the application of one of the above automated methods to map clean glacier ice is strongly recommended compared to a full manual digitization. The latter should be restricted to applying edits to the initial mapping.

3.4 Expected performance gains by future developments

From the above description major shortcomings of the algorithms and the methodological issues to be considered become clear. In regard to the latter, the Glaciers_cci project is expected to make a substantial contribution to data consistency as a result of the round robin. This comparison of glacier delineation work should clearly reveal which issues need to be addressed in illustrated guidelines. In regard to expected algorithm improvements, further research would be helpful to reduce the workload in the post-processing stage. The problems to be addressed are compliant with the tasks listed in the Annex to the Statement of Work for the Glaciers_cci project: debris, water, shadow, clouds and snow fields. We expect further improvements for mapping debris-covered glaciers and those under frequent orographic clouds from microwave sensors (coherence image pairs taken in summer). Moreover, improved consideration of water bodies and shadow might result from incorporating precise topographic information from DEMs. For detection of seasonal and/or perennial snow fields the best idea remains to wait for a satellite scene with better snow conditions. All these issues will be investigated in more detail in the second year of the project.

Another important improvement we expect in the future is related to geolocation accuracy. For example, currently the void-filled SRTM DEM from CGIAR is used to orthorectify the Landsat scenes for the L1T product of USGS. It was found in a recent study by Frey et al. (subm.), that in the region of data voids the interpolated CGIAR DEM can have large errors, i.e. the elevations are systematically (caldera like) several hundred metres too low. This results in a 3-5 pixel shift in the respective region with related problems to match the outlines with other independent datasets (e.g. the drainage divides derived from a different DEM). With the DEM from the TanDEM-X/TerraSAR-X mission currently being produced, it might be possible that the orthorectified Landsat datasets offered by USGS will have an increased geometric accuracy in the future. Certainly, there will be further improvements that are yet difficult to foresee as science and the database to be used is evolving rapidly in this domain.

3.5 Required input data and generated output

The input data required to generate the output with the algorithms described above are an orthorectified satellite scene (with at least the geometric accuracy of the L1T product from USGS) and a DEM. Further details are described in the DARD (Glaciers_cci, 2011c). While the satellite data are normally provided in Geotiff format, the DEMs use a variety of formats (bil, geotif, ascii, grid, etc.). As a starting point, these formats have to be converted to the storage format of the digital image processing and GIS software used. The next step is related to pre-processing work (e.g. creation of true and false colour composites, deriving hillshades, contour lines and drainage divides from the DEM), before one of the algorithms described above is applied in the main processing stage. The output is a binary raster map that is converted to the vector format before the editing in the post-processing stage can start. For this purpose the entire dataset is still in the UTM projection of the satellite scene(s) used as an input. The further processing then follows the steps developed within the GlobGlacier project.

To facilitate internal communication, a tiered terminolgy was developed to discriminate different levels of processing. These levels are not related to the processing levels of satellite data in general (e.g. as used by ESA), but just to help to be precise and short. The raw glacier outlines have level 0 (L0), outlines corrected for gross errors (e.g. water, sea ice, clouds) have L0a, and fully corrected outlines (debris, shadow and all other issues) have L0b. Deriving individual glaciers (L1) from the L0b outlines requires to digitally intersect the L0b outlines

with drainage divides that need to be derived beforehand from the DEM. The digitization of drainage divides is time consuming as it requires manual work, at least it has to be done only once. For the glacier inventory, the L1 outlines are digitally combined with a DEM to have topographic parameters for each glacier (L2 product). Finally, the outlines are converted to the GLIMS format and submitted (L3).

So the main processing algorithm is located between the pre and the post-processing stage. In principle, only the algorithm itself works automatically whereas all other processing steps require manual intervention. However, some automated (script-based) processing is available for some of the steps as well (e.g. deriving L2 from L1 outlines). As the results of the various algorithms can only be distinguished at the pixel level (e.g. Paul and Kääb, 2005) and the uncertainties introduced in the post-processing stage are much larger, the focus of the round robin for glacier area is on the latter. A major issue after the round robin is thus to identify the most problematic regions in glacier mapping and give proper advice to the community (e.g. with illustrated guidelines) on how to solve them. In the end, the final product should meet the accuracy requirements as summarized in the URD (Glaciers_cci, 2011a) to be useful for further applications.

3.6 Error budget estimates

When considering the final glacier outline product, errors are introduced at the pre, main and post-processing stage. The quantification of the respective errors require different measures and are sometimes difficult to assess. As a first step, we provide an overview on the potential error sources in Table 3.2. From this table it become clear that the largest errors are introduced in the post-classification stage. They could be up to one order of magnitude larger than errors caused by the algorithm or the mosaicing of scenes in UTM projection (e.g. when debris-cover is not included). This is indeed not the error that occurs when the debris cover is manually corrected. However, in this case other errors occur (generalization, inconsistent interpretation of mixed pixels) that can be determined by multiple digitizations. The round robin should help to properly assess their magnitude. The geolocation error has no direct effect on glacier size, but needs to be considered when the outlines are combined with a different DEM (e.g. drainage divides).

Step	Error	Typical	Measure	Comment
Pre-processing	geolocation	+/- 1 pixel	GCPs (provided with the Metadata information)	only relevant for L1/L2 outlines (DEM fusion)
Main-processing	algorithm	< 3%	validation data	accuracy is for debris-free ice
	threshold	< 5%	overlay of binary maps	see Gjermundsen et al. (2011)
	median filter	<2%	RGB composites filtered vs. unfiltered	could be larger for very small glaciers
Post-processing	water	> 100%	visual inspection (432)	should be removed
	other ice	> 100%	visual inspection (432)	should be removed
	debris	> 50%	comp. with ground truth	requires manual digitization
	shadow	< 50%	visual inspection (321)	can be locally difficult to identify
	projection	<2%	comparison with equal area projection	error <2% for +/-2 scenes combined in UTM projection

Table 3.2: Errors contributing to the overall error budget.

When assessing an error against a reference data set, several issues have to be considered to derive the correct conclusions: The area of the glacier (polygon) changes with pixel size (e.g. Paul et al., 2003), at a much higher spatial resolution different features become visible, and without a band in the shortwave infrared (e.g. panchromatic imagery) the determination of the outline could be much more complicated (see Fig. 3.5). Moreover, some care has to be taken that the projection of the data used for comparison is the same. The reference data set that is used for comparison (or validation) must be acquired at the same point in time (week is sufficient in most cases) or at least snow conditions must be the same.

3.7 Practical considerations and implementation

To summarize, the algorithm development for the glacier area product has the following main goals:
- periodically check the geolocation accuracy of the USGS L1T data (DEM improvements?)
- further test and develop algorithms for critical regions (debris, water, shadow, clouds, sea ice, frozen lakes) to reduce the post-processing workload
- perform multiple digitization tests during the round robin to identify the most problematic issues in image interpretation and to assess the analysts internal accuracy.
- determine an absolute accuracy by comparison with higher resolution data sets
- increase the degree of automation and evaluate the potential of free software for image processing and later editing (ImageMagick, GRASS, QGIS, GLIMSView, etc.)
- have more consistent datasets in the GLIMS database

Whereas the specific data processing work-flow depends on the software used to process the data, the major steps are common to all software. While the core algorithm that is used by the analyst to map the glaciers in a specific region can be freely chosen, the post-processing issues have still to be better illustrated. Specific guidelines for the analysts are already available from the GLIMS website, but these products could certainly be updated/further improved. Once glacier outlines and drainage divides are available, the automation of data processing might be further increased. However, it has to be noted that different user communities (e.g. regional hydrologists vs. sea-level-rise modellers) require different products (e.g. only L0b instead of L2). So not in all cases the final product (glacier covered area) has to be provided as L2. As data availability and technical development is a continuous process, new algorithms and further improved products are expected in the future. Glaciers_cci will continously monitor the ongoing efforts and actively participate in related activities. This includes the compilation of a global product (a map of glacier covered areas) for the climate modelling community in netCDF format.

4. Elevation changes from repeat altimetry

4.1 Introduction

The specific objectives of this chapter are:
(a) to provide the theoretical basis of the algorithms that will be used to generate elevation changes maps from laser and radar altimeter data;
(b) to assess the accuracy of these products; and
(c) to evaluate the range of applicability and the limitations of the derived data.

Satellite altimetry is a powerful tool for mapping the surface elevation of glaciers and ice caps and the instruments used to reach this purpose can be divided in two groups based on the part of the electromagnetic spectrum they utilise.

Altimeters using microwave frequencies are commonly referred to as radar altimetry. At these wavelengths the signal can penetrate cloud cover, making the measurements possible in all weather conditions. In addition, the use of microwaves enables measurements to be made independently from sunlight conditions. The repeat orbits of the satellites with altimeters on board cover a region of up to 1 km on either side of a nominal ground track. Furthermore, satellite altimetry radars have been in continuous operation since 1991 and new missions are scheduled for the next decade. There is therefore the availability of long time series and as a consequence the possibility to monitor seasonal to interannual variations during the lifetime of these satellites. However, these instruments are primarily designed to operate over uniform surfaces such as oceans rather than complex topography that may cause data loss. Other disadvantages are related to the footprint size (c. 10 km), the ionospheric delay and the variable penetration of the signal in the snowpack.

Laser altimeters are altimeters that operate at optical wavelengths. The main advantages of these instruments are related to the high range accuracy (accuracies better than 0.05 m have been demonstrated under optimal slope conditions by Fricker *et al*., 2005) and to the footprint size, which leads to less data loss. In fact, the most significant difference of laser over radar altimeters is the much smaller ground footprint of less than a hundred metres in diameter (Zwally *et al.*, 2002), in contrast to that of several kilometres of radar altimeters. The main drawbacks are the short time series, the infrequent repeat passes, the detector saturation (Fricker *et al.*, 2005) and cloud interference with the light beam.

Although airborne laser altimeters are widely used remote sensing instruments, there have been only few of them orbiting in space. This is due to laser altimeters being electrically and mechanically more complicated than radar altimeters, making the space environment particularly harsh for them.

In the next section the electromagnetic properties of ice and snow will be reported and the main concepts of the interaction of an electromagnetic wave with ice will be explained to make clear the physics behind the penetration of an electromagnetic wave. This can be quite significant over ice surfaces at the frequencies commonly used for space radar altimetry (Ridley and Partington, 1988). In fact, in the case of dry snow a radar altimeter will measure an elevation below the snow-air interface, whereas in the case of wet snow, the instrument

will measure an elevation of the snow-air interface. The phenomenon that causes this uncertainty in the measurement, known as volume scattering, implies the need for a correction to the height measurements and the use of appropriate retracking algorithms, which will be described in section 4.2. In section 4.3, the concepts of a radar and a laser altimeter will be explained in more in detail, followed by the algorithms used to retrieve elevation changes in section 4.4. Section 4.5 describes the pre-processing procedure to apply to radar altimeter data, in particular the retracking techniques used. It is worth underlining that such algorithms will not be validated in the framework of Glaciers_cci, because they are already well established. In section 4.6 potential future developments are presented and the last section discusses the errors that affect the altimeter data and the major corrections necessary to apply when the altimeter operates over ice surfaces.

4.2 Scientific background on altimetry

This section presents basic concepts governing electromagnetic wave propagation relevant to active remote sensing of ice and snow and especially useful to understand the penetration of the electromagnetic wave in ice masses (particularly for longer wavelength radar altimetric measurements), which effects the estimation of elevation changes (Ridley and Partington, 1988). The main phenomena influencing the propagation of microwaves are absorption, reflection, refraction, and scattering. A summary of the dielectric properties of ice and snow is given whose characteristics are primarily influenced by frequency, temperature, and density. A description of extinction and its absorption and scattering components is also presented.

4.2.1 Dielectric properties of snow and ice

The basic laws of electromagnetism are given by the Maxwell's equations and the interaction of the electromagnetic wave with any material is controlled by the constitutive parameters: the permeability μ, the permittivity ε, and the conductivity σ (lossy medium). Under the assumption that the medium is linear, homogeneous, isotropic, stationary and non dispersive these parameters can be considered as scalars. A linear medium is a medium in which the permeability μ, the permittivity ε, and the conductivity σ are not functions of the applied field strength. It is homogeneous when all properties are the same at all points in the medium, namely the constitutive parameters are not a function of the position. An isotropic medium has μ, ε, and σ independent of the field directions. Materials whose characteristics are invariant in respect to the time are referred to as stationary. When the constitutive parameters are not a function of the frequency, the medium is referred to as non-dispersive. The parameter ε_c is the complex permittivity or dielectric constant and defined in Eq. 4.1. Conventionally the real and imaginary parts of ε_c are denoted ε' and ε'' (Ulaby et al, 1982):

$$\varepsilon_c = \varepsilon - j\frac{\sigma}{\omega} = \varepsilon' - j\varepsilon'' \tag{4.1}$$

It is common practice to express the permittivity and permeability relative to their values in a vacuum by defining dimensionless quantities (Ulaby et al, 1982):

$$\varepsilon_r = \frac{\varepsilon_c}{\varepsilon_0} \tag{4.2}$$

$$\mu_r = \frac{\mu}{\mu_0} \tag{4.3}$$

where $\varepsilon_0 = 8.854 \times 10^{-12}$ Farad/m and $\mu_0 = 4\pi \times 10^{-7}$ Henry/m represent the permittivity and permeability values in free space, and ε_r and μ_r are referred to as the relative dielectric constant and relative permeability, respectively. In the microwave region $\mu_r \simeq 1$ for most natural materials (Ulaby et al, 1982), although the relative dielectric constant ε_r is in general a complex function composed of a real part ε_r' and an imaginary part ε_r'' :

$$\varepsilon_r = \varepsilon_r' - j\varepsilon_r'' \tag{4.4}$$

The electromagnetic properties of ice and snow are described by these parameters, which are of fundamental importance for the interpretation of the radar altimeter measurements over glacier ice (due to the penetration of the wave in the medium). Snow and firn (material in the intermediate stage between snow and ice) are regarded as homogeneous media and can be described by an effective complex dielectric constant, which is a weighted average of the dielectric constants of their air and ice constituents (Maetzler, 1987). Liquid water content has a profound impact on the dielectric properties. Ionic impurities (due to e.g. salts and volcanic acids) may also strongly impact the dielectric constant. Ice is a low-loss, non-magnetic medium such that $\mu_r = 1$ is assumed. For such a medium the real part of the dielectric constant determines the velocity of propagation and the imaginary part the wave attenuation. The real permittivity of ice is relatively well-determined and is nearly constant over microwave frequencies (Maetzler and Wegmueller, 1987), whereas the imaginary part is difficult to quantify mainly because it is so small and because of its sensitivity to temperature, impurities, and scattering from air bubbles. Hence, variations of several orders of magnitude in its value have been reported in the literature. However, description of the electromagnetic properties of ice has significantly improved in recent years with the availability of new and more accurate measurement techniques. A recent review of the complex dielectric constant of pure ice incorporating updated measurements across the optical and microwave electromagnetic spectrum is available in Warren and Brandt (2008) with temperature dependencies treated by Maetzler (2006). The dielectric properties of snow and firn were investigated both experimentally and theoretically in Maetzler (1987).

The real part of the relative dielectric constant or relative real permittivity ε_r' is independent of the frequency in the microwave region and has a slight temperature dependence (Maetzler and Wegmueller, 1987; Fujita et al., 1992). Numerous investigations have been carried out to determine ε_r' for pure ice, with typical values ranging from 3.14 to 3.18 (Evans, 1965; Ulaby, 1982, Warren and Brandt, 2008). For the microwave frequencies of interest, the relative real permittivity of pure ice at -20 °C is represented well by a value of 3.15 (Kovacs et al., 1995). For dry snow and firn ε_r' is primarily a function of the density ρ_{firn}. Assuming cold conditions, Kovacs' empirical mixing-formula can be used to relate firn density and relative real permittivity (Kovacs et al., 1995).

Although many mixing formulae are available including the Maxwell-Garnett (Sihvola and Kong, 1988) and Polder-van Santen models (Maetzler, 1996), differences between the models at the firn densities of interest are very slight and Kovacs' empirical mixing-formula is largely used because of its close match to data collected at microwave frequencies and its ease of implementation. The sensitivity of ε_r' to snow and ice grain shape was found to be small at microwave frequencies (Maetzler, 1996) and is not addressed further.

As opposed to ε_r' and mentioned above, the imaginary part of the dielectric constant ε_r'' varies significantly in the microwave region. As ε_r'' strongly influences the wave attenuation, it is also referred to as the dielectric loss. Ice is one of the most transparent media at microwave frequencies (Maetzler, 2006) leading to very low dielectric loss. This loss arises from two principal causes:

1. The high-frequency tail of the Debye relaxation spectrum, with a relaxation frequency in the KHz region, due to the re-orientation of frozen water molecules in the presence of an alternating electric field (Dowdeswell and Evans, 2004; Maetzler, 1987).
2. The low-frequency tail of infrared absorption bands in the THz region (Maetzler, 1987).

Therefore, a simple model suitable to describe the frequency dependence of ε_r'' for pure ice can be expressed by the sum of two components: one inversely proportional to frequency for the high-frequency tail of the Debye relaxation spectrum, and the other proportional to the frequency for the low-frequency tail of the infrared absorption bands (Maetzler, 1987). Uncertainty in the precise behaviour of ε_r'' as a function of frequency and temperature is a serious limitation in the modelling of the microwave signatures of ice and snow (Maetzler, 1987). This lack of knowledge translates directly to uncertainties in quantities relevant for remote sensing including the extinction (Maetzler and Wegmueller, 1987).

4.2.2 Scattering

When an electromagnetic wave impinges the surface boundary between two semi-infinitive media, scattering takes place only at the surface boundary if the two media can be assumed homogeneous. Under such a supposition, the problem is named a *surface scattering* problem. On the other hand, if the lower medium is inhomogeneous or is a mixture of materials of different dielectric properties, then a portion of the transmitted wave scattered backward by the inhomogeneities may cross the boundary surface into the upper medium. In this case scattering takes place within the volume of the lower medium and it is referred to as *volume scattering*. In the case of ice surfaces both scattering processes are involved. Surface scattering is primarily dependent on surface roughness, permittivity (i.e. dielectric constant), and imaging geometry. Volume scattering is principally a function of the size, shape, density, dielectric constant, and orientation of the discontinuities.

When the surface boundary separating the two semi-infinitive media is perfectly smooth, the reflection is in the specular direction and is described by the Fresnel reflection laws. On the other hand, when the surface boundary becomes rough, the incident wave is partly reflected in the specular direction and partly scattered in all directions. Qualitatively, the relationship between surface roughness and surface scattering can be illustrated through the example shown in Fig. 4.1. For the specular surface, the angular radiation pattern of the reflected wave is a delta function centred about the specular direction as shown in Fig. 4.1a. For the slightly rough surface (Fig. 4.1b), the angular radiation pattern consists of two components: a reflected component and a scattered component. The reflected component is again in the specular direction, but the magnitude of its power is smaller than that for smooth surface. This specular component is often referred to as the *coherent* scattering component. The scattered component, also known as the *diffuse* or *incoherent* component, consists of power scattered in all directions, but its magnitude is smaller than that of the coherent component. As the surface becomes rougher, the coherent component becomes negligible.

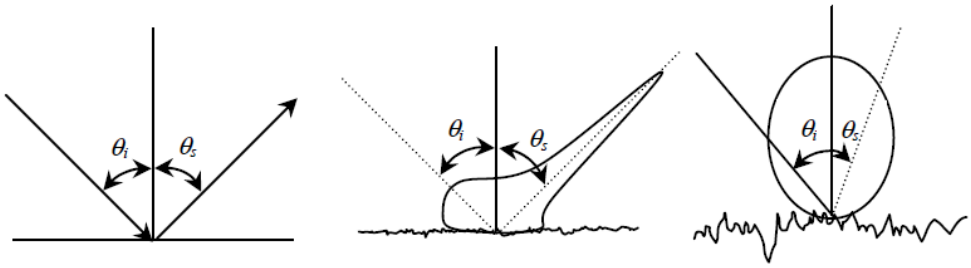

(a) **(b)** **(c)**

Fig. 4.1: Relative contributions of coherent and diffuse scattering components for different surface-roughness conditions: (a) specular, (b) slightly rough, (c) very rough.

A precise description of scattering from randomly rough surfaces is difficult; while the problem of reflection and transmission of a plane wave at a plane interface between two homogeneous media can be solved exactly, no closed-form solution exists when the interface is irregular (Ulaby et al., 1982). However, for many practical applications approximate solutions are sufficient for a description of the electromagnetic behaviour (Ulaby et al., 1982). Ridley and Partington (1988) have demonstrated that the altimeter return over ice sheets is strongly influenced by volume scattering as well as surface scattering. Volume scattering results from dielectric discontinuities within inhomogeneous media and from the presence of inhomogeneities in a host medium, whose size, shape, density, dielectric constant, and orientation affect the scattering. They cause a redistribution of the energy of the transmitted wave into other directions and results in a loss in the transmitted wave (Ulaby et el., 1982). An important descriptor of volume scattering is the extinction coefficient, which is the reduction in signal power due to absorptive and scattering losses per unit length as an electromagnetic field propagates through a volume.

The most significant simplifying assumption in the derivation of the volume scattering for a radar altimeter wave-form model is that the snowpack is considered homogeneous within the volume sampled by the altimeter. This allows the attenuation of the signal through the snow to be described by a constant extinction coefficient, and it permits the contribution of the differential shell volumes to the received power to be described by a constant back-scattering cross-section per unit volume. With this assumption, the volume scattering model is a first-order approximation to the physical situation where the snow density and grain-size are known to increase with depth under typical ice-sheet conditions (Davis and Moore, 1993).

4.2.3 Extinction coefficient

One of the major tasks that needs to be addressed for radar altimeter interpretation over glaciers and ice caps is understanding to what degree the electromagnetic wave penetrates into the medium. To describe the radar return and develop correct retracking algorithms (refer to section 4.5), the parameter of extinction is a useful quantity. It is a measure of the total power loss of a propagating wave within a medium and is usually expressed per unit length as an extinction coefficient (Ulaby et al., 1982). Extinction is the combined effect of scattering and absorptive losses, where the absorption component is a strong function of frequency, temperature, density, water content, and ice impurities. The scattering component is influenced by near-surface melt features including the presence of ice layers as well as the size and shapes of ice crystals and trapped air bubbles. The concept of extinction is closely related to penetration depth.

Extinction also has implications on the accuracy of existing radar products, as knowledge of its temporal and spatial variability could help correct radar altimeter derived elevation maps which suffer from an extinction-dependent penetration bias (Scott et al., 2006).

However, there are still fundamental gaps in our understanding of the electromagnetic properties of ice originating from compressed snow, particularly at microwave frequencies. There are large variations in published extinction results for pure ice in the literature dependent upon the method used, instrument accuracy, and purity of the samples, and there are few established methods of determining extinction outside of the laboratory. Most investigations of glacier ice extinction have been carried out during ground-based experiments where generally either high-frequencies (Davis and Poznyak, 1993; Maetzler, 1987; Rott et al., 1993) are used to reduce antennae and sample sizes, or very low-frequencies are used (Bamber, 1987; Moore et al., 1999) to image the glacier bedrock.

For its description we refer to the situation represented in Fig. 4.2, where for simplicity the surface material has been referred to as "snow", recognising that in the first layer the material is normally a mixture of snow and firn. As the wave penetrates the ice surface, it is attenuated by the ice volume. The reduction in power density at depth l is defined by the equation (Davis and Moore, 1993; Ulaby et al., 1982):

$$P_t(l) = P_i e^{-k_e l} \tag{4.5}$$

where P_i is the incident power density and k_e is the power extinction coefficient. Penetration depth δ_p is defined as the depth l where the incident power density is reduced in magnitude to $1/e$ or ~ 37% (Davis and Moore, 1993; Ulaby et al., 1982). For an extinction coefficient that varies with depth l, δ_p is defined by:

$$\int_0^{\delta_p} k_e(l')dl' = 1 \tag{4.6}$$

while for a constant extinction coefficient this reduces to:

$$\delta_p = \frac{1}{k_e} \tag{4.7}$$

In the limit, as the extinction coefficient approaches infinity, the depth of penetration approaches zero and only surface-scattering contributes to the back-scattered power.

From scattering theory the extinction coefficient k_e consists of two parts (Maetzler, 1987; Ulaby et al., 1982):

$$k_e = k_a + k_s \tag{4.8}$$

where k_a is the absorption coefficient and k_s the scattering coefficient.

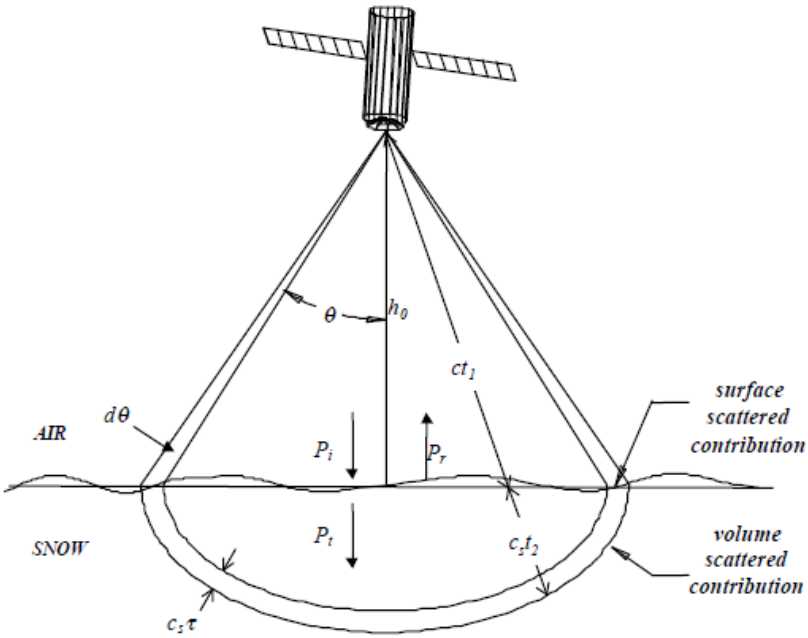

Fig. 4.2: Geometry for satellite-altimeter pulse that propagates along the ice surface producing volume scatter (Davis and Moore, 1993).

By absorption losses, it is meant that the transmitted energy is transformed into other forms of energy (such as heat), and by scattering losses, it is meant that the energy is caused to travel in directions other than the direction of the incident radiation (Ulaby et al., 1982). Extinction within ice is influenced by frequency, temperature, and density, as well as by surface scattering from englacial layers and volume scattering from snow and ice grains, air bubbles, and ice inclusions. Birefringence may create a situation of slight differential extinction, i.e. a polarisation-dependent extinction coefficient, although the anisotropic effects are generally within measurement accuracies and thus small enough to be neglected.

An important distinction must be made between attenuation and extinction coefficients which are sometimes used interchangeably in the literature. Conventionally the attenuation coefficient is defined as the rate the 'field strength of an electromagnetic wave decreases with distance' (Evans, 1965) and generally accounts for only absorption effects. Extinction accounts for both absorption and scattering components and describes the rate of decrease of the power of the wave.

For ice a simplified form for k_a is given by (Maetzler, 1987):

$$k_a = \frac{2\pi\varepsilon_r''}{\lambda_0\sqrt{\varepsilon_r'}} \tag{4.9}$$

where λ_0 is the wavelength in a vacuum. As the real part of the relative permittivity ε_r' of ice is virtually independent of frequency and temperature in the microwave region, it is the imaginary part of the dielectric constant, which is responsible for variations in absorption (Maetzler, 1987).

Recent measurements of the absorption coefficient of pure ice at microwave frequencies have been weaker by factors of 2-5 than previously reported (Warren and Brandt, 2008), where it is likely that extinction measured in the laboratory that had been attributed to absorption was partly caused by scattering from small air bubbles.

Scattering within firn volumes is mainly attributed to variations in the real part of the dielectric constant and is strongly related to changes in density. The scattering component of glacier ice extinction k_s is influenced by near-surface features including the presence of ice layers, lenses and pipes, as well as by the size, density, and distribution of ice crystals and trapped air bubbles. Because inhomogeneities in the firn can be as small as individual grains or as large as decimetre to metre-sized icepipes, a precise model of the interactions between the incident wave and ice inclusions for the determination of the scattering coefficient is a difficult task. Various models have been proposed to compute k_s when scattering from ice crystals much smaller than the wavelength is the dominant scattering mechanism. These models include:

- Rayleigh scattering (Maetzler, 1998; Sneep and Ubach, 2005)
- Dense Medium Radiative Transfer (DMRT) theory, a modified Rayleigh model to account for multiple scattering due to the close spacing of volume scatterers (Tsang et al., 1985; Wen et al., 1990).
- Improved Born Approximation model (Maetzler, 1998), representing a modification to the Rayleigh model for quasi-dense media to account for wave propagation in an effective medium.

The most well-known and widely applied model is Rayleigh scattering due to its simplicity. For a volume of uniformly-distributed spheres with real relative permittivity ε'_r ice and radius r_g embedded in a background of air, Rayleigh scattering gives extinction scattering coefficient (Maetzler, 1998):

$$k_s = 2v_{firn} k_0^4 r_g^3 \left(\frac{\varepsilon'_{r\,ice} - 1}{\varepsilon'_{r\,ice} + 2} \right)^2 \tag{4.10}$$

where $k_0 = 2\pi/\lambda_0$ is the free-space wavenumber. Firn fraction $v_{firn} = \rho_{firn}/\rho_{ice}$ is the fractional volume of the firn occupied by the particles, and ρ_{firn} and ρ_{ice} = 0.917 g/cm^3 (Kovacs et al., 1995) are the firn and pure ice densities, respectively. Due to the r_g^3 and λ^{-4} dependencies in (4.10) the scattering coefficient is very sensitive to changes in grain size and to the wavelength of the incident wave.

Additional corrections can be implemented to account for non-sphericity of molecules and for a distribution of grain sizes rather than a single grain radius. More sophisticated models incorporating multiple scattering have also been developed for dense media scattering problems (Tsang et al., 1985; Wen et al., 1990). The introduction of near-field effects between adjacent particles results in a scattering coefficient less than that under the assumption of independent Rayleigh scattering. However, these models have had a lack of success in matching theoretical results with observed backscatter data from snow and ice with an underestimation of the scattering coefficient (Wen et al., 1990; West et al., 1993), such that the added value of the extra modelling complexity is not clear.

4.3 Review of radar and laser principles

4.3.1 Radar altimetry

Radar altimeters provide a measure of the time t_d of a radio signal to travel from the emitting instrument, reach a target surface, and return/scatter back. The round trip distance from the reflecting target to the radar is given by (Elachi, 1988):

$$r = \frac{ct_d}{2} \tag{4.11}$$

where c is the speed of light and t_d is the round-trip delay. The accuracy with which the distance is measured is given by:

$$\Delta r = \frac{c}{2B} \tag{4.12}$$

where B is the signal bandwidth.

The operating principle of an altimeter is shown in Fig. 4.3. Surface elevation h is calculated as the difference of the satellite altitude a and the measured range r:

$$h = a - r \tag{4.13}$$

Surface elevation h is in relation to the reference ellipsoid used for determining satellite altitude a (see Fig. 4.3). In addition to measuring range, the altimeter records a sample of the pulse echo (return) and estimates other parameters, including the magnitude of the return.

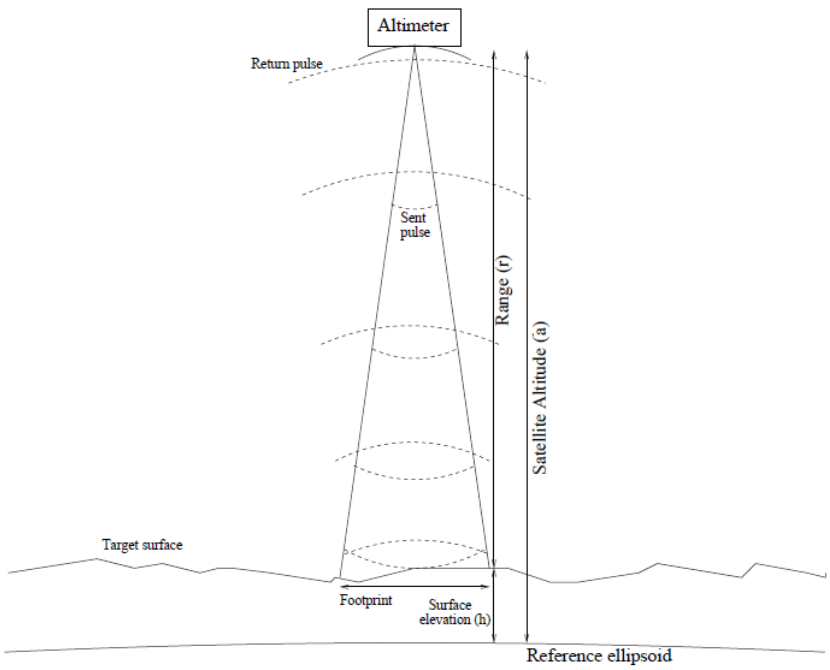

Fig. 4.3: Altimeter measurement principle

The side view representation in Fig. 4.4 shows the propagation of a single pulse along the beam of the antenna towards a horizontal and planar surface. The curved lines represent the pulse propagating and the temporal width between the curves is constant and equal to τ, the duration of the pulse length. A different visualization of the propagation (looking down on the scattering surface from the instrument position) is also provided in Fig. 4.4 (plane view). When the spherical wavefront first hits the surface at the instant time t_0, the footprint is a point. The area illuminated by the pulse rises to a circular area until the descending edge of the wavefront reaches the surface, at the instant time t_1. The pulse-limited footprint is the maximum circular area defined as the radius of the leading edge of the pulse when the trailing edge of the pulse first hits the surface. As the pulse propagates, the circle transforms into rings of equal area (Fu and Cazenave, 2001). The figure shows also, in black color, thereturn waveform from the surface assumed horizontal and planar. Thus, it represents the typical return from an ideal surface. However, in the case of a generic rough surface, the average return shows a similar trend. The power received begins to increase from the time when the wavefront hits the surface, t_0, and continues to increase for the duration of the pulse. The waveform presents a linear leading edge corresponding to this initial interaction. At the times greater than the pulse duration, the area intercepted by the pulse remains constant with time. But instead of remaining constant, the power of the reflected pulse actually decreases gradually with time according to the illumination pattern of the antenna.

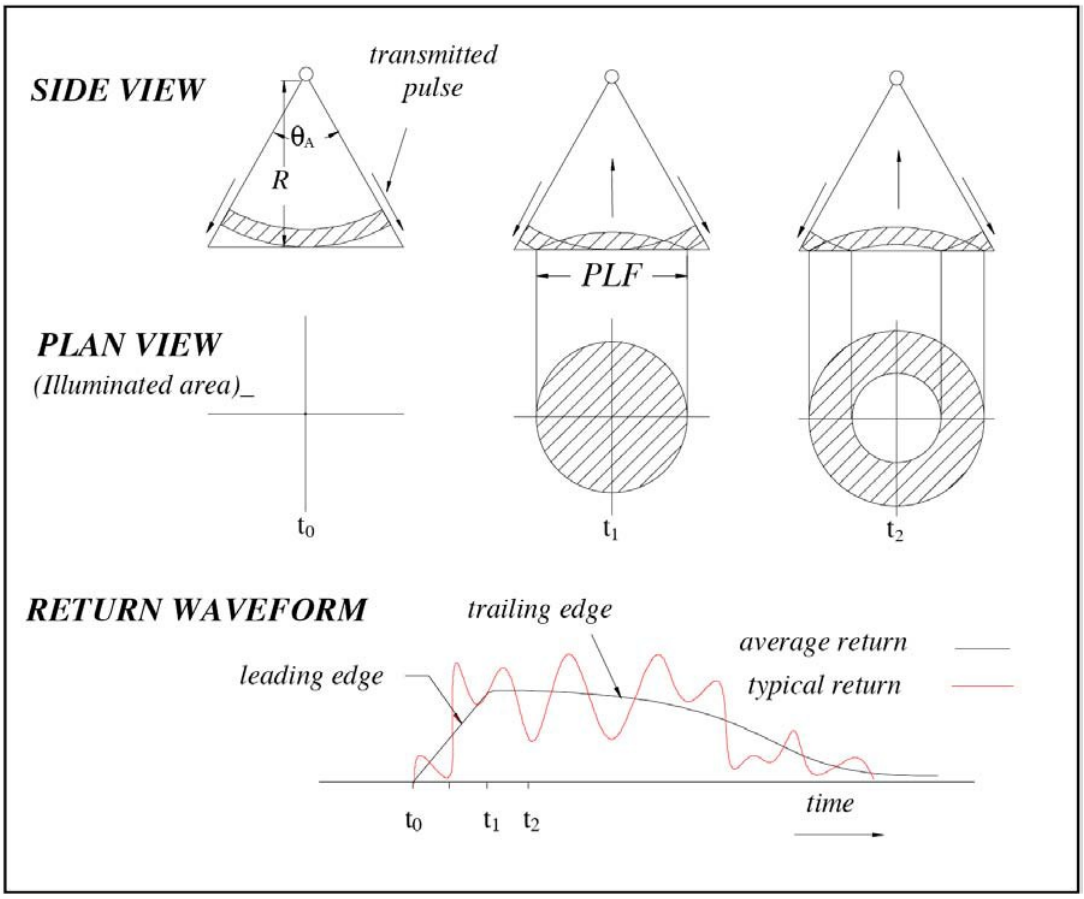

Fig. 4.4: The interaction of a radar altimeter pulse with a horizontal and planar surface, from its initial intersection (t_0), through the intersection of the descending edge of the wavefront with the surface (t_1), to the stage where the pulse begins to be attenuated by the antenna beam (t_2). The return is from surface only (Ridley and Partington, 1988).

Figure 4.4 shows in red the individual return from each single facet representing the elementary target of the surface. The return is similar to the noise that results from the interference between reflections from multiple facets and its shape reflects the statistical properties of the surface. The presence of evident peaks and troughs, especially over ice, is often the result of surface irregularities due to a large variability in the elevation. Another effect of such irregularities, when they are larger than the pulse width, is to impose an additional slope on the leading edge of the returned signal strength curve. Indeed, for a perfectly smooth surface, the echo is a mirror image of the incident pulse, whereas if the surface has some roughness, some return occurs in the backscatter direction at slight off-vertical angles as the pulse footprint spreads on the surface. This results in a slight spread in time of the echo. If the surface is very rough, some of the energy is scattered when the radio pulse intercepts the peaks of the surface and more energy is scattered as the pulse intercepts areas at various heights of the surface. This leads to a larger multi-path spread of energy which results in noticeable rise in the echo leading edge. The rise time can be used to measure the surface roughness.

4.3.2 Laser altimetry

Many of the characteristics of satellite laser altimetry over ice surfaces carry over from radar altimetry, which has a 20-year history. The basic measurement is the same principle – the determination of the travel time of an electromagnetic pulse from the satellite to the surface and back. For both types of altimeter the shape of the return pulse is modified by irregularities in the ice surfaces. However, there are important differences that arise from the different wavelengths and beam widths and that affect the height calculation. Before discussing these issues, we present in Fig. 4.5 sketches of the returned laser pulse, which is broadened by the distribution of surface heights within the footprint. The surface height distribution is characterised by a mean surface slope and a surface roughness within the footprint.

As already mentioned in the introduction, there are two crucial ways in which the laser altimeter differs from the radar altimeter: it has a much smaller footprint and it operates at a much higher electromagnetic frequency. The small footprint means that returns will come from only one spot on the surface at a time and that the position of that spot will be known. The high frequency means that the signal will not penetrate deeply below the surface. These characteristics simplify greatly the determination of the surface geometry. On the other hand, clouds and aerosol in the atmosphere affect the laser beam. Heavy clouds (optical depth > 2 or so) will completely block ground returns, whereas thinner clouds and aerosols cause forward scattering, which is indeed a specific problem for laser altimeters. In the presence of clouds or aerosols in the atmosphere, a part of the signal can be scattered. These scattered photons travel a longer path than photons that pass directly to and from the target. Therefore the mean travel time of the return pulse is lengthened, and the centroid of the pulse is shifted toward a later time (Duda *et al.*, 2001). A method to avoid errors due to forward scattering is to identify the presence of forward scattering from the waveform. Forward scattering causes a long tail in the waveform (Fricker *et al.*, 2005), and measurements with such a tail can later be discarded.

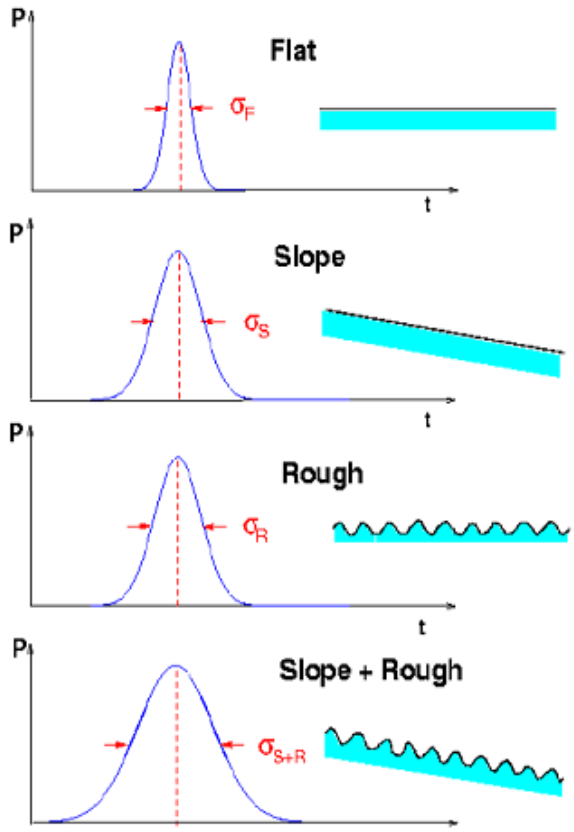

Fig. 4.5: Characteristics of returned laser pulse as function of surface type. Presence of surface slope and roughness both broaden the pulse.

Gaussian waveform fitting

The GLAS instrument onboard ICESat is designed to measure the precise time it takes the laser pulse to travel from the satellite to the Earth's surface and back again. The transmitted laser pulse is reflected from an elliptical footprint of the Earth's surface that varied from 52x95 m (lasers L1-L2c) to 47x61 m (lasers L3a and L3b), an average of 64 m (Abshire et al., 2005). For each transmitted laser pulse, the altimeter collects 4.5 million 1 nanosecond samples that are pre-processed onboard into 544 samples for transmission back to Earth. To determine in which 544 sample time range the reflection from the Earth's surface is contained, a generalized DEM is used to predict the time return (Brenner et al., 2003).

Two 2nd level products are available, GLA06 (Zwally et al., 2010a) and GLA14 (Zwally et al., 2010b). The products differ by the number of potential Gaussian fits used to determine the mean elevation within the footprint. The GLA06 products are meant for glaciers and ice sheets, because their relatively flat surfaces typically return waveforms that approximate a single Gaussian and thus the average centroid of maximum two Gaussian fits are used to determine the mean elevation within the footprint. The GLA14 products are designed for land terrain surfaces as the steeper slopes, greater roughnesses and possible vegetation produce wider and multi-model echo waveforms (Fig 4.5). Therefore, GLA14 uses an average of maximum six Gaussian fits to determine the mean elevation within the reflected footprint (Zwally et al., 2002). The difference between the two products is small, with average differences less than about 20 cm, standard deviations of ±60 cm though maximum differences up to ±3 m can occur in alpine terrain (e.g. New Zealand and Svalbard (Fig. 4.6)).

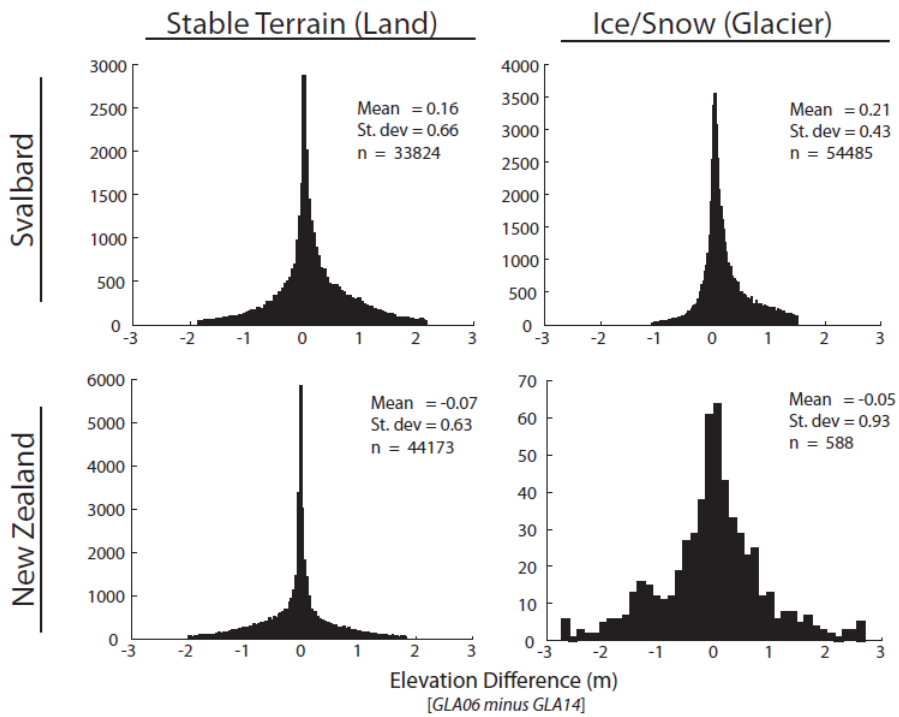

Fig. 4.6: Histograms of the elevation differences between GLA06 and GLA14 ICESat products on stable terrain and over ice. The two datasets, Svalbard and New Zealand, are those used in Nuth and Kääb (2011) and are from release 31. The two distributions on Svalbard also seem slightly skewed towards more positive GLA06 elevations than GLA14 elevations. This is most likely the lack of saturation corrections in the GLA14 products since super-saturated signals generally result in a longer range, thus lower elevation of the GLA14 products (Fricker et al., 2005).

4.4 Algorithms for altimeter data

Elevation change rate is determined from altimeter measurements using crossover or repeat track analysis. A crossover is the elevation difference at the intersection of two ground-tracks. The elevation difference is assumed to be an actual surface elevation change at the crossover location, since it occurs at the same location but different times, which means that some of the spatial errors can be eliminated. In repeat track analysis, elevation measurements from an altimetry satellite with near-repeat ground-tracks are used to estimate surface characteristics, such as elevation change rate. As the ground-tracks will not repeat exactly, the cross-track offsets should be accounted for in repeat track analysis so that the ground-tracks are more directly comparable.

Crossover and repeat track analyses are primarily used for the retrieval of elevation change or elevation change rates. However, in addition to information on elevation change, an elevation derived from a laser or radar altimeter contains effects from physical processes and measurement errors. Both methods use different techniques to remove error terms present within the derived elevations.

4.4.1 The crossover method

Crossovers are used to determine elevation change at the intersection of two altimeter passes. In this section, a detailed description of crossover theory will be given.

Description

Surface elevation differences (*dH*) are computed from surface heights (*H*) at the intersection or "crossover" between two satellite ground-tracks or spot track, one ascending and one descending (Fig. 4.7). The measured elevation difference at a crossover point is:

$$dH(t) = H_2 - H_1 + E \tag{4.14}$$

where H_2 and H_1 are the surface elevations at times t_2 and t_1, respectively, and E is the random measurement error, which includes errors in the altimeter-range measurement and in the determination of the vertical position of the orbit (Zwally et al., 1989). In the case of radar altimeters, the range measured is the average surface elevation in the pulse-limited footprint, whereas for a laser altimeter the elevation is obtained by fitting Gaussian functions to the returned waveforms and the maximum amplitude of the return marks the two-way travel time which translates into distance from the satellite. As satellite altimeters make discrete, non-continuous measurements, it will be rare to have measurements exactly at the crossover location, which means that surface elevations at the crossover points are obtained by interpolation.

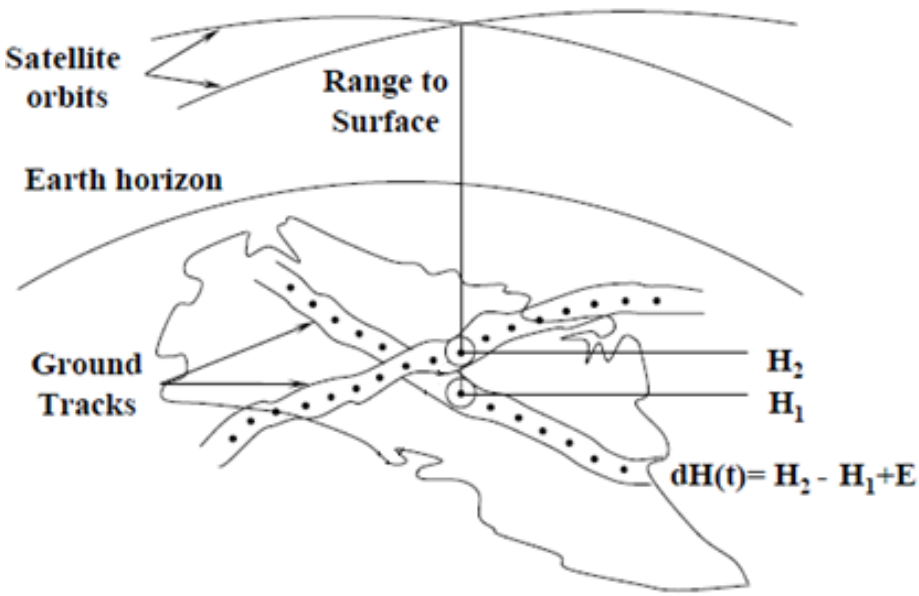

Fig. 4.7: Crossover method for measuring changes in surface elevation from radar altimeter measured elevation, H(t).

To obtain the rate of change of surface elevation from a set of crossover measurements, there are two methods.

The first method, known as the time series method, consists in comparison of measurements related to two distinct periods separated by a relatively large time interval (Δt). It is used when a sufficient number of measurements are available and the surface changing rate is the average crossover height difference divided by the time interval, $\left[\left(\sum(H_2 - H_1)_i\right)/N\right]/\Delta t$, where $(H_2 - H_1)_i$ is the elevation difference at the *i*-th crossover and *N* is the number of crossover.

The second method, known as *dH/dt* method, is appropriate for a set of crossovers that tend to have randomly distributed time intervals. The slope of a linear fit to the crossover differences, $dH_i = (H_2 - H_1)_i$, versus the time intervals, $dt_i = (t_2 - t_1)_i$, gives the thickening ($dH/dt > 0$) or thinning rate ($dH/dt < 0$).

The second method gives a more valuable result of elevation change for the entire time-interval considered, while the first one allows investigation of its temporal variability. A special case of the *dH/dt* method is the dual crossover method which was first used by Wingham et al (Wingham et al., 1998) to define Antarctica elevation change from ERS-1 measurements. Instead of combining ascending and descending tracks from a single orbital cycle, the elevation measurements from pairs of orbital cycles, acquired at times t_1 and t_2 are compared. In this manner two pairs of elevations can be considered: ascending track elevation h_{At_1} (measured during orbit cycle 1 at time $t = t_1$) and descending track elevation h_{Dt_2} (measured during orbit cycle 2 at time t = t2), as well h_{At_2} (ascending track, orbit cycle 2) and h_{Dt_1} (descending track, orbit cycle 1). The change in elevation between two orbital cycles at each point *x* is defined as:

$$\Delta h(x, t_1, t_2) = \frac{1}{2}\left[\left(h_{At_1} - h_{D_2}\right) + \left(h_{At_2} - h_{D_1}\right)\right] \tag{4.15}$$

The elevation change during one orbit cycle is supposed to be negligible. To see how the surface elevation changes over time, one of the orbital cycles can be chosen as a reference cycle. Pairing all other orbital cycles with the reference cycle, a time series of values of surface elevation $\Delta h(x, t, t_{ref})$ relative to the surface elevation measured during reference orbital cycle can be obtained from:

$$\Delta h(x, t, t_{ref}) = \frac{1}{2}\left[\left(h_{At} - h_{D_{ref}}\right) + \left(h_{At_{ref}} - h_{D}\right)\right]_{t=t_1..t_N} \tag{4.16}$$

Methods for deriving elevation time series from crossover data have evolved steadily over time. Early studies calculated crossovers between an early “reference” period and later measurements; the time-series of these differences gave the evolution of the surface height, which was often fit with a linear model. These studies often simultaneously solved for a sinusoidal seasonal cycle, assumed to be constant from year to year. More recently, researchers have fit auto-regressive models to the data (Ferguson et al., 2004), a technique which finds smoothly-varying functions that match the data to within tolerances appropriate to the accuracy of the data. These techniques can identify both seasonal and longer-term height variations, and are claimed to be less prone to bias induced by seasonal cycles than linear-fitting techniques.

Advantages
In case of a radar altimeter, the antenna is pointed at nadir and the pulse-limited footprint tends to be located at the closest surface lying within the beam-limited footprint, namely the first part of the reflected echo will come from the part of the surface within the beam-limited footprint that is closest to the satellite. Over flat surfaces, the closest point on the surface is at nadir, whereas over sloping or rough surface it is offset from nadir. Thus, the determination of the absolute surface elevation at nadir requires correction for slope-induced offset of the pulse-limited footprint from nadir. The same problem occurs also in the case of laser altimeters. However, for the purpose of studying elevation changes, correction for slope-induced errors is not necessary because the pulse-limited footprint is usually located at the same place on the surface due to the fact that the satellite is at the same position (the intersection of the two orbits). Thus the slope errors cancel, and any difference between the two measurements reflects elevation change.

Disadvantages
The main drawback is that the method provides information on elevation change only on crossover points. In addition, the location of the measurements is still determined by the surface slope, the footprint width and the pointing angle, so significant difficulty remains in measuring elevation changes for outlet glaciers, where the crossovers are preferentially located on the surrounding high points. The error in elevation determination can be caused by non-modelled or incorrectly modelled atmospheric errors. Orbit error, or uncertainty in the altimeter position, and inaccuracies in the model of Earth's gravity field also introduce errors into the derived elevations.

Since elevation data are discrete and not continuous, there will rarely be two elevation measurements at a crossover location, which means that interpolation is required to determine elevation values at the crossover location. Interpolation error can contribute to error in elevation determination, as the interpolation process may produce elevations inconsistent with the actual topography; this error will be higher in areas with higher topographic variability.

In case of radar altimeters, as mentioned in the section 4.2.2, a further complication comes about because microwaves can penetrate up to several metres into the snow pack. In addition, the measurements show difference due to volume echo induced errors between ascending and descending tracks.

4.4.2 The repeat-track method
Repeat-track analysis is a technique used to detect elevation change rate by comparing elevations from different times along the same repeat portion of a ground-track or spot track from one orbital revolution of the altimeter, also referred to as track segment (Zlotnicki et al., 1989). The track segments will not repeat exactly, so repeat-track analysis is an attempt to reduce the associated errors by estimating parameters that influence the elevation.

Description
In an ideal case, ground-tracks or spot tracks for altimeter satellites in repeat-track orbits would repeat exactly so that elevations along the track at one time could be directly compared to elevations along the same track obtained at a different time. However, differences in the altimeter pointing angle and orbital perturbations will cause cross-track differences which should therefore be compensated for within the repeat track analysis.

The unmeasured topography between near repeat-tracks needs to be considered when comparing elevations from different tracks. Slobbe et al. (2008) used a DEM to correct for the surface slope between the centre points of overlapping footprints. Using only overlapping footprints limits the slope-induced error, but it also limits the amount of data available for comparison. A method which uses along-track interpolation to restrict the DEM slope correction to the cross-track distance between two repeat-tracks has been applied in Moholdt et al. (2010a and b). For pairs of repeat-tracks, one profile is projected onto the other profile using the corresponding cross-track elevation differences from an independent DEM (Fig. 4.8a). Elevations are then compared at each DEM-projected point by linear interpolation between the two closest footprints in the other profile.

Ideally, a DEM or other external data should not be required to compare near repeat-track elevations. A set of repeat-tracks contain a mixed elevation signal from local topography and temporal elevation changes between the observations. Several methods have been proposed to separate elevation changes from topographic variations. For example, Pritchard *et al.* (2009) fitted a triangular plane to three elevation observations, and used the plane as reference for measurements falling inside this triangle, while Howat *et al.* (2008), Moholdt *et al.* (2010a) and Moholdt *et al.* (2010b) used rectangular reference planes determined by least squares fitting to segments of repeat-track of GLAS data. Regardless of the shape of the plane fitted, this approach eliminates the need of an external DEM. One potential disadvantage is the algorithms capability to separate surface slope from real elevation change signal, both of which are parameters derived within the algorithm. However, Moholdt *et al.* (2010b) showed that both along-track methods discussed here yield consistent results, and agree well with the elevation changes calculated using the crossover point method.

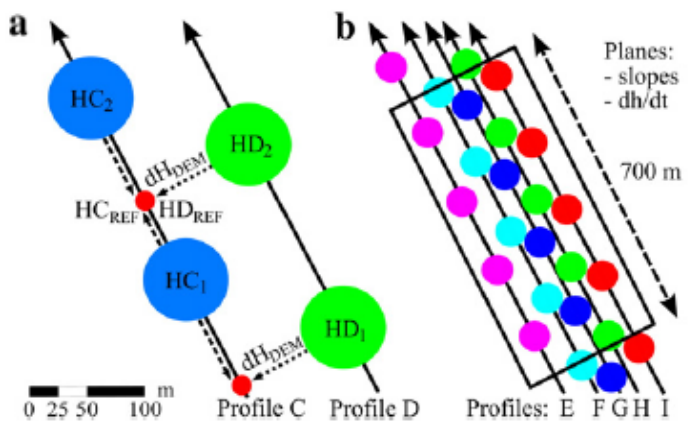

Fig. 4.8: (a) cross-track DEM projection ($HD_{REF}=HD_2+dH_{DEM}$) and linear interpolation to compare two repeat-tracks ($dh=HD_{REF}-HC_{REF}$), and (b) fitting least-squares regression planes to repeat-track observations to estimate slopes and average dh/dt (from Moholdt et al., 2010b).

Advantages

The main advantages of the repeat-track methods are an increased quantity and spatial distribution of elevation change measurements in comparison to the cross-track method. It increases the SNR of the analysis and increases the spatial resolution of the measurements. It

also allows working locally along track to seek for local scale phenomena much better than the sparse crossover points.

Disadvantages
One disadvantage when using radar altimetry over ice caps is that the surface and volume change with time depends on the surface state. The measured height is then variable according to the surface state variations or other volume echo intensity variations (linked to temperature changes impacting the medium's absorption). A disadvantage of the plane fitting method is that the potential elevation change signal between the two repeat tracks is present in the reference plane.

In Table 4.1 we provide short overviews on the algorithms applied to determine elevation changes at point locations from repeat altimetry.

Abbreviation	**XO-RepAlt**
Algorithm	Cross-Over for Repeat Altimetry.
Reference	Zwally et al. (1989).
Applications	Zwally et al. (1989), Wingham et al. (1998).
Description	Elevation change is determinated at the intersection of two altimeter passes.
Advantages	No need of slope errors correction.
Disadvantages	- Few intersection points; - The location of the point still depends on the surface slope, the footprint width and the point angle; - Interpolation is required to determine the elevation values at the interpolation points; - In case of radar altimeter, the signal can penetrate the snow pack.
Improvements	

Abbreviation	**DP-RT-RepAlt**
Algorithm	DEM-Projected correction method for Repeat Altimetry.
Reference	Moholdt et al. (2010).
Applications	Moholdt et al. (2010).
Description	One profile is projected onto a neighbouring profile by accounting for the cross-track slope using an external DEM. Elevations are then compared at each DEM-projected point by linear interpolation between the two closest footprints in the other profile.
Advantages	- Greater spatial distribution than cross-over analysis; - Uses the full potential of repeat track data.
Disadvantages	- Requires an external DEM; - Requires an assumption of constant slope if the DEM is not temporally consistent with the altimeter acquisition epoch; - Only functional at high latitudes where the cross track separation is not more than ±200 m.
Improvements	

Abbreviation	**RP-RT-RepAlt**
Algorithm	Rectangular Plane fitting method for Repeat Altimetry.
Reference	Howat et al. (2008), Moholdt et al. (2010).
Applications	Howat et al. (2008), Moholdt et al. (2010), Gardner et al. 2011.
Description	Fits rectangular planes to segments of repeat-tracks data by using the least-squares regression of the cross-track slope and a linear elevation change rate.
Advantages	- Does not require any external DEM; - Greater spatial distribution than cross-over method; - Uses the full potential of repeat track data.
Disadvantages	- Lower accuracy than cross-over method; - Assumes a linear elevation change rate during the altimeter acquisition; - The residuals of the plane regression contain remaining elevation variations which can not be ascribed to the assumption of planar slopes and an invariable elevation change rate; - Changing slopes may be mis-quantified as elevation changes.
Improvements	

Abbreviation	**TP-RT-RepAlt**
Algorithm	Triangular Plane fitting method for Repeat Altimetry.
Reference	Pritchard et al., 2009.
Applications	Pritchard et al., 2009.
Description	Fits a triangular plane to three elevation observations and uses the plane as a reference for measurements falling inside the triangle.
Advantages	- Does not require any external DEM; - Greater spatial distribution than cross-over method; - Uses the full potential of repeat track data.
Disadvantages	- Lower accuracy than cross-over method; - The potential elevation change value between two repeat tracks could be present in the reference plane.
Improvements	

Table 4.1: Details of the algorithms available for elevation changes from repeat altimetry.

4.5 Data pre-processing: the altimetry re-tracking algorithms

There are several variables, like the satellite orbit, the instrument attitutude, the effective atmospheric path length, the Earth tides, which have an effect on the surface elevation measurements and need to be corrected for. Among them, the most important is the lag in the radar pulse tracking system of the altimeter. This effect is corrected during the initial coarse processing on-board by applying the so-called retracking algorithms.

The altimeter estimates the range by the use of an algorithm which tracks the half-power point on the leading edge of the return wave-form (Fig. 4.4). The return wave form is digitised into equally spaced range "gates", where the centre gate should coincide with the half-power point on the mean wave form. The design of the tracking algorithm is based upon the assumption that the range to the surface changes slowly and predictably with time. This is valid for the ocean surface, and the algorithm positions the centre gate at the half-power point very accurately. An ocean surface can be represented by a horizontal planar mean surface with a

large number of scattering facets distributed normally around the mean surface. This has the effect of increasing the width of the leading edge of the return, which is used to estimate the significant wave height, whereas the range to the mean surface is associated with the half-power position on the leading edge (Ridley and Partington, 1988). However, over glacier ice the half-power point deviates substantially from the centre gate because of larger topographic variations and the volumetric scattering due to the penetration of the wave.

Since the telemetered range corresponds to the centre of the sampled return, further processing is required to correct the range estimate for ice-sheet wave forms. The procedure used is known as "**retracking**". The retracking correction consists of computing the distance of the leading edge of the return from the centre of the range window, or altimeter tracking gate, which defines the range over which the return is recorded at the satellite, and correcting the satellite range measurement (and surface elevation) accordingly. Fig. 4.9 explains the retracking correction schematically.

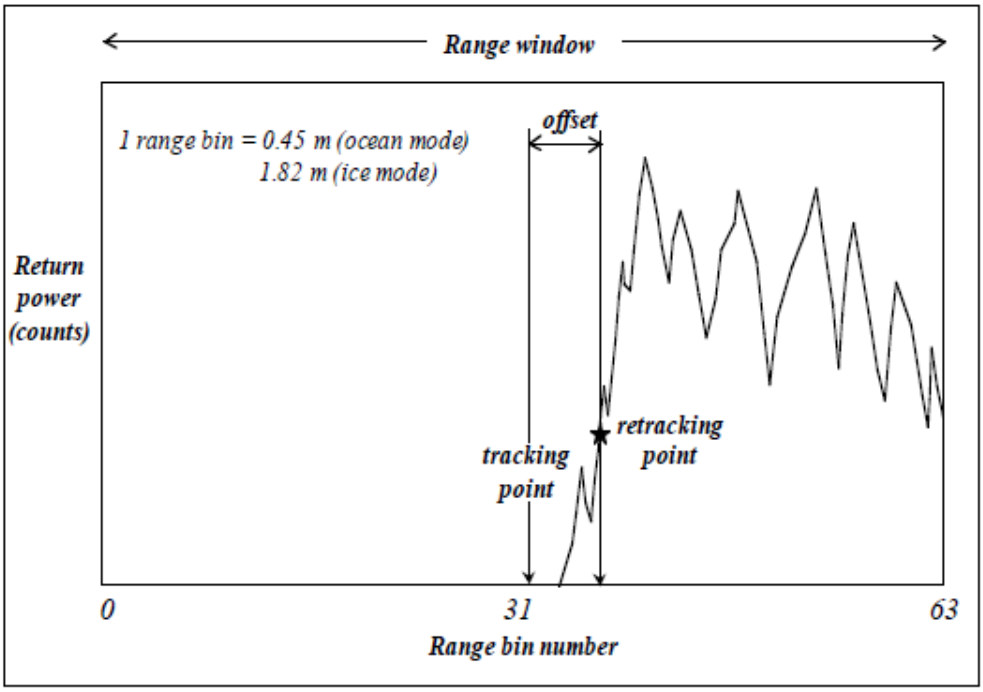

Fig. 4.9: Illustration of he retracking correction.

Originally, Martin et al. (1983) developed the first retracking algorithm for processing altimeter return waveforms for ice sheets. This algorithm, known as the **NASA algorithm**, processed al1 data acquired over the ice sheets from Seasat and Geosat to obtain corrected surface elevation estimates (Davis, 1996). The NASA algorithm fits a 5 or 9 parameter function to the altimeter return waveform. This algorithm is based upon Brown's surface-scattering model (Brown, 1977) which was developed to describe the shape of altimeter return waveforms over the ocean. Each function contains a parameter that defines the location of the waveform's leading-edge position, which is used to correct the altimeter range measurement. The 5-parameter function is used to fit single-ramp returns, while the 9-parameter function is used to fit double-ramp returns. Fig. 4.10 shows typical waveforms generated by the 5 and 9 parameters functions. Double-ramp returns occur with greater frequency near the ice sheet

margin where the ice is thinner. The double-ramp return is formed when two nearly equidistant surfaces within the altimeter's antenna beam width contribute to the received power at the satellite (Martin et al., 1983).

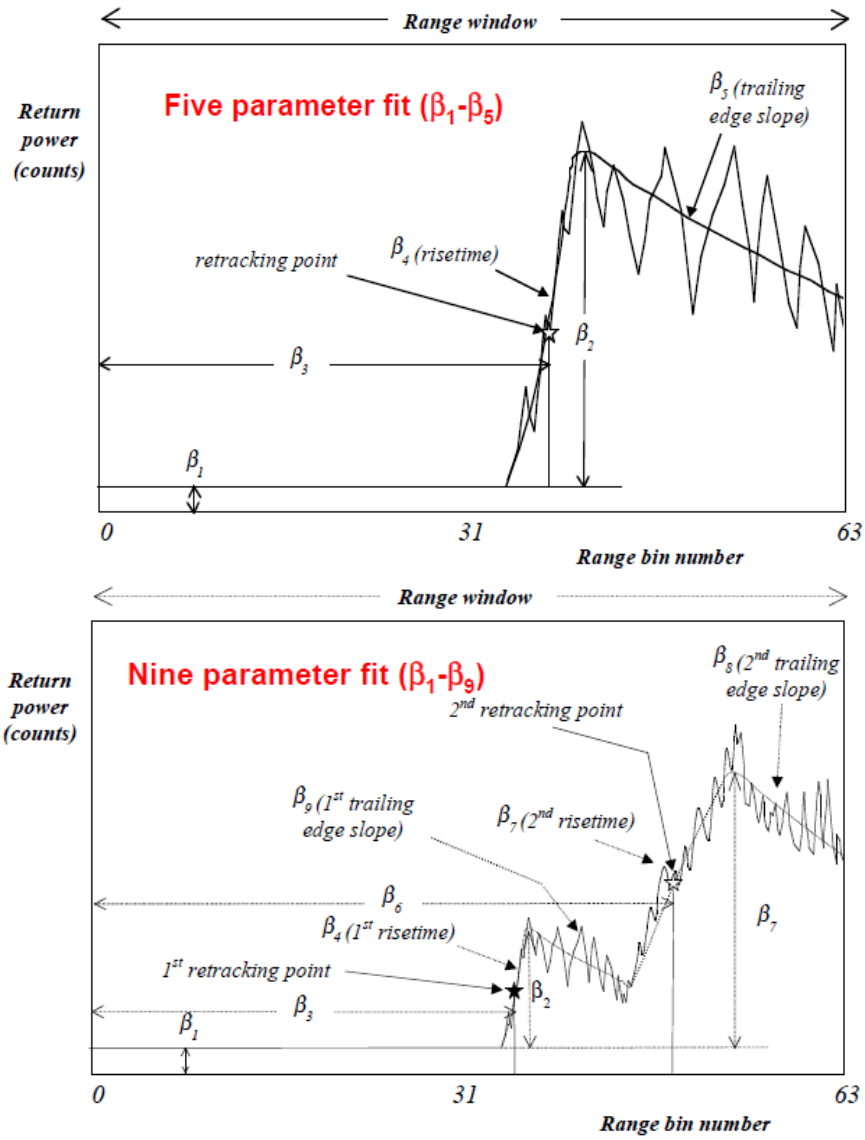

Fig. 4.10: Typical waveforms generated by the NASA algorithm's 5 and 9 parameter retracking functions.

The European Space Agency uses an empirical method, known as **ESA algorithm**, to process altimeter data from the ERS-l satellite (Wingham et al., 1986). The ESA retracking algorithm computes a rectangular box from the waveform samples that has an area and centre of gravity (COG) that is the same as the return waveform. The rectangular box is then aligned with the COG position and the retracking point is determined by linearly interpolating between adjacent samples of a threshold crossing (Fig. 4.11). Currently, threshold values of 25%, 50%, and 75% of the rectangle's amplitude are used to determine the leading edge position (Bamber, 1994).

The ESA algorithm is simpler computationally than the NASA algorithm. However, a disadvantage of the ESA algorithm is that it is not based on a physical model of the ice-sheet surface and the retracking location could therefore be sensitive to variations in surface properties. Also, the selection of one of the three threshold retracking locations is left to the individua1 user, and therefore is totally arbitrary.

Recent work has demonstrated that energy at altimeter frequencies can penetrate *5* to 10 m beneath the surface (Rott et al., 1993; Davis and Poznyak, 1993). Ridley and Partington (1988) and Davis and Moore (1993) have demonstrated that the shape of altimeter return over ice sheet is strongly influenced by volume scattering as well as surface scattering. To account for the altimeter signal penetration, Davis and Moore (1993) developed a closed-form analytical solution for the return power volume scattered from beneath the ice surface. The volume-scattering model was then combined with a surface-scattering model and used to accurately characterise variations in the shape of ice- return waveforms caused by differing contributions of surface and volume scattering. Davis (1993) used the surface/volume-scattering model to develop an algorithm, referred to as the **S/V algorithm**, to process ice-return wavefoms. Currently, this is the only altimeter processing algorithm that includes volume scattering to describe ice- return waveforms and it is used as a reference for determine the relative accuracy of the NASA and ESA algorithms when subsurface volume scattering occurs (Davis, 1996). The results reported in (Davis, 1996) show that the ESA algorithm with the 25% threshold value, $ESA_{25\%}$, produced slightly higher surface elevations than the S/V algorithm. The NASA retracking algorithm produced lower surface elevations than the S/V algorithm, with average differences ranging from -0.3 to -0.9 m. The lower NASA elevations can only account for a portion of previously reported differences between altimeter and geoceiver surface elevations, suggesting that the remainder is probably due to orbital differences.

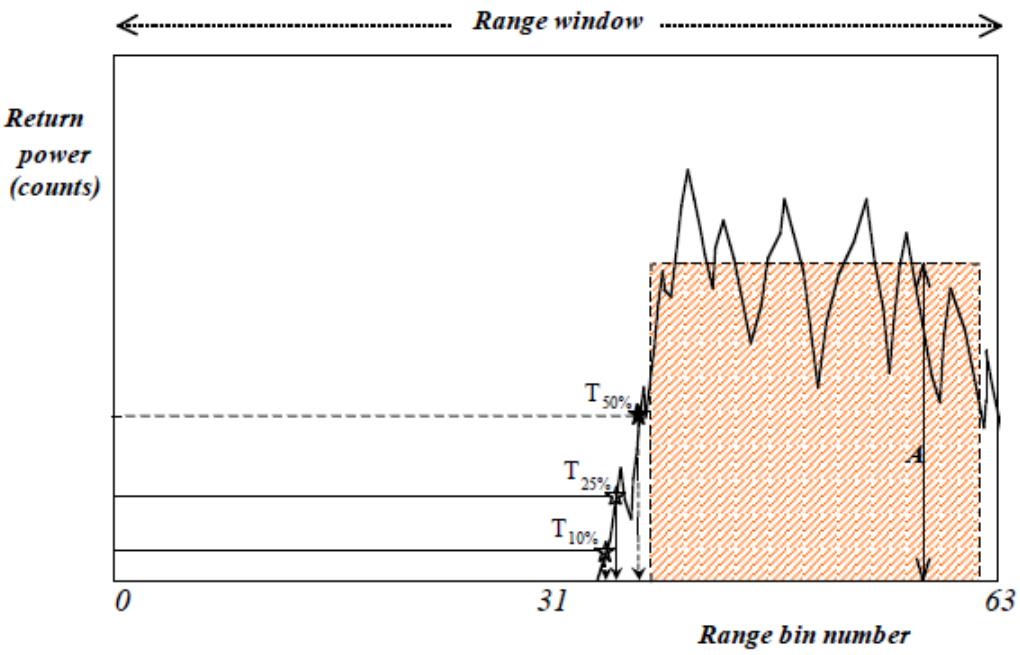

Fig. 4.11: An example waveform with COG retracking variables.

The 9-parameter NASA function was determined to approximate and the volume-scattering altimeter waveforms. The original purpose of the 9-parameter function was to fit double-ramp waveforms that occur when two nearly equidistant surfaces within the altimeter's antenna beamwidth contribute to the received power. However, David (1996) demonstrated that an extremely large percentage of the NASA waveform fits the East Antarctica plateau due to the volume-scattering nature of the waveforms in this region.

Furthermore, it is important to know if penetration varies over time, thus requiring a seasonal correction to data retracking. If the scattering of the pulse is altered significantly by seasonal conditions, erroneous elevation changes may be calculated.

4.6 Expected performance gains by future developments

The algorithms described in section 4.4.2 for pulse-limited radar altimetry and laser altimetry are relatively mature, and main performance gains are expected to arise through improved instrumentation, specifically Croysat2, Sentinel 3 and Icesat-2. These will lead to finer footprints, increased density of observations, and reduced data loss in regions of mountainous terrain. Cryosat-2 has recently been placed into orbit and it is the first satellite equipped with a SAR Interferometric Altimeter (SIRAL) to enhance the radar's horizontal resolution to 250 m while allowing for precise measurements of changes as small as a few centimetres. A further benefit of this satellite is, that it will allow for the highest coverage available for an altimeter with measurements capable of being taken up to 88° N/S latitude.

Whereas conventional radar altimeters send pulses at intervals long enough that the echoes are "uncorrelated" (about 500 µs), the CryoSat-2 altimeter sends a burst of pulses at an interval of only about 50 µs. The returning echoes are correlated and, by treating the whole burst together, the data processor can separate the echo into strips arranged across the track by exploiting the slight frequency shifts, caused by the Doppler effect, in the forward- and aft-looking parts of the beam. Each strip is about 250 m wide and the interval between bursts is arranged so that the satellite moves forward by 250 m each time. The strips laid down by successive bursts can therefore be superimposed on each other and averaged to reduce noise. This is known as the SAR (Synthetic Aperture Radar) mode. In order to measure the arrival angle, a second antenna receives the radar echo simultaneously forming SAR Interferometry acquisition mode. When the echo comes from a point not directly beneath the satellite, there is a difference in the path-length of the radar wave, which is measured. Simple geometry then provides the angle between the 'baseline' joining the antennas and the echo direction. The difference in path length is tiny – up to a wavelength of the radar wave (2.2 cm) – and has to be accurately determined in an overall measurement range of 720 km. Thus, combining these two techniques Cryosat-2 is able to point down the location of the echo on sloping surfaces, such as those found around the edges of ice sheets.

The performance of the CryoSat-2 SAR Interferometer instrument over the continental ice sheets of Antarctica and Greenland have been analysed in Shepherd et al. (2010). The authors were able to confirm that with the corrected data products the system performance of CryoSat-2 will meet or exceed its specification over the continental and marine parts of the ice sheet.

The Sentinel 3 altimeter will provide data on an operational basis in support of services that have been developed with ERS and Envisat since 1991. The altimeter part component of the mission will further complement that of Jason and others to contribute to a worldwide

operational oceanographic service (Rosmorduc et al., 2011). Also this altimeter will have the capability to operate in SAR mode which can be used alternatively to the more conventional pulse-limited mode, called LRM (Low Resolution Mode). Together with this acquisition mode, the altimeter will present another extra feature which can be used independently or in combination with the SAR mode: the open-loop tracking mode. This will be used mainly over discontinuous surfaces (like land sea transitions) or rapidly varying topography like ice margins. In this mode, the altimeter's tracking window will be controlled based on a priori knowledge of the surface height, from existing high-resolution global digital elevation models, combined with knowledge of the location of the satellite from the satnav receiver. The main advantage is that the measurements are continuous, avoiding the data gaps typical of closed-loop tracking, which has problems in tracking the rapid topographic changes at coastal margins and in mountainous regions (ESA Bulletin 131). Typical operation over different surface types is summarized below (Mavrocordatos et al., 2007).

Surface type	Instrument operation	
	Mode	*Tracking*
Open Ocean	LRM	Closed-loop
Coastal Ocean	SAR	Open-loop
Sea Ice	SAR	Closed loop
Ice sheet interiors	LRM	Closed-loop
Ice sheet margins	SAR	Open-loop
Rivers/Lakes	SAR	Open-loop

Table 4.2. Sentinel 3 instrument operation summary.

4.7 Error budget estimates

There are several potential error sources originating from the EO data themselves that have effect on the surface elevation measured. To achieve the best possible accuracy, the effect of these variables must be compensated for. Thus the data has to be corrected for:

- uncertainty in satellite orbit (also known as radial uncertainty) due to gravity anomalies of the Earth as well as the gravity of the Sun and the Moon;
- uncertainty in satellite attitude (roll, pitch and yaw rotations) due to fuel consumption, solar panel orientation and other factors;
- lag of the leading-edge tracker, waveform saturation and surface scattering variations;
- dry atmosphere mass due to gases in the atmosphere that slow the altimeter signal;
- water vapour which effect is to slow the altimeter signal, due to the polarizability of the water molecules;
- ionosphere delay (frequency-dependent), is due to the free electrons in the ionosphere;
- solid Earth tides due to gravity pull of the Moon and the Sun and to the variations of the Earth's rotation axis; and ocean loading tides.

When the altimeter is applied to continental surfaces, such as ice surface, the error budget is greater compared to when the altimeter operates over oceans and some specific corrections should be applied.

The first difference is due to the kilometre-scale topographic features and surface slope that induce several problems. As described in section 4.3, the altimeter measures the range between the antenna and the nearest point of the surface. This point is at the nadir only when the topography is very flat, otherwise it is shifted in the up slope direction of the surface. This error, pointed out by Brooks et al. (1978) or Brenner et al. (1983) depends on the square of the surface slope. The correction can be done either directly on the height at the nadir or by relocating the impact point in the up slope direction (Brenner et al., 1983; Roemer et al., 2007; Brenner et al., 2007; Remy et al., 1989). The limitation is due to the lack of knowledge of the 2-D surface slope that can be derived from an external base (Bamber, 1995) or by iteration from an a priori DEM obtained by fitting a bi-quadratic form over the local area (Remy et al., 1989). Nevertheless, data processing can be developed to correct for (or minimize) these errors so that altimeter measurements reach a very good accuracy. However, due to the inaccurate repetitivity of the orbit, the cross-track slope misknowledge is still one of the greatest limitations for the time series analysis. The kilometre-scale feature also affects the tracking system which pre-positions the receiving window based on previous measurements and that cannot follow the irregular surface topography. The on-board estimate is thus inaccurate and retracking is needed (see section 4.5). Finally, due to the kilometre-scale footprint, the small-scale topographic features also affect the waveform shape that in turns via the retracking affects the height restitution so that the final precision is limited (Wingham et al, 1995).

The second difference with classical ocean processing lies in the penetration of the radar wave within the snow pack, as described in sections 4.2.3. In Ku-band (13.6 GHz or wavelength of 2.3 cm), the classical altimetric band penetrates within the dry and cold snowpack so that the reflection comes both from the surface (surface scattering, section 4.2.2) and subsurface layering (volume scattering, section 4.2.2). As mentioned in the section 4.2.3, this was first pointed out by Ridley and Partington (1988) who modelled the waveform shape and detected a distortion due to volume scattering. The induced error on the height measurement is between a few tens of centimetres and a few metres and is probably the most critical one, even if its effects can be minimized thanks to retracking techniques (see section 4.5). The error is difficult to model because the snow is a very complex and variable medium: it is thus the major limitation for the time series interpretation.

Finally, to get continuous and consistent elevation time series for calculation of the elevation change, observations recorded by successive satellites are needed. As a consequence cross-calibration between the different measurements is a main point to achieve. Multi-mission crossover differences are used the remove the inter-satellite biases during the periods of mission overlap.

5. Elevation changes from DEM differencing

5.1 Introduction

For DEM differencing, the major algorithms presented in this chapter are a part of the **pre-processing** stage. In order to assure that multi-temporal elevation data actually stem from corresponding ground points, i.e. have exactly the same horizontal coordinates in a reference system, elevation data sets require co-registration. This minimizes potential systematic errors (biases). After co-registration, biases may remain related to the acquisition strategy and DEM creation. For example, ASTER and SPOT DEMs have shown to have errors related to pointing inaccuracies of the sensors (Berthier et al., 2007; Nuth and Kääb, 2011). These should be analyzed, typically by looking at along track and cross track geometries. However, as these types of biases are sensor or even scene-dependent, they are not considered as uniformly applied in all situations and therefore will remain as a suggested work-flow rather than a defined algorithm in the Glaciers_cci project.

After co-registration between the DEMs, the main **elevation difference** algorithm is applied by simply differencing the two DEMs. The DEM differences (sometimes called dDEM, differential DEM) have three important error characteristics: voids, noise and bias. At all locations where at least one DEM has a void also the dDEM will have a void (no-data value). There are many reasons for these voids but all depend primarily on the methods used for DEM generation (e.g. failed correlation for optical stereo, lack of phase coherence for InSAR, perspective obstruction by adjacent terrain). Secondly, dDEMs are affected by noise or random errors. These are typically evaluated statistically using the root sum of squares (RSS) or standard deviations of the vertical differences between DEMs on stable terrain. Last, potential un-removed systematic bias may remain. These biases can be evaluated if a third dataset is available (e.g laser altimetry). By performing co-registration between all three datasets, the residual remaining by triangulation of the 3 co-registration vectors is an estimate of the un-removed systemic bias. Last, as a **post-processing** step, dDEMs may be filtered or smoothed. This will also be a site/data specific task and thus Glaciers_cci will not particularly focus on these algorithms. However, resampling to larger grids may be a Glacier_cci standard when providing data, to abide by copyright laws.

5.2 Scientific background on DEM generation

Digital Elevation Models are spatially continuous representations of the Earth surface and may be generated using stereo optical images, laser pulse scanning or radar interferometry on either terrestrial, aerial or satellite platforms. This variation of acquisition methods results in a plethora of data that has different attributes. Since Glaciers_cci will focus on the differencing of this type of data, and not specifically on the generation of DEMs, this section will only provide a short overview of the acquisition methods and DEM generation.

5.2.1 Stereoscopic DEMs

Stereoscopic DEMs are generated using photogrammetric principles. In along-track stereo, a *parallax* measurement gives the difference between the projected stereo rays of the same object onto the Earth's ellipsoid and can be converted to height provided the observer positions, the sensor pointing angles and camera parameters are known (Lillesand et al., 2004). Examples of satellite stereoscopic geometries are nadir and backward looking sensors (e.g. ASTER), forward and backward looking sensors (e.g. SPOT-5 HRS), forward, nadir and

backward looking sensors (ALOS PRISM), or sensors that can be freely rotated to any stereo geometry (e.g. Ikonos, WorldView, Pleiades), all of which are pushbroom or line scanners.

Satellite stereoscopy is slightly more complicated than traditional photogrammetry from aerial frame imagery due to the typical pushbroom acquisition strategies and to the greater effect of Earth's rotation and curvature from the higher flying height of satellites (Toutin, 2004; Kääb, 2005). Image orientation may be solved from Ground Control Points (GCP) and a satellite orbital model (Toutin, 2004) that is implemented in commonly available software e.g. PCI Geomatica®. Automated approaches are becoming more common for deriving the relative and/or absolute orientation of stereo images using direct measurements of the satellite's attitude and position (i.e. pointing information, auxiliary and ancillary data) (for more details, see Schenk, 1999). Common examples of automatically generated satellite stereo DEMs that are available today include: the ASTER DEMs produced by LPDAAC using the SilcAst software (product AST14) (Fujisada et al., 2005) and the SPOT5-HRS DEMs (Bouillon et al., 2006; Korona et al., 2009), as for instance available through the IPY SPIRIT (SPOT 5 stereoscopic survey of Polar Ice: reference Images and Topography) project.

Errors associated with stereoscopic DEMs are related to the errors in the orientations of the stereo-scenes, either from GCP-based solutions or direct on-board determination, and to the ability of the matching algorithms to locate the corresponding points on two or more images. Errors in the parallax determination are both due to imperfect matching procedures and to imperfect image quality such as from lack of visible contrast, cloud cover, shadows and topographic distortions. Errors related to the parallax matching often result in blunders and voids rather than bias, whereas errors related to the image orientation will typically induce bias. ASTER DEM uncertainty is reported to be typically within 15 to 60 m RMSE in the vertical depending upon terrain type (Toutin, 2002, 2008; Kääb et al., 2002; Hirano et al., 2003; Kääb, 2005; Fujisada et al., 2005) and between 15 and 50 m horizontally (Fujisada et al., 2005; Iwasaki and Fujisada, 2005). SPOT5 uncertainty is reported to be between 10 and 25 m vertically (Berthier and Toutin, 2008; Korona et al., 2009) and greater than 15 m in the horizontal (Bouillon et al., 2006; Berthier and Toutin, 2008). In relation to pushbroom sensors (e.g. ASTER and SPOT5 HRS), it has been shown that variation in the satellite's attitude induces biases within the raw images acquired as well as final DEMs produced (Leprince et al., 2007; Berthier et al., 2007; Nuth and Kääb, 2011).

5.2.2 Interferometric DEMs

Interferometric DEMs are generated through synthetic aperture radar (SAR) interferometry which uses the phase differences between two radar images acquired with a small base-to-height ratio. These phase differences are the photogrammetric equivalent to a "parallax" measurement allowing retrieval of topography (Rosen et al., 2000). Examples include the SRTM DEM, acquired in February 2000, which mapped the Earth from 60º N to 56° S using single-pass SAR interferometry (Farr et al., 2007), and the ongoing TanDEM-X Mission.

Many glacier elevation change studies have used the SRTM as a base dataset to compare to both newer and older data products (Rignot et al., 2003; Larsen et al., 2007; Schiefer et al., 2007; Paul and Haeberli, 2008). Typically reported vertical uncertainties of the dataset are ±10m which is lower than the mission standards of ±16m (Rodriguez et al., 2006). However, vertical biases are present due to instability of the sensor and/or platform (Rabus et al., 2003), and elevation-dependent biases have also been shown due to penetration of the C-band radar waves (centre frequency at 5.3 GHz) into snow and ice (Rignot et al., 2001; Berthier et al.,

2006). Rignot et al. (2001) determined that the phase centre of the C-band signal return was 1 to 10 m into the surface depending upon the snow conditions (i.e. dry vs. wet) in Greenland and Alaska. In Svalbard, the volumetric phase centre of the C-band varied from 1 to 5 m along a profile from ablation to firn zones, respectively (Müller, 2011). Corrections for depth penetration are hardly used for the SRTM data, and it is extremely difficult to correct for as knowledge of the snow conditions at the time of acquisition is required and yet hardly available. Nonetheless, this bias is crucial to understand when interferometric DEMs are used in differencing. Future potential in determining this bias may entail the comparisons between the C-Band and X-Band SRTM datasets.

5.2.3 Laser scanning DEMs

DEMs generated from laser altimeters are at the present time typically restricted to airborne platforms and are therefore less widespread than satellite based DEMs. However, their accuracy is unprecedented and therefore provide great potential for glacier elevation changes (Geist et al., 2003; Geist et al., 2005; Aberman et al., 2010). Elevation acquisition from laser pulses is described in section 4.3.2. Laser scanning uses the same principles but collects data not only along a profile (as ICESat), but also across track (swath). Depending upon the flying height and sampling frequency, airborne laser scanners can typically acquire a horizontal point density on the order of 1-2 metres. The accuracy of the returned elevations are typically a function of the accuracy of the laser range determination and of the GPS position of scanner through time. Laser scanning DEMs are not globally available, and are only used as a secondary DEM source for those particular glaciers from which they are available.

5.3 Elevation changes from multi-temporal DEMs

Glacier elevation changes can be derived from multi-temporal DEMs through differencing. DEM differencing provides a more-or-less complete spatial representation of the glacier changes in height (provided no data voids), but has a coarse temporal resolution. This is because a greater time between data acquisitions is required to estimate significant changes due to the accuracy of the DEMs and due to seasonal elevation variations of the glacier surface as a result from accumulation and ablation. To compensate for both DEM accuracy and natural seasonal height variability, glacier elevation changes from DEM differencing are typically derived as long term averages (i.e. >5 years). The shortest period between successive DEMs is dependent upon the accuracy of the DEMs and the magnitude of the changes.

Glacier elevation changes are used for analyzing changes in the geometry of glaciers (Hagen et al., 2005) and for estimating volume and mass changes (Kääb, 2008; Berthier et al. 2010; Nuth et al., 2010), and possibly their relation to climate. However, the estimation of volume and mass changes requires some standard assumptions about the density of the changes which is difficult and rarely measured. Furthermore, an elevation change at a point on a glacier is the result of both climatic (surface mass balance) and dynamic (glacier flow) processes, and therefore a direct translation into responses induced by climate change is difficult. This is sometimes made easier when integrating all changes over individual glaciers (i.e. mean elevation change thickness) as the dynamic component of ice submergence and ice emergence cancels due to mass conservation within a land terminating glacier system. For these land terminating glaciers, this has led to a large effort to control field derived surface mass balances of glaciers (Andreassen, 1999; Elsberg et al., 2001; Cox and March, 2004; Thibert et al., 2008), but also to provide control and calibration for surface mass balance models (Huss et al., 2009). However, if the glacier is marine terminating and contains ice loss to calving processes, the mean elevation change will include both the surface mass balance component

as well as the component related to the calving loss of ice. In some instances, glacier elevation changes from DEM differencing have been combined with surface mass balance modelling to estimate the calving component to volume change (Nuth et al., 2011; Gardner et al., 2011). In summary, the algorithms presented for DEM differencing will focus on the **pre-processing** and generation of elevation changes, rather than the translation of elevation changes into volume and mass changes which require several assumptions.

While the approach of DEM differencing is straight-forward (i.e. subtraction of the older DEM from the newer DEM), the results of this differencing can be misleading due to bias in one or both of the DEMs and to the geometric co-registration of the DEMs to each other. DEMs can be generated from optical, radar or lidar data, and therefore variation in the errors and biases in any of these products may propagate into the elevation changes. Thus, the goals in terms of algorithms will be to outline the best procedures for (1) combining the various datasets and (2) for detecting and correcting (if possible) potential biases between the datasets. Further, we aim for universal procedures that can be highly automated and are flexible for the various input data sources used to generate differential DEMs.

5.4 Algorithms for DEM differencing

For DEM differencing, the elevation change algorithm is simply subtraction of the two grids and therefore requires little attention. One of the DEMs will have to be re-sampled to the cell size of the other DEM. Any resampling technique more advanced then nearest neighbour should be used (i.e. bilinear interpolation), because nearest neighbour resampling, though retaining the original measurements, will inherently compare ground elevations representing different locations and areas (pixel sizes). Therefore, despite the smoothing of higher order interpolations (e.g. bilinear), these methods are necessary to ensure comparison of similar ground locations and areas to limit the effect of mis-registrations on DEM differences. We here focus on the pre-processing steps to improve the accuracy (remove bias) and precision of DEM differencing measurements.

The accuracy of glacier elevation differences from multi-temporal DEMs is dependent upon the individual accuracies of each of the DEMs and the geometric alignment between the DEMs. For DEMs that contain sufficient non-glacier terrain (e.g. > 10% of the scene), DEM difference statistics in this terrain, assumed stable within the time period, can be used for co-registration and bias-assessments. The initial (and universal) pre-processing step for deriving glacier elevation changes from DEM differencing is thus co-registration of the DEMs to each other. After co-registration, higher order biases can be investigated and removed if possible. A suggested work-flow for pre-processing DEMs before differencing is seen in Fig. 5.1. An overview of the key characteristics of this algorithm is provided in Table 5.1.

5.4.1 A universal co-registration correction

Two DEMs of the same surface that are not perfectly aligned experience a characteristic relationship between elevation differences and the direction of the terrain (aspect) that is precisely related to the x-y-shift (co-registration) vector between them. Figure 5.2 shows a schematic drawing and a real example where one DEM is shifted to the second. Resulting elevation differences (dh) are larger on steeper slopes due to the relationship of the magnitude (a) of the shift vector and the elevation errors to the tangent of the slope of the terrain (α):

$$\tan(\alpha) = \frac{dh}{a} \tag{5.1}$$

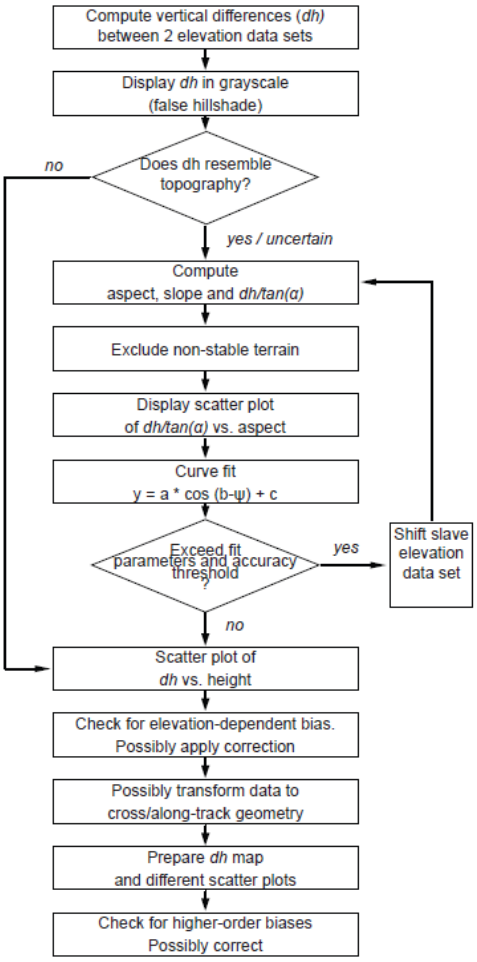

Fig.5.1: A suggested methodology for comparing DEMs or elevation products for glacier elevation change (Nuth and Kääb, 2011).

For the assumed shift in x-direction, *dh* is positive on eastern and negative on western slopes, exemplifying the relationship between the shift direction and terrain aspect (Ψ). Because Ψ is usually defined circular from the north (azimuth), the direction of the shift can be modeled using a cosine of the difference between Ψ and the horizontal directional component of the co-registration vector. Combining this with the relation described by Eq. 5.1 derives the full analytical solution by relating the elevation differences to the elevation derivatives slope and aspect (Kääb, 2005):

$$dh = a \cdot \cos(b - \psi) \cdot \tan(\alpha) + \overline{dh} \qquad (5.2)$$

where *dh* is the individual elevation difference, *a* is the magnitude of the horizontal shift, *b* is the direction of the shift vector, α is the terrain slope, Ψ is the terrain aspect and $\overline{dh}$ is the overall elevation bias between the two DEMs. Slope and aspect can be calculated by any standard GIS or mathematical software, and different approaches exist depending upon

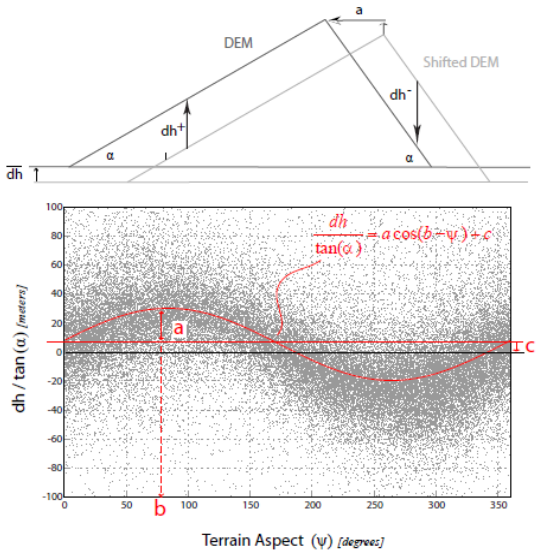

Fig. 5.2: Top: 2-D scheme of elevation differences induced by a DEM shift. Bottom: The scatter of elevation differences between 2 DEMs showing the relationship between the vertical deviations normalized by the slope tangent (y-axis) and terrain aspect (x-axis). The example is the DEM differences between the 2002 and 2003 DEM shown in Fig. 5.3. The equation for the solved sinusoidal curve fit is shown along with the three unknown solution parameters, a, b and c. Reproduced from Nuth and Kääb (2011)

application. In this case, the finite difference method is more appropriate then the D8 method (Wilson and Gallant, 2000). To remove the error dependency on slope due to a geometric mis-registration, we normalize the vertical deviations by dividing by the tangent of slope at that pixel. This produces a clean sinusoidal relationship between elevation difference and aspect (Fig. 5.2). The transformation of Eq. 5.2 after slope normalization is:

$$\frac{dh}{\tan(\alpha)} = a \cdot \cos(b - \psi) + c \tag{5.3}$$

where:

$$c = \frac{\overline{dh}}{\tan(\alpha)} \tag{5.4}$$

Three cosine parameters (a, b and c) are solved using least squares minimization where the amplitude of the cosine (a) is directly the magnitude of the shift vector, b is the direction of the shift vector and c is the mean bias between the DEMs divided by the mean slope tangent of the terrain (see Fig. 5.2). Because the solution to this actually analytical relationship is solved using the terrain which is not an analytical surface, the first solution may not be the final solution and iteration of the process is required to arrive at an ultimate solution. For automation, the iteration can be halted when the improvement of the standard deviation is less than 2% or if the magnitude of the solved shift vector is less than 0.5 m. The final correction is applied to the corner coordinates of the un-registered DEM by solving the x- and y-components of the shift vector from the magnitude (a) and direction (b). The mean bias

determined by inverting Eq. (5.4) is added to the DEM using an estimate of the mean slope of the terrain used to solve Eq. (5.3).

The co-registration procedure outlined here is not restricted to DEMs, but to datasets that contain a sufficient amount of stable non-glacier terrain to solve with Eq. (5.3). In particular, ICESat can be used for this despite the smaller amount of points available (Nuth and Kääb, 2011). This provides a framework for global co-registration using ICESat as a reference.

Last, alternate methods for co-registration involve the basic principles in image matching techniques (described in Section 6.4) but uses entire DEMs rather than sub-image search windows (e.g. Berthier et al., 2007). These algorithms, in principle, minimize the population of elevation differences over stable terrain in a least-squares approach to find the statistical co-registration adjustment. The algorithm is computationally expensive as it requires numerous iterations and resampling of rather large data sets into the sub-pixel domain in order to derive sub-pixel co-registration corrections. In addition, to achieve sub-pixel accuracy, resampling and interpolation is required while our algorithm returns sub-pixel precision directly. Glaciers_cci will not directly incorporate this algorithm, because the previous algorithm is, in principle, the analytical solution to a mis-registration. The algorithm may however be used by partners in the round-robin exercise which would allow comparison.

Abbreviation	**DEM CR**
Algorithm	Digital Elevation Model Co-Registration
Reference	Kääb (2005), Nuth and Kääb (2011)
Applications	Nuth and Kääb (2011)
Description	The analytical solution to a mis-registration of terrain data relate the co-registration correction vector to terrain slope and aspect using all measurements over "assumed" stable terrain.
Advantages	- Simple, robust method which can be applied using a GIS and any curve-fitting software. If no curve-fitting available, the co-registration parameters can be read directly off the graph in Fig. 5.2. - Requires few iterations (generally less than 5, typically 2-3).
Disadvantages	- Must have a sufficient sample and distribution of elevation differences over stable terrain covering all aspects, and particularly higher slopes. I.E. In Svalbard, less than 10% of an ASTER DEM was sufficient (Nuth and Kääb, 2011) - The solution is not well defined for low sloped terrain (<5 degrees)
Improvements	- The threshold for exiting iteration can be investigated. - A standard removal threshold for low slopes has not been undertaken.

Table 5.1: Details of the algorithm used for co-registering DEM pairs.

5.4.2 Higher-order biases

Higher order biases are rather source/sensor dependent, and therefore not universally applied. However, higher order biases are specifically important for glacier elevation changes. For example, an elevation dependent bias which may arise due to an uneven distribution of ground control points (GCPs) or to inaccurate satellite parameters, may have significant implications for glacier elevation changes because glaciers spread a range of altitudes which define their ablation and accumulation areas (Fig. 5.3). These biases may be corrected for

using linear or polynomial corrections. However, elevation biases may also result solely from differences in the resolution of the DEMs compared (Paul, 2008). Either way, these types of biases shall be investigated on a case-by-case basis in the **pre-processing** stage prior to applying the **elevation change** algorithm.

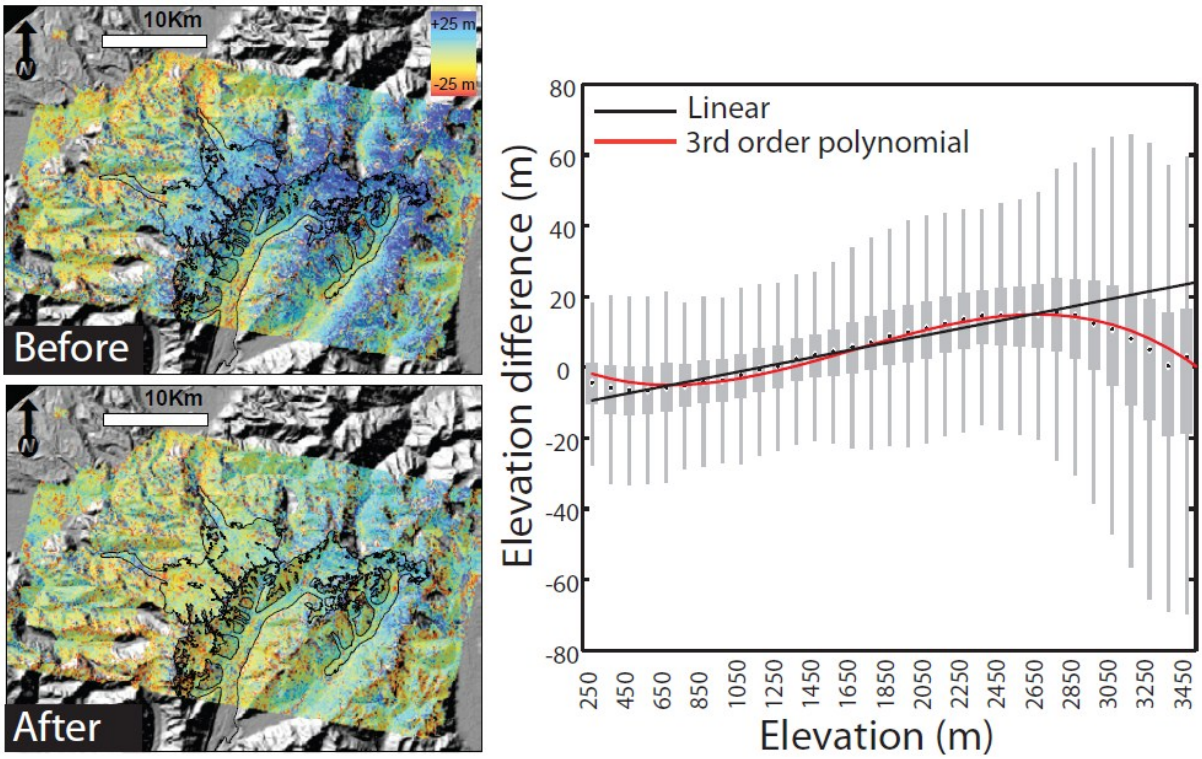

Fig. 5.3: Example of elevation differences between two ASTER DEMs in New Zealand before and after applying an elevation dependent bias correction using a 3rd order polynomial. The two DEMs were first co-registered before checking for an elevation dependent bias. Glacier extents are indicated by black outlines. Examples are from Nuth and Kääb (2011).

5.4.3 Elevation changes derived through combination DEM / altimetry

Satellite altimeter elevation measurements can also be differenced to a DEM from an earlier date. The advantage of this approach is that it yields an estimate of mean elevation change over periods longer than the relatively short life-spans of satellite missions. The downside is that the accuracy of the elevation change estimate is dependent on the accuracy of both measurements, and not only the precision of the satellite instrument. Some studies have compared GLAS measurements to historic DEMs to derive long term measurements (Sauber *et al.,* 2005; Kääb, 2008; Nuth *et al.,* 2010). The key difference in this approach is that a full spatial distribution of elevation changes is not provided, and therefore the approach relies on estimating average elevation changes per altitude bands based upon the spatial distribution of ICESat points.

5.5 Expected performance gains by future developments

The major gains expected for DEM differencing will result from the implementation of the co-registration algorithm. This algorithm (section 5.4.1) is analytically defined and may be universally applied provided a proper representation of the terrain. Major gains in this

algorithm may be automatically determining whether the terrain (slope and aspect) available is sufficient to analyze and detect DEM mis-registration. Actually, only half of the aspects may be required to determine proper phase and amplitude of the cosine in Eq. 5.3. Also, low-slope terrain does not properly solve the algorithm and removal of low-slopes with a threshold or histogram analysis may provide proper solutions faster.

The computational efficiency of the co-registration algorithm as compared to DEM matching is outstanding (i.e. < 5 iterations vs. > 25 iterations, respectively). However, for large datasets (i.e. millions of pixels), the solution to the algorithm is over defined and the sample size may be limited. Future progressions for automating this algorithm may entail randomly selecting the proper terrain for a much smaller sample size than using each individual pixel. How large this sample must be has to be defined.

5.6 Error budget estimates

Errors remaining in a differential DEM are a composite of errors from both DEMs as well as the quality of the co-registration between the DEMs. Quantification of errors in dDEMs will generally use available stable terrain (i.e. non-glacier) within the DEMs. The random error is generally a function of the combined precision of the individual DEMs. For optical stereo DEMs, this will for example, be related to the base to height ratio of the stereo acquisition, or from the internal image matching algorithms used to derive parallax measurements. The random error is typically quantified by the standard deviation or RMSE of elevation differences in these stable terrain areas. Typical random errors of satellite derived DEMs lie on the order of 5-15 metres though generally much less for DEMs derived from aerial photography and aerial laser scanning. The accuracy of the co-registration (or bias remaining after co-registration) can be determined by incorporating a third dataset (i.e. ICESat) or more. If all 3+ data sets are co-registered to each other, using equation 5.3, the residual remaining after triangulation between the 3+ co-registration vectors is the un-removed linear bias remaining. Of most importance for elevation changes is that of the vertical component.

If co-registration is done properly and with a sufficient data sample, then errors remaining after co-registration are most likely dominated by sensor specific considerations. These might arise from poor acquisition conditions (i.e. white surfaces or clouds for DEMs derived from optical data), erroneous construction of a stereo model (e.g. from poor GCPs), imprecise or insufficient satellite attitude measurements during data acquisition, loss of coherence or errors in the baseline determination in interferometric DEMs, or saturated lidar waveforms for laser scanner DEMs. All these potential error sources will result in bias or voids within the DEMs and dDEMs. The bias is especially problematic for DEM differences as it will directly affect the glaciological interpretations of the quantified surface changes.

5.7 Practical considerations

The generation and public distribution of DEM difference grids introduces a copyright question for the data being used. If one of the DEMs is freely available while another is owned by a national centre and not publically available, the difference grid may be used to back-calculate the non-public DEM. To surpass this issue, filtering and resampling (e.g. block averaging) will be used to generate a lower resolution (ideally 3-4 times) product.

6. Algorithms for Glacier Velocity

6.1 Introduction

A large number of archived and upcoming optical and SAR satellite missions make it now possible to operationally map and monitor glacier flow on a nearly global scale. Deriving glacier displacements globally will provide unique glaciological information (Heid and Kääb, 2011a and b). It will make it possible to compare spatio-temporal variations of glacier velocities both within regions and between regions (e.g. Fig. 6.1). Such knowledge will enable better understanding of a wide range of processes related to glacial mass fluxes, such as glacier response to climate and climatic changes, glacier physics and flow modes, glacier flow instabilities (e.g. surges), subglacial processes (e.g. erosion), supra- and intra-glacial mass transport, etc. Knowledge about glacier ice supply helps to understand the development of glacial lakes and associated hazards (Kääb et al., 2005). Mapping and monitoring glacier flow globally perfectly complements current attempts for mapping and monitoring glacier areas and glacier volume changes on a global scale (GLIMS, GlobGlacier, Glaciers_cci).

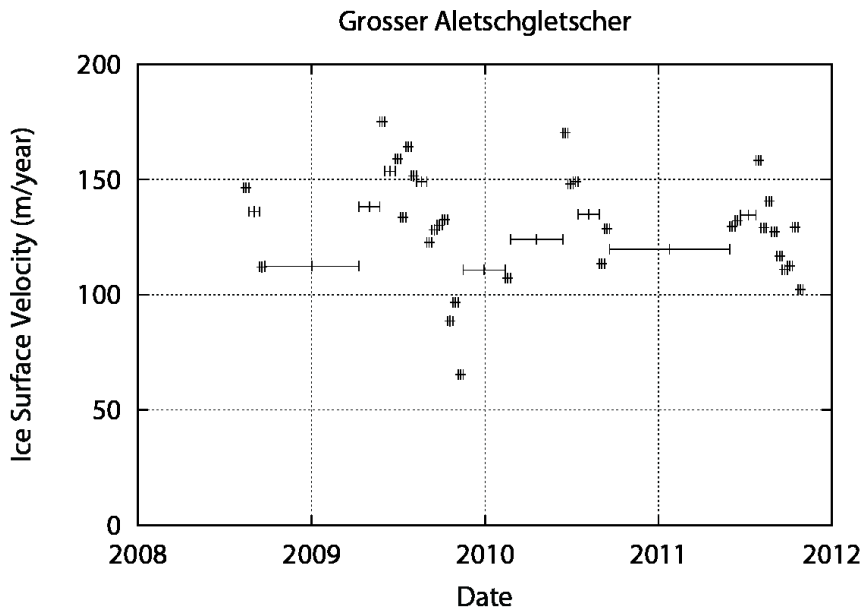

Fig. 6.1: Variations of surface speeds from repeat TerraSAR-X data over Aletschglacier, Swiss Alps.

Within the Glaciers_cci project, the generation of ice motion fields of glaciers is performed using repeat-pass images acquired by SAR and medium to high-resolution optical satellite data. In the case of images from a single look direction none of these methods is capable of directly measuring the full 3-D ice velocity vector which is of interest for ice dynamic studies. Additional assumptions on the ice flow can be introduced to provide ice velocity information directly applicable for glaciological tasks. In general surface-parallel ice flow is assumed, where the slope is derived from a low-pass filtered DEM. As an effect, displacements from SAR and optical methods cannot be compared directly, but only if projected to a common geometry. This step involves assumptions and auxiliary data (in particular DEMs).

This chapter provides an overview on the methods for retrieving ice motion fields from SAR and optical satellite data, including the boundary conditions applied to transform satellite-derived displacement to surface ice velocity products. In response to the User Requirement Document (URD, Glaciers_cci, 2011a) and the surveys conducted in the requirement definition process, the main focus is on raw displacements derived from multi-temporal image pairs in UTM or geographic projection, i.e. without projection to a certain flow direction.

6.1.1 SAR data

SAR data have the advantage of an active sensor that is not affected by solar illumination (day/night) or cloud coverage. Moreover, the acquisition geometry, satellite orbit and the technical sensor properties are well defined and stable, enabling precise analysis of repeat-pass images which are required for retrieval of glacier motion. The penetration depth of microwaves in dry snow and ice is on the order of a few metres to more than 100 m, depending on the radar frequency and snow and ice purity and structure (Ulaby et al., 1982; Maetzler, 1996; Rignot et al., 2001). While radar methods detect a mixture of surface and sub-surface features, they are generally referred to as measurement of glacier surface flow.

Depending on the available SAR data in terms of spatial resolution and temporal sequence of repeat passes, two primary methods evolved during recent years to retrieve the surface ice motion field. The methods discussed here are:

- Across-track Interferometric repeat-pass SAR (InSAR) analysis, delivering the velocity component in radar line-of sight (LOS).
- SAR Image offset tracking: this encompasses various methods, including the cross-correlation of chips in amplitude or complex SAR images and coherence optimization. These methods deliver velocity components in LOS and along-track and do not require phase-unwrapping, but are less sensitive to displacement than InSAR. Depending on the employed algorithm they require distinct features like crevasses or coherence. In their raw form, SAR offset-tracking provides 2-dimensional displacements in SAR geometry, i.e. in the azimuth and slant-range system, and radar interferometry provides 1-dimensional displacements in the line-of-sight (LOS) direction between the ground points and the satellite positions.

6.1.2 Optical data

Surface displacements from repeat optical data are usually performed on orthorectified and projected images so that the displacements are directly in the coordinate system aimed at. The method applied in most cases is block-matching (in contrast to feature matching) where a maximum similarity of an image template is searched for in the second image. The techniques used for that purpose are similar, in parts identical, to the above amplitude offset tracking. A main difference between optical and SAR matching algorithms lies in their ability to cope with the large noise level in SAR images (radar speckle) (Debella-Gilo and Kääb, in press).

A second major difference which is relevant for offset tracking, is the different sensor and thus image geometry. Most optical data used for this purpose are nadir looking, with, for instance, similar pixel resolutions over the image and little effect of elevation changes and errors, whereas both effects play a significant role in the side-looking geometry of SAR data. In their raw form, optical orthoimages provide the 2-dimensional horizontal displacement component in a given map coordinate system. They are sensitive to surface features only.

6.2 Scientific background

The suitable temporal baselines of the repeat data are within two fundamental constraints:

- The displacements have to exceed the accuracy of the method, i.e. have to be statistically significant;
- The surface changes such as melt, deformation, phase coherence loss, etc. over the measurement period have to be small enough so that corresponding intensity or phase features can be matched in both data sets.

Typical temporal baselines suitable for optical data are up to 1-2 years, for SAR offset-tracking up to a few weeks (depending on magnitude of ice flow and stability of available features), for SAR interferometry a few days (see PSD, Glaciers_cci, 2011b).

In the optical domain, tracking methods are usually called '**image matching**', in the microwave domain '**offset tracking**'. Here we use the term offset-tracking for both optical or SAR data.

6.2.1 Ice motion fields from SAR

The general steps of a processing line for ice motion retrieval from repeat-pass SAR data, including InSAR and offset tracking, is outlined in Fig. 6.2. As input a data stack of multi-temporal repeat pass SAR images and a DEM is needed. Accurate co-registration of the repeat pass SAR images is an important step for further analysis and has to be performed with high accuracy. Depending on the software implementation of the co-registration module different steps are applied including geometrical co-registration based on orbit and imaging parameters only, coarse-co-registration with pixel-accuracy using a DEM or not and sub-pixel co-registration using stationary regions or points available in both images. In the latter methods it is important to mask out potentially non-stationary areas like glaciers or water surfaces in the co-registration process. The precisely co-registered SAR image stacks are fed into the InSAR and offset-tracking modules for retrieving ice displacements. These procedures are outlined in more detail in section 6.4. After performing InSAR or offset-tracking the derived displacement component in radar geometry has to be resampled to the preferred map projection and can be converted to ice velocity maps (section 6.4).

6.2.1.1 Ice motion fields using SAR Interferometry

Neglecting random phase noise, which is of relevance for coherence, the interferometric phase measured over a moving glacier by means of satellite-borne repeat pass SAR (SB-SAR) over the time interval Δt is composed of the following contributions:

$$\phi(\Delta t) = \phi(geom) + \phi(topo) + \phi(atm) + \phi(dis) \qquad (6.1)$$

where $\phi(geom)$ and $\phi(topo)$ are the phase shifts related to the observation geometry for flat Earth and topography, respectively, $\phi(atm)$ is the phase shift caused by changes in the atmospheric propagation conditions (it mainly depends on differences of atmospheric water vapour content between the two images acquisitions of an interferogram, and for lower frequencies also on ionospheric conditions). The parameter $\phi(dis)$ is the phase shift due to displacement in line-of-sight (LOS) of the radar beam over the time interval Δt. Both $\phi(geom)$ and $\phi(topo)$ depend on the distance (baseline) of the SAR positions from which the two images are acquired.

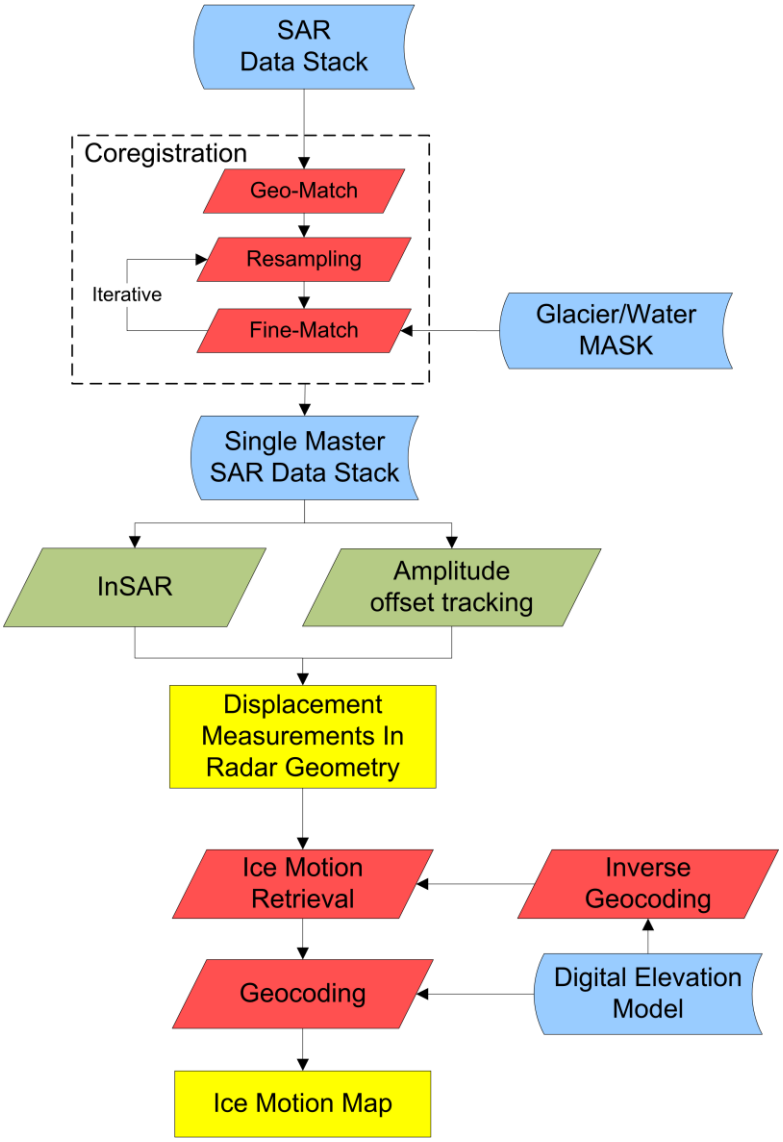

Fig. 6.2: Overview of general steps for ice motion retrieval from SAR data. SAR Interferometry and amplitude offset-tracking using SAR data. The InSAR module is shown in more detail in Fig 6.3, the Amplitude offset-tracking in Fig. 6.4

For satellite-borne repeat pass InSAR the positions of the two satellites at the time of image acquisition need to be known very accurately to calculate ϕ(geom). Furthermore, a very precise estimation of ϕ(topo) based on an accurate DEM is crucial for the accuracy of the InSAR results. The InSAR sensitivity to ϕ(geom) and ϕ(topo) decreases with decreasing perpendicular baseline (B_n), and becomes zero if $B_n = 0$.

If two separate interferograms are available, ϕ(topo) can be obtained directly from the InSAR data by means of differential processing. However, this requires that the surface velocity is the same in the two interferograms which is often not fulfilled on glaciers.

There is another phase component that is not explicitly included in Eq. 6.1, namely the phase change due to temporal change of the propagation path within the observed medium (e.g. due to accumulation of dry snow). This can in principle be treated the same way as ϕ(atm), assuming similar snow accumulation as on the reference targets, and can hardly be separated from the atmospheric contribution without external information. However, snow fall on glaciers usually results in rapid temporal decorrelation (i.e. hampering InSAR processing), so that this phase contribution is not taken into account separately.

Figure 6.3 summarizes the main processing scheme of a typical InSAR sequence for ice velocity retrieval. It starts with the definition of the area-of-interest (AOI) and the window-size for low pass filtering by means of block-averaging (multi-looking). As a next step, the coherence is calculated in order to identify areas with sufficient stability of the signal between the two SAR acquisitions. The next step of the InSAR processing line forms the interferogram by multiplying one SAR image with the complex conjugate of the other precisely co-registered SAR image. The ice displacement ΔR in LOS between the time t_1 and t_2 can be written as:

$$\phi_{t_2} - \phi_{t_1} = \frac{4\pi}{\lambda}\Delta R = \frac{\phi_{dis}}{t_2 - t_1} \tag{6.2}$$

λ is the SAR sensor wavelength, ΔR is the LOS displacement and $\phi_{t_2} - \phi_{t_1}$ is the measured phase difference. As the InSAR approach relies on a phase measurement, the path difference can be determined at the precision of the fraction of the SAR wavelength λ. In the case of steep incidence angles the displacement phase is in general more sensitive to vertical displacement than to horizontal displacement. Although the main contribution to the motion related phase comes from horizontal motion components, some part of the phase contribution on the glacier terminus should be attributed to vertical displacement.

In order to calculate the LOS displacement term ΔR and subsequently the ice motion, the motion-related phase has to be unwrapped. Regions with in-sufficient coherence are excluded from the unwrapping process. The output of the procedure is a map of displacements in line of sight direction. The conversion and assumptions necessary for retrieving a reasonable ice velocity map from LOS displacements are described in section 6.2.1.4.

6.2.1.2 Factors affecting interferometric coherence of glacier surfaces

Phase decorrelation is the main limiting factor for InSAR repeat pass applications over snow and ice. The degree of coherence is used to estimate the stability of the phase relation between two SAR images used for forming an interferogram. The coherence magnitude $|\gamma|$ is estimated over a window containing N pixels:

$$|\gamma| = \frac{\left|\sum_{n=1}^{N} y_1^{(n)} y_2^{*(n)}\right|}{\sqrt{\sum_{n=1}^{N}\left|y_1^{(n)}\right|^2 \sum_{n=1}^{N}\left|y_2^{(n)}\right|^2}} \tag{6.3}$$

where $0 \le |\gamma| \le 1$. For a reliable estimate of $|\gamma|$ the window should include > ~ 50 pixels. The total degree of coherence can be split up in several factors (Zebker and Villasenor, 1992):

$|\gamma|$ = γ(SNR) γ(processor) γ(spectral) γ(path) γ(temporal))

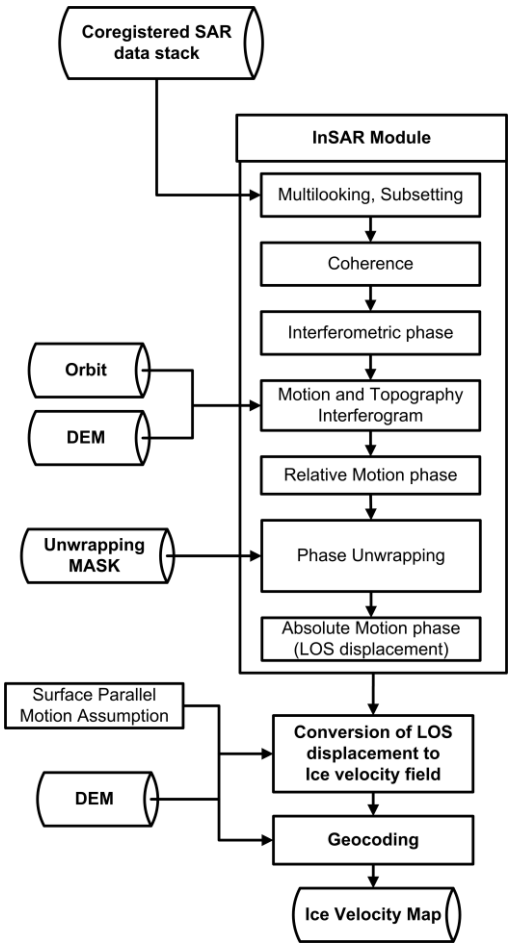

Fig. 6.3: Flow chart of the InSAR module which is part of the Glaciers_cci ice motion analysis framework.

The various contributions are due to the following effects:

- γ(SNR) is related to the signal-to-noise ratio of the data. It becomes increasingly important as the backscattering coefficient approaches the noise equivalent σ°. The following numbers demonstrate the impact of SNR on phase noise: SNR = 10 dB results in standard deviation of phase $\sigma\phi = 0.65$ rad, SNR = 5 dB in $\sigma\phi = 0.95$ rad.
- γ(processor) is related to phase errors of the sensor and processor. These are usually quite small.
- γ(spectral) is related to the spectral shift of the signal due to different sizes of the corresponding image resolution cells, resulting from different observation geometries for the two scenes according to the different satellite positions. This decorrelation is composed of a surface contribution and (in case of a volume scattering medium such as dry snow) from a volume scattering contribution (Hoen and Zebker, 2000). For ERS-SAR, the critical baseline, where the two images are completely decorrelated, is 1100 m. For InSAR motion analysis image pairs with short baselines (e.g. 100 m for ERS-1/2 SAR data) are preferred, in order to minimize this so-called "baseline decorrelation".

- γ(path) is related to differences in the propagation conditions along the path of the radar beam at pixel scale. This is usually not relevant for coherence, because the phase disturbances at pixel scale are very small, as obvious from the spectrum of atmospheric phase shifts (Hannsen, 2001).
- γ(temporal) is the main factor for decorrelation of repeat pass InSAR data over snow and ice, as well as over many other natural targets.

Because the phase variations can be considered as being statistically independent, multi-looking is an efficient way for reducing the phase variance. For a given degree of coherence $|\gamma|$ and number of looks N_L, the phase variance can be calculated by:

$$\sigma_\phi^2 = \frac{1-\gamma^2}{2\gamma^2 N_L} \quad [\text{rad}^2] \tag{6.4}$$

The temporal decorrelation, γ(temporal), of radar signals over glaciers results from changes of the backscattering phase and amplitude and can be attributed to:

- Surface melt
- Snowfall
- Snow drift (wind erosion and deposition)
- Surface rotation (e.g. in shear zones)
- Deformation at sub-pixel scale

Surface melt of snow and ice often results in complete decorrelation at C-band even within one day (e.g. Rott and Siegel, 1997; Strozzi *et al.*, 1999). In L-band the coherence of melting snow and ice is better preserved, as the comparison of one-day X-, C-, and L-band repeat pass data of SIR-C/X-SAR has shown (Rott *et al.*, 1998; Stuefer, 1999). In the case of debris-covered glaciers the coherence might be preserved over longer time periods.

Snowfall and snow redistribution by wind (snow drift) in the time interval between the image acquisitions may also cause significant decorrelation at C-band within a few days, as shown with ERS SAR one-day tandem data of Alpine test sites (Rott and Siegel, 1997) and three-day repeat pass data of Alaska (Li and Sturm, 2002). Surface rotation of a target in respect to the radar look direction, as for example observed in shear zones along glacier margins or at boundaries of ice streams, is a geometrical factor causing decorrelation because it results in a spectral shift (Zebker and Villasenor, 1992). If the target is not deformed at sub-pixel scale, complete decorrelation results for C-band with ERS chirp bandwidth (15.5 MHz) for a rotation ≥ 0.7°. At L-band this is relaxed by a factor of four.

Deformation at sub-pixel scale takes place in heavily crevassed shear zones, as found at fronts of fast-flowing calving glaciers (Rott *et al.*, 1998). As for surface rotation, increase of chirp bandwidth helps to reduce these effects. Because of rapid decorrelation, most InSAR studies of glacier motion have been based on one-day repeat pass data of the ERS-1/ERS-2 tandem phase and on 3-day repeat pass data of the ERS-1 ice phase. Only over cold ice masses, where ice motion is slow and accumulation is small, coherence may be preserved over periods of several weeks, as demonstrated for ice motion analysis on the Antarctic plateau with 24-day cycle (Radarsat) and 35-day cycle (ERS) repeat pass data (Kwok *et al.*, 2000). Envisat ASAR

and ALOS PALSAR have 35 and 46 day repeat cycles, respectively, so that their use for interferometric analysis over temperate glaciers is not feasible.

6.2.1.3 Incoherent amplitude offset tracking

Tracking is employed in order to provide ice surface motion when the signal in the repeat-pass SAR image pair is not coherent. A general flow diagram of the processing is shown in Fig. 6.4. After the common co-registration, outlined in Fig. 6.2, the displacement is measured by applying various algorithms. One of the most commonly used is the normalized cross correlation coefficient (NCC) of amplitude image chips according to Barnea et al. (1972):

$$NCC(u,v) = \frac{\sum_{x,y}[f(x,y)-\overline{f}_{u,v}][t(x-u,y-v)-\bar{t}]}{\sqrt{\sum_{x,y}[f(x,y)-\overline{f}_{u,v}]^2 \sum_{x,y}[t(x-u,y-v)-\bar{t}]^2}} \tag{6.5}$$

f is the master image, t is the template window with pixel position at (u, v) and (x, y) is the pixel position in the reference image. $\bar{t}$ and $\overline{f}_{u,v}$ are the mean amplitude values of the template and master window, respectively. The NCC is calculated on a regular slant-range grid of typically 64 (range) x 64 (azimuth) pixels.

Depending on the implementation there might be some overlap between the search and reference windows implicitly resulting in some low-pass filtering as the image windows are not completely independent. The NCC kernel provides image offsets in range (LOS) and azimuth (along-track) direction. Optionally the Correlation Relaxation Labelling (CRL) technique can be applied to check for outliers in the displacement field. CRL provides the opportunity to check the consistency of a NCC image offset retrieval by comparing the results to neighbouring NCC results (Wu, 1995). If the result is not consistent with the neighbourhood it will be rejected. In general, the best performance of the NCC kernel can be expected in regions with pronounced surface features such as crevasses, drainage channels and surface moraines, but it also works where speckle (and thus coherence) is retained.

In comparison to SAR interferometry, offset-tracking techniques have various drawbacks. Comparatively large image patches (> 64 x 64 pixels) are needed to retrieve a single motion vector, which excludes the application ERS SAR or ASAR on small glaciers. Distinct features (including speckle) need to be present on the glacier surface that move with the glacier and are preserved over months or years and in accumulation areas such features are usually missing. The offset-tracking techniques are significantly less sensitive to displacement than InSAR which results in larger error bars. However, this improves with the new high resolution spaceborne SAR systems such as TerraSAR-X and Cosmo-Skymed.

Alternatively to the NCC parameter for determination of the displacement other statistical parameters can be applied (see section 6.4.2), including a complex-correlation of SAR images and coherence optimization. The computional burden and performance of these algorithms are different to those of the NCC, but the above mentioned characteristics remain valid. In section 6.4.2 we review these algorithms in more detail.

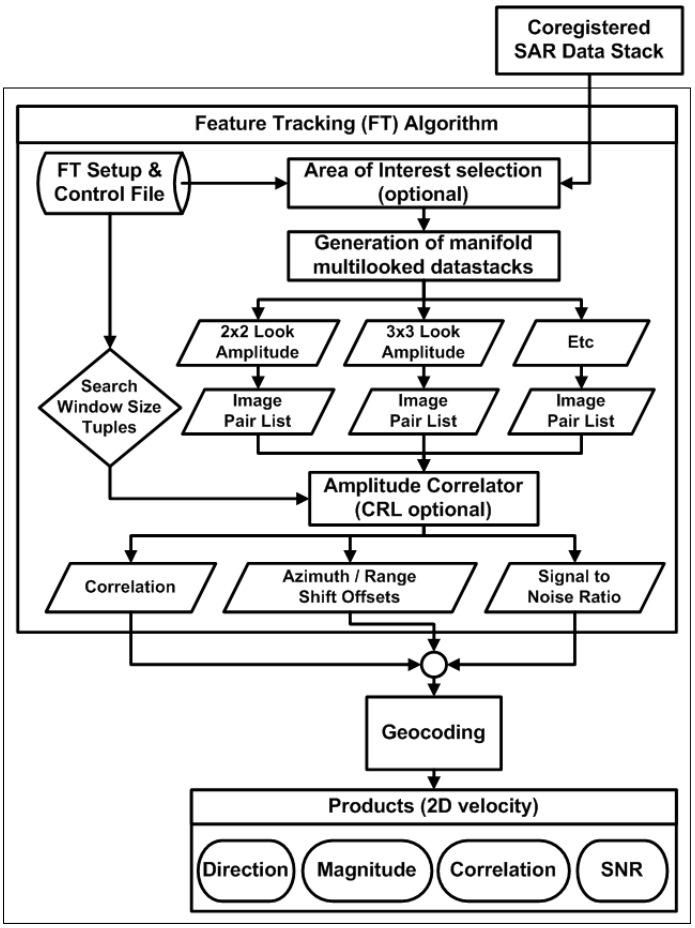

Fig. 6.4: Flow diagram outlining the principal processing steps of SAR offset tracking.

6.2.1.4 Retrieval of glacier surface velocity by SAR

The displacement of a particle on the glacier surface during a time interval, T, is described by the three-dimensional displacement vector $\mathbf{d}$:

$$\mathbf{d} = d_x\hat{\mathbf{x}} + d_y\hat{\mathbf{y}} + d_z\hat{\mathbf{z}} = \mathbf{d_h} + d_z \tag{6.6}$$

Normalizing the displacement by the time interval, T, between the two image acquisitions the velocity vector $\mathbf{v}$, is given by:

$$\mathbf{v} = v_x\hat{\mathbf{x}} + v_y\hat{\mathbf{y}} + v_z\hat{\mathbf{z}} = \mathbf{v_h} + v_z \tag{6.7}$$

$\hat{\mathbf{x}}$, $\hat{\mathbf{y}}$, and $\hat{\mathbf{z}}$ are the unit vectors in the Cartesian coordinate system. The orientation of the coordinate system can, for example, be selected according to a specified map projection. In the following the x-coordinate is assumed to correspond to easting (E), the y-coordinate to northing (N), and the z-coordinate upward perpendicular to the local geoid surface. The three components of the vector can be re-arranged to separate the vertical displacement component d_z and the horizontal displacement vector d_h. The vertical displacement (elevation change) at the glacier surface represents the net effect between the ablation/accumulation and emergence/submergence velocity of the ice at a given location. On land terminating glaciers in retreat, the emergence velocity in the ablation area is usually rather small. During summer the ablation dominates over emergence as well as on glaciers that are in balance over the year,

causing the surface to subside. Mass balance assessments of glaciers and ice sheets by flux divergence calculations require at least the two-dimensional horizontal surface velocity pattern (Mohr and Madsen, 1996). The knowledge of the full 3D flow pattern is required for some ice dynamical studies and the validation of ice flow models, whereas other approaches are able to account for single velocity components.

Figure 6.5 shows the imaging geometry of SAR and the velocity / displacement components. Repeat pass SAR enables two main methods for mapping ice displacement, Differential SAR Interferometry (DINSAR) and incoherent amplitude offset tracking. DInSAR measures only the displacement in radar look direction (LOS) during the time interval between the acquisitions of two SAR images. However, surface deformations may occur in vertical or horizontal direction, along the surface gradient, in the local surface plane, but also in any other directions. Strictly speaking, a single SAR interferometric observation does not allow to full determination of the magnitude and direction of a surface deformation, but only allows an observation of the deformation component along the radar look direction.

As the vertical component affects the slant range displacement, two cases can be distinguished depending on the imaging geometry relative to the flow direction of the glacier.

- *horizontal displacement towards near range and downward vertical displacement*: without taking the vertical component into account, the observed pixel shift in slant range direction derived from offset-tracking is reduced relative to the "true" horizontal displacement
- *horizontal displacement towards far range and downwards vertical displacement:* without taking the vertical component into account, the observed pixel shift in slant range direction derived from offset-tracking leads to an overestimation of the horizontal displacement relative to the "true" horizontal displacement

In the interpretation of ice displacement fields of glaciers with changing ice flow direction the discrimination of the two cases is particularly important.

For the description of a displacement in look direction (line-of-sight) we select the polar coordinates in the geocoded (map) geometry. We characterize the displacement vector in look direction $\boldsymbol{v} = (v_x, v_y, v_z)$ by its magnitude d, elevation angle υ and orientation angle φ:

$$\begin{aligned} v_x &= d \cdot \cos\upsilon \cdot \sin \\ v_y &= r \cos\varphi \\ v_z &= r \cdot \sin\upsilon \end{aligned} \tag{6.8}$$

For a displacement component $\boldsymbol{v}$ in look direction, the possible displacement vectors are in a plane perpendicular to the look vector direction intercepting the look vector at a distance r. The equation of a plane perpendicular to a vector $\boldsymbol{v} = (v_x, v_y, v_z)$ is given by:

$$v_x x + v_y y + v_z z = r^2 \tag{6.9}$$

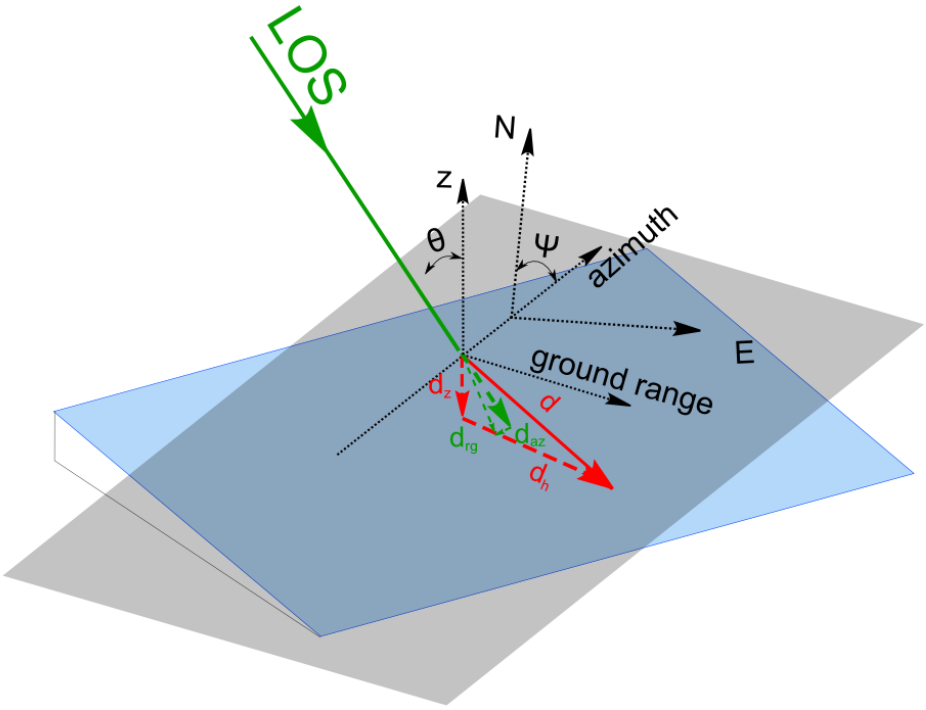

Fig. 6.5: Sketch of the geometry of spaceborne SAR observations with 3D displacement vector (d). With d_h: the horizontal displacement component, d_z: the vertical displacement (elevation change), d_{az} and d_{rg}: are the displacement components in azimuth and range direction in SAR slant range coordinates, respectively, θ: the off-nadir angle, and ψ the azimuth angle (defined as the angle between North and along-track direction).

where x, y and z are the Cartesian coordinates of the 3-dimensional displacement vector, with the x coordinate corresponding to the east direction, the y coordinate to the north direction and the z coordinate pointing upward.

The relationship between the Cartesian (x,y,z) and polar coordinates (r,υ,φ) is given by (DMK/DPK, 1977):

$$r=\sqrt{x^2+y^2+z^2}$$
$$\sin\upsilon=\frac{z}{r} \qquad (6.10)$$
$$\cos\varphi=\frac{x}{r\cos\upsilon},\ \sin\varphi=\frac{y}{r\cos\upsilon}$$

If only one measurement from one look direction is available, the 3-dimensional displacement vector can be only computed if a displacement or "flow" direction is known. We represent this flow direction by the unity vector $\boldsymbol{f} = (f_x,f_y,f_z)$ defined by its elevation (slope) angle υ_f and its orientation angle φ_f:

$$f_x=\cos\upsilon_f\cdot\sin\varphi_f$$
$$f_y=\cos\upsilon_f\cdot\cos\varphi_f \qquad (6.11)$$
$$f_z=\sin\upsilon_f$$

Displacement in the flow direction of ***f*** means that the displacement is on the straight line defined by the equations:

$$x = c \cdot f_x$$
$$y = c \cdot f_y \qquad (6.12)$$
$$z = c \cdot f_z$$

In this case the system of equations to solve for the displacement vector is given by equation (6.12) (in the case of a measurement from a descending track). The system can only be solved if flow and look directions are not perpendicular to each other, because in this case the SAR measurement is not sensitive to the displacement. The magnitude r of the 3-dimensional displacement vector can be computed by:

$$r = \frac{r_d}{\sin(\theta_d)\cos(\varphi_d)\cos(\varphi_d)+\cos(\theta_d)\sin(\varphi_d)} \qquad (6.13)$$

where r_d is the magnitude of the displacement in the look direction of the SAR and θ_d = (90°-υ_d) and φ_d are the incidence and orientation angles, respectively, of the SAR observation.

SAR data are often acquired in two independent look directions, those of ascending and descending tracks. In this case, only one additional restriction of the deformation geometry is required. Typical restrictions are displacement in horizontal direction or along the surface plane. For the 3-dimensional interpretation of measurements of ascending and descending tracks, it is suitable to first characterize the two available displacement components and then to combine them with an assumption about a third direction.

In order to obtain a 3-dimensional deformation vector field, observations from three different look directions are required. However, SAR data are only acquired in two independent look directions, those of ascending and descending tracks. As a consequence, an additional restriction of the deformation geometry is needed. In many cases the knowledge of the deformation process allows to find such a geometric restriction. Typical restrictions are displacement in vertical or horizontal direction or along the surface plane. For the 3-dimensional interpretation of measurements of ascending and descending tracks, it is suitable to first characterize the two available displacement components and then to combine them with an assumption about a third direction.
Displacement components r_a measured in the look-direction of SAR data acquired in ascending mode (elevation angle υ_a and orientation angle φ_a) and r_d measured in the look-direction of SAR data acquired in descending mode (elevation angle υ_d and its orientation angle φ_d) result in plane equations:

$$a_x x + a_y y + a_z z = r_a^2 \qquad (6.14)$$

where the x, y, and z components of the vector **a** = (a_x,a_y,a_z) are:

$$a_x = r_a \cdot \cos(\upsilon_a)\sin(\varphi_a)$$
e (6.15)
$$a_z = r_a \cdot \sin(\upsilon_a)$$

and

$$d_x d_y + d_z^2 = r_d^2 \tag{6.16}$$

where the x, y, and z components of the vector $\mathbf{d} = (d_x, d_y, d_z)$ are:

$$\begin{aligned} d_x &= r_d \cos\varphi_d \sin\alpha_d \\ d_y &= r_d \cos\varphi_d \cos\alpha_d \\ d_z &= r_d \cdot \sin\upsilon_d \end{aligned} \tag{6.17}$$

Typical elevation angles of SAR data are between 70º and 50º (in this context the displacement vector in look direction points upwards). If we can assume that there is no vertical component of the motion

$$z = 0 \tag{6.18}$$

Equations (6.14) and (6.16) form a system of two equations which can be solved for the two unknowns x and y representing the east and north coordinates of the displacement vector. The assumption of displacement along the surface normal can be useful in glaciology when flow is nearly parallel to the surface of the glacier. The unity surface normal vector $\boldsymbol{n}$ (i.e. perpendicular to the surface) is computed from a DEM and can be expressed with its orientation and elevation angles υ_n and φ_n, respectively, as:

$$\begin{aligned} n_x &= \cos\upsilon_n \cdot \sin\varphi_n \\ n_y &= \cos\upsilon_n \cdot \cos\varphi_n \\ n_z &= \sin\upsilon_n \end{aligned} \tag{6.19}$$

Displacement along the surface plane means that the displacement is on a plane perpendicular to $\boldsymbol{n}$

$$n_x d_x + n_y d_y + n_z d_z = 0 \tag{6.20}$$

Equations (6.14), (6.16) and (6.17) are a system of three equations for the three unknown x, y and z representing the Cartesian coordinates of the displacement vector.

SAR offset-tracking provides the shift of features in slant range and azimuth (across track) direction. As for InSAR, using data of ascending and descending orbits, an additional restriction about the deformation geometry is required The displacement vector in slant range, $\boldsymbol{r}_g$, and azimuth direction, $\boldsymbol{d}_{az}$, observed at a pixel, is related to the 3D displacement on the Earth surface according to

$$\begin{aligned} v_x &= |\mathbf{r}_{LOS}| \sin\upsilon \cos\varphi + |\mathbf{r}_{az}| \sin\varphi \\ v_y &= |\mathbf{r}_{LOS}| \sin\upsilon \sin\varphi + |\mathbf{r}_{az}| \cos\varphi \\ v_z &= |\mathbf{r}_{LOS}| \cos\upsilon \end{aligned} \tag{6.21}$$

The azimuth shift observed by offset-tracking is not sensitive to the vertical component of the displacement that is observed in the ablation zone of glaciers with significant ice melt (causing a net-decrease of surface elevation) and can thus be converted directly into horizontal motion. The slant range shift observed by offset-tracking includes both the horizontal and vertical motion, which cannot be resolved without additional information.

6.2.2 Surface displacements from repeat optical data

Surface displacements from optical data are derived by finding similarities between two (or more) images similar to the above SAR amplitude offset tracking. A general flow chart for the processing is shown in Fig. 6.6. Even if in some cases feature-based methods can provide good results, block-matching techniques are preferred due to typical glacier surfaces that often lack distinct geometric features such as crevasses, but rather contain less sharp radiometric features, e.g. from dust or debris deposits. The relevant offset-tracking algorithms are listed under section 6.4. The main difference between the design of offset-tracking algorithms for SAR amplitude images and optical images are the higher robustness against noise (radar speckle) that SAR offset-tracking algorithms need to have. Thus, the same principles may be used for both types of images, but with different parameterisations (e.g. template size), and different evaluation criteria for their performance.

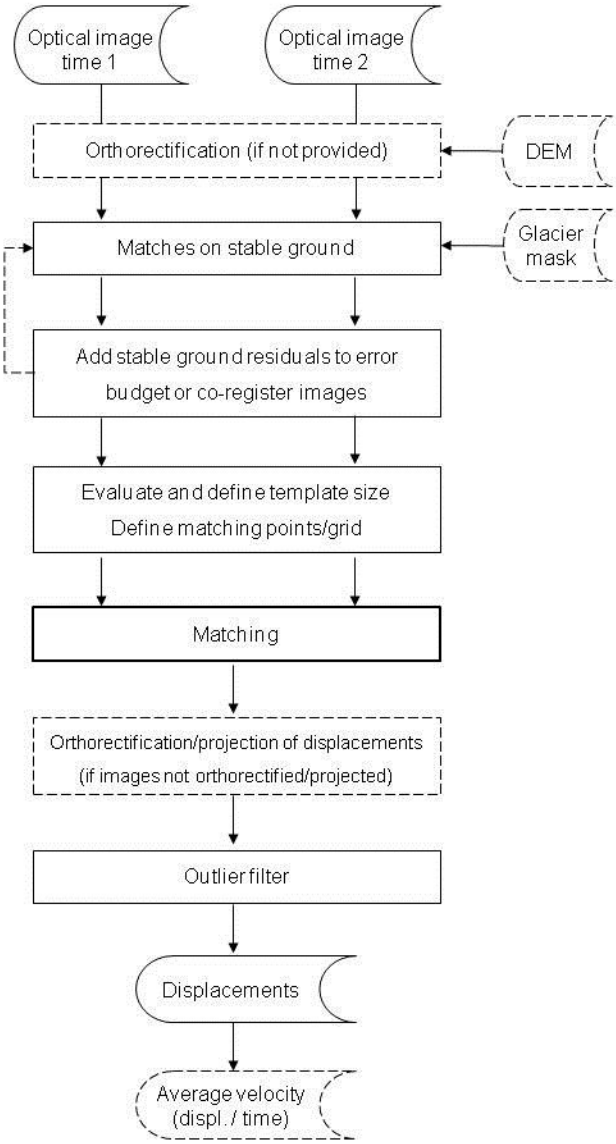

Fig. 6.6: Flow chart for glacier velocity from repeat optical images.

Usually, orthorectified optical data will be matched so that the raw displacements are already in the desired projection. A proper orthorectification is therefore crucial to the positional accuracy of the matches. The main error influences to orthoprojection are errors in the sensor position and attitude information (either in the data auxiliary data or from orientation based on ground control points) and propagated elevation errors from the DEM used for orthoprojection. Offsets on stable ground allow defininition of the level of propagated DEM errors, and for evaluation and partial correction of orientation errors. Though, it is crucial to keep in mind that these errors, in particular the propagated DEM errors, cannot be simply corrected by coregistration because the misregistrations are not linear (also not linear in the sense of a higher order polynomial). Rather, stable ground offsets give the background error to be expected from the matches on the moving glacier and to be added to the total error budget.

Since displacements are usually tracked from orthoprojected images, the tracked positions can be defined as a raster in e.g. UTM or geographic coordinates, or as points of special interest, for instance positions of ground measurements, such as GNSS, or fixed positions or flux gates for time series analysis.

The matching template sizes can be chosen after iterative tests on the images, or from a list of typically optimal sizes for specific image types and resolutions. An automatic choice is in principle possible, but very time consuming and only particularly effective for high-resolution data, less for medium resolution such as Landsat (Debella-Gilo and Kääb, in press).

The matching itself is to find in image of time 2 the most similar location to a template of image of time 1 (Fig. 6.7). The available algorithms differ among others in the similarity measure and the normalisation used.

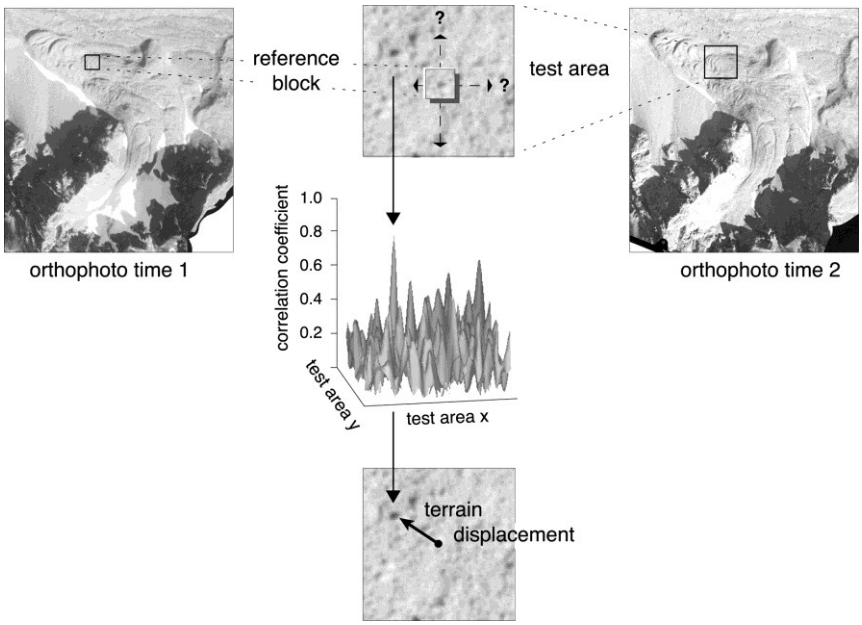

Fig. 6.7: Principle of matching between two repeat optical orthoimages within the offset-tracking process.

In the case the input images have not been orthorectified beforehand, the tracked displacements would have to be projected/orthorectified. This step requires reconstruction of the acquisition geometry and in most cases heavy operator interaction and specialized processing software. Glaciers_cci will therefore not work with un-orthorectified optical images before the offset tracking process.
The displacements can be filtered for outliers, and average velocities be computed over the observation time period. The final displacements/velocities are horizontal movement components in the projection chosen for the orthoimages. This projection can be easily changed in standard software as the displacements are point information with attributes.

6.2.3 Evaluation criteria

The purpose of this chapter is not to review algorithms themselves on the strictly technical level, but to compare algorithms and their potential embedding in a processing system with **global scale applications** as a focus. As a result of this focus, the main evaluation criteria for the assessment of glacier offset-tracking methods are:

- Robustness of the method under different surface conditions (e.g. illumination, reflectance levels);
- Robustness of the method under different sensor resolutions (high and medium resolution);
- Robustness of the method under different imaging frequencies (optical: visible to infrared; SAR: X – L band; but not necessary the same algorithm for optical and SAR intensity data);
- Suitability of the method for a high degree of automation;
- Accuracy requirements as outlined in the PSD (Glaciers_cci, 2011b).
- User requirements as outlined in the URD (Glaciers_cci, 2011a).

In summary, the focus is on algorithms for highly automated and robust global-scale application based on varying sensors. Among others, the focus is not on advanced filtering algorithms for displacements or projections to different three-dimensional movement components, as the users prefer raw displacements in UTM or geographic projection.

6.3 Input data

The above criteria limit the type of satellite input data to be considered to those that are globally available, provide regular acquisitions, and have no or uncomplicated restrictions. As a consequence, the following data are considered for **production** of glacier displacements:

- Optical: Landsat (15-30m res.), ASTER (15 m res.), Sentinel-2 (planned); Landsat data are orthorectified; ASTER data can be ordered with and without orthorectification. The data have different co-registration accuracies in the subpixel level, i.e. pixel geolocation accuracies that can be estimated by stable ground matches, and have to be added to the error budget.
- SAR: ERS-1/2, Envisat ASAR, ALOS PALSAR, TerraSAR-X, CosmoSkymed, Sentinel-1 (planned).

For product and algorithm **validation** the following sensors are considered, due to low spatial and temporal availability, small coverage, usage restrictions, etc.:

- Optical: ALOS AVNIR and PRISM, SPOT, commercial high-resolution; some of these data are (only) available as orthoprojected versions, some not.

- SAR: JERS-1, TerraSAR-X, Radarsat strip and image mode, Cosmo-Skymed.

Radar interferometry requires expert user interaction, in particular in the phase unwrapping step, and acquisitions with daily time intervals, which are currently not globally available. Though it is an invaluable method for specific studies and for complementing and validating tracking results, it is not suitable for current and near future robust, highly automated and global-scale glacier displacement measurements.

6.4 Review of algorithms and methods

6.4.1. Pre-processing

6.4.1.1 Geometric pre-processing

The most crucial pre-processing step before InSAR and offset-tracking is the accurate co-registration of the data to be matched. Offsets over stable ground measured using the same algorithms as evaluated below (though often with different parameterizations) form the base of co-registration. The search (=slave) image(s) can be either transformed to the geometry of the reference (=master) image or (e.g. polynomial) transformation parameters can be computed and applied to the matching results without transforming the images. Co-registration transformation has the advantage to make offset-tracking and other usages of the images (e.g. time-series analysis of SAR data) easier, but increases the computational time and storage and may introduce loss of information, even if this is marginal for SAR data.

A polynomial transformation from a working image with coordinates (u,v) to the reference image (x,y) is given by:

$$u = \sum_{l=0}^{m} \sum_{j=0}^{i} a_{lj} x^{l} y^{j-1}$$
$$v = \sum_{l=0}^{m} \sum_{j=0}^{i} b_{lj} x^{l} y^{j-1} \qquad (6.22)$$

Where a and b are the polynomial parameters, and m and i the order of the polynomial used, in image registration typically up to 5th order.

Note that (polynomial, and other) coregistration is not appropriate when tracking offsets in orthorectified images (see 6.2.2), but only when images in sensor geometry or in ellipsoid projected format are used.

6.4.1.2 Radiometric pre-processing

A number of radiometric pre-processing steps in offset-tracking have been proposed such as:

i. Normalizations of the images (Heid and Kääb, 2011);
ii. Tracking based on derivatives of the image data rather than the raw data (e.g. filtered versions, gradient images) (Heid and Kääb, 2011);
iii. Interest operators to select suitable tracking targets (Förstner, 2000; Debella-Gilo and Kääb, in press);
iv. Selection of most suitable band or radar frequency, if available, or derivatives of multiple bands (e.g. principle components).

Some of these pre-processing possibilities can only be applied to very specific input data (iv) and do not meet the above evaluation criteria. Other potential pre-processing procedures (i, ii) are actually built-in in some tracking algorithms. Further procedures (ii, iii) depend much on the data resolution and noise level, and thus also do not meet the evaluation criteria. As a consequence only radiometric pre-processing procedures that are largely independent of input data are considered. Since their applicability depends much on the tracking algorithm, they are considered together with these algorithms in the next section.

6.4.2 Algorithms for glacier velocity

We list and assess the most commonly used algorithms (and modifications of them), based on literature and own tests, and in view of the above criteria. Apart from InSAR, all below algorithms are block matching algorithms relying on grey value matrices. Feature-based algorithms are not considered, because they depend on image resolution and distinct features (though certainly with good performance over feature-rich zones such as crevasses), whereas many glaciers and glacier sections are characterised by the lack of such distinct features.

Abbreviation	InSAR
Algorithm	SAR Interferometry $$\phi_2 - \phi_1 = \frac{4\pi}{\lambda}\Delta R = \frac{\phi_R}{t_2 - t_1}$$ where t_1 and t_2 indicate the time of the two SAR acquisitions and ΔR is the difference in distance from the scatterer on the ground to the two positions in space.
Reference	Bamler and Hartl (1998), Rosen et al. (2000)
Applications	Various.
Description	SAR interferometry is based on the computation of the phase difference between two acquisitions, which is directly related to displacement along the line-of-sight.
Advantages	- High precision (sub-centimetric; fraction of a wavelength). - Widely used.
Disadvantages	- Requires short time intervals (days) to retain coherence. - Requires accurate DEM or two consecutive pairs to remove the topographic component of the interferomtric phase.
Comments	- Considering that all current and future planned global SAR missions have repeat cycles of several days that preclude high coherence for large glacierized areas, InSAR will in the frame of this project likely be considered for validation only.

Abbreviation	NCC
Algorithm	Normalized cross-correlation in spatial domain $$\mathrm{CC}(i,j) = \frac{\sum_{k,l}(s(i+k,j+l)-\mu_s)(r(k,l)-\mu_r)}{\sqrt{\sum_{k,l}(s(i+k,j+l)-\mu_s)^2 \sum_{k,l}(r(k,l)-\mu_r)^2}}$$ where (i,j) indicates the position in the search area, (k,l) the position in the reference area, r the pixel value of the reference chip, s the pixel value of the search chip, μ_r the average pixel value of the reference chip and μ_s the average pixel value of the search chip.

Reference	Kääb and Vollmer (2002), Heid and Kääb (2011)
Applications	Kääb (2005)
Description	NCC is a matching method that is often used when studying glacier velocities. This is mostly due to its simplicity and robustness. The first image is taken as the reference image, and a template out of this image is searched for in the second image, or the search image. The peak of the cross-correlation surface indicates the displacement between the images. This cross-correlation is normalized.
Advantages	- The algorithm is simple and robust. - The algorithm can be applied to optical and SAR data. - Effects of normalization: Firstly, images with different illumination conditions can be better compared, and secondly, the correlation coefficient from different correlation attempts can be compared.
Disadvantages	- Original precision is only on the pixel-level. - Because this method operates in the spatial domain (as a convolution operation), the computation is time-consuming compared to computations in the frequency domain. - The NCC method is easily dominated by large differences in the digital numbers. If large differences exist within the reference or the search template, large differences also have to exist in the opposite window (i.e. the search or the reference template, respectively). We hypothesize that this is a major drawback with this method for glacier applications using optical data. Glacier areas usually contain large differences in digital numbers, because white snow and black rocks etc. are present. This would not be a problem if these differences were present in both images and also represented the displacement. However, it is common that snow patches in one image disappears in the nest image, or that rocks move independently of the glacier movement by rolling or sliding at the glacier surface. Situations where large intensity differences are not present in both images or where large intensity differences do not represent the displacement are hence hypothesized to create erroneous matches for the NCC method.
Improvements	- The original pixel-level precision of NCC can be improved by interpolation of the correlation peak or image template interpolation beforehand correlation (Debella-Gilo and Kääb, in press). - An ice mask can be applied to exclude ice-free regions and therefore improve the computational efficiency. - If available (e.g. from previous studies or runs), a prediction of the glacier motion can be applied to better match the offsets.

Abbreviation	CCF
Algorithm	Normalized cross-correlation in frequency domain $$CC(i,j) = IFFT\,(F(u,v)G^{*}(u,v))$$ where F(u,v) is the Fast Fourier Transform (FFT) of the matching window from the image at time t = 1, G(u,v) is the FFT of the matching window from the image at time t = 2, * denotes the complex conjugated and IFFT is the Inverse Fast Fourier Transform.
Reference	Scambos et al. (1992), Heid and Kääb (2011)

Applications	Skvarca et al. (2003); Rott et al. (2010)
Description	Cross-correlation can also be computed in the frequency domain by multiplying the Fourier transform of one image and the complex conjugated Fourier transform of the second image (the convolution theorem). This procedure is equivalent to computing the cross-correlation in the spatial domain.
Advantages	- Faster than NCC because operated in the Fourier domain
Disadvantages	- The NCC normalization cannot easily be transformed to the frequency domain. In the CCF method, only the cross-correlation is computed, so that this method does not normalize. This implies that different illumination conditions in the two images can lead to mismatches. Also, the method can result in a wrong match if the illumination varies within the section to be matched.
Improvements	not yet known

Abbreviation	PC
Algorithm	Phase-correlation in frequency domain $$CC(i,j) = IFFT\left(\frac{F_o(u,v)G_o^*(u,v)}{\left\lvert F_o(u,v)G_o^*(u,v)\right\rvert}\right)$$ where F(u,v) is the Fast Fourier Transform (FFT) of the matching window from the image at time t = 1, G(u,v) is the FFT of the matching window from the image at time t = 2, * denotes the complex conjugated and IFFT is the Inverse Fast Fourier Transform.
Reference	Heid and Kääb (2011)
Applications	Heid and Kääb (2011)
Description	A common way of approximating normalization in the Fourier domain is to consider only the phase information. By doing this, differences in image intensity, which show up only in the amplitudes, are ignored.
Advantages/ Disadvantages	- In the PC method the phase differences at every frequency contribute equally, and the dominant phase difference is taken as the displacement. Noise limited to one or few frequencies is therefore ignored, whereas noise spread across all frequencies makes the location of the peak inaccurate, and therefore also the final displacement estimate inaccurate. This can affect the matching, both positively and negatively. First, the method should be robust against different illumination between the images, because this effect is constrained to low frequencies. Second, it should also be robust to large intensity differences that are hypothesized to create erroneous matches for the NCC method. This is because snow patches and rolling/sliding rocks will be constrained to a few frequencies and thereby ignored in the PC method. Third, this method can be hypothesized to experience problems in areas with deformation, because the phase differences at the different frequencies will not agree.
Improvements	not yet known

Abbreviation	CCF-O
Algorithm	Cross-correlation on gradient images in frequency domain $$f_o(x,y) = sgn(\frac{\partial f(x,y)}{\partial x} + i\frac{\partial f(x,y)}{\partial y})$$ $$g_o(x,y) = sgn(\frac{\partial g(x,y)}{\partial x} + i\frac{\partial g(x,y)}{\partial y})$$ $$\text{where } sgn(x) = \begin{cases} 0 & \text{if } \lvert x\rvert = 0 \\ \frac{x}{\lvert x\rvert} & \text{otherwise} \end{cases}$$ where sgn is the signum function and i is the complex imaginary unit. The new images f_0 and g_0 are complex.
Reference	Fitch et al. (2002)
Applications	Heid and Kääb (2011)
Description	CCF-O computes first image intensity gradients in both dimensions, x and y. The new gradient images, called orientation images, are complex and hence consist of one real and one imaginary part, where the intensity differences in the x-direction represent the real matrix and the intensity differences in the y-direction represent the imaginary matrix. These orientation images are then matched using cross-correlation operated in the frequency domain (CCF-O) and phase correlation (PC-O; below).
Advantages	- Orientation correlation is illumination invariant. Because the orientation vector (and hence both orientation images) has zero value in uniform areas and a length of one in non-uniform areas, the correlation is not effected by uniform areas. This is a desired property in glaciological research because uniform areas are common. We also hypothesize this to be important when it comes to matching striped Landsat images after the failure of the scan line corrector (SLC-off) because the stripes are ignored when using orientation correlation.
Disadvantages	Not known (besides general image matching problems)
Improvements	Not yet known

Abbreviation	PC-O
Algorithm	Phase correlation in frequency domain on orientation images (see CCF-O)
Reference	(see CCF-O)
Applications	(see CCF-O)
Description	See CCF-O. In addition for PC-O, two types of normalizations are actually included. Firstly, orientation images are already normalized, and then the amplitudes are removed, which represents a further normalization.
Advantages/ Disadvantages	It is not yet known if two kinds of normalizations applied subsequently improve results, or remove too much of the original signal..
Improvements	Not yet known

Abbreviation	COSI-Corr
Algorithm	Phase correlation as in COSI-Corr. Algorithm not accessible.
Reference	Leprince et al. (2007)
Applications	Scherler et al. (2008), Quincey et al. (2009)
Description	The matching method in COSI-Corr estimates the phase difference in the Fourier domain as in the above PC, but does not transform the images back to the spatial domain to find the maximum of the CC. Matching windows in COSI-Corr are weighted by a bell-shaped function to avoid edge effects. The effect of this is that central parts of the window are given more weight in the matching than the outer parts of the window. The effective size of the matching window in COSI-Corr is therefore smaller. This, however, will depend on the visual contrast in the windows. COSI-Corr is freely available, though locked software, and its algorithm is not freely accessible.
Advantages/ Disadvantages	COSI-Corr uses re-weighted least squares in the matching process, and this makes COSI-Corr less sensitive to outliers within the windows. The pixels within the window hence have to move coherently for COSI-Corr to get a correct match. We therefore hypothesize that COSI-Corr can experience problems in areas with much deformation. (Note: COSI-Corr is a publicly available plug-in to ENVI, i.e. not itself a commercial software. However, its code is not open and the ENVI software required to run it is commercial off-the-shelf (COTS) software. Glaciers_cci will therefore to some extent investigate its performance, but not further rely on it).
Improvements	Not yet known

Abbreviation	LSM
Algorithm	Least-Squares Matching $$F(x,y) = G(f_x(p_1,\ldots,p_n,x',y'), f_y(p_1,\ldots,p_n,x',y'))g + o + e$$ Where F(x,y) is an image at time t=1, G(x',y') an image at time t=2, g radiometric gain, o radiometric offset, and e random noise. The geometric transformation is typically affine (6-parameter transformation) so that f_x and f_y are $$x' = p_1 + p_2x + p_3y$$ $$y' = p_4 + p_5x + p_6y$$
Reference	Förstner (1982)
Applications	Kaufmann and Ladstädter (2003), Debella-Gilo and Kääb (in press)
Description	Least-Squares Matching fits, using minimization of the squared differences between two image sections, a given geometric and radiometric model (e.g. translation, radiometric gain and offset, rotation, higher-order deformation).
Advantages	- Sub-pixel accuracy - variable geometric and radiometric offset model to be optimized
Disadvantages	- LSM needs good initial parameter estimations, usually obtained NCC. Thus it is rather a method for achieving a sub-pixel accuracy, than an independent matching algorithm for glacier flow. Its success depends on the algorithm used for the initial parameter estimates. Here, it is therefore not treated further as independent algorithm.
Improvements	Not yet known

Abbreviation	CT
Algorithm	Coherence Tracking of SAR data
Reference	Derauw (1999)
Applications	Strozzi et al. (2002)
Description	Throughout the single-look complex SAR images, small data patches are selected, a series of small interferograms with changing offset is constructed, and the coherence is estimated. The location of the coherence maximum is determined at subpixel accuracy by oversampling the single-look complex SAR image patches with zero-padding and by using a 2-D regression function to model the coherence peak with a four-point interpolator.
Advantages	- Small data patch sizes (e.g. 8x8 single-look pixels) can be used.
Disadvantages	- For areas of insufficient coherence, such as observed for wet snow and in general for acquisition time interval larger than a few days, no reliable offsets can be determined with this technique. - Computational efficiency.
Improvements	Not yet known

6.4.3 Post-processing

None of the algorithms above directly provides perfect results including only accurate and reliable results. Errors and outliers cannot be avoided because of non-perfect image and ground conditions and have to be detected and filtered as much as possible.

Most of the above tracking algorithms provide, together with the offset with highest score, the correlation coefficient (CC) or signal-to-noise ratio (SNR) of the resulting offset. This measure can directly be used to estimate the potential quality of a match, and filters based on CC or SNR thresholds. Since CC and SNR, however, depend not only on the quality of a match but also on the image texture, such filters are not strictly conclusive and should be used with care and only in combination with other post-processing measures.

The resulting displacement field can be low-pass filtered (e.g. mean, median, Gaussian, etc.) in order to filter out individual outliers. Similar to a resolution pyramid, the raw displacements can be compared to a low-pass filtered version of the field and measurements marked as outliers when the difference exceed a given threshold on displacement magnitude and direction. This procedure is very successful over dense fields, but may fail where successful matches are only scattered, or where entire groups of displacements have a similar bias. Geometric constraints such as maximum magnitude or direction sectors can be used as filters. They, however, are not very useful for large-scale applications including a number of glaciers with different speeds and orientations.

Also, for instance, gradients in glacier velocities could be used to filter, but they are very different from region to region due to the large variety of glaciers. To filter the displacements based, for instance, on the assumption that glaciers flow downslope is considered to be impossible globally, because the required accurate elevation models are not available in all glacierized areas, and because of physical reasons where this assumption does not simply hold, such as in confluence areas or for supraglacial ice topography.

It should be noted that in our opinion glaciologically sound and useful glacier displacements can only be obtained when the automatic results undergo an expert check and, potentially, editing (similar to the well acknowledged and good practice in multispectral glacier mapping). Thus, the aim of displacement filters is to support the analyst in removing the obvious errors as much as possible to focus on details that require glaciological expert judgment. Some examples of the algorithm results and the filtering techniques discussed above are presented in Figs. 6.8 to 6.12 for the test sites Karakoram and Kronebreen.

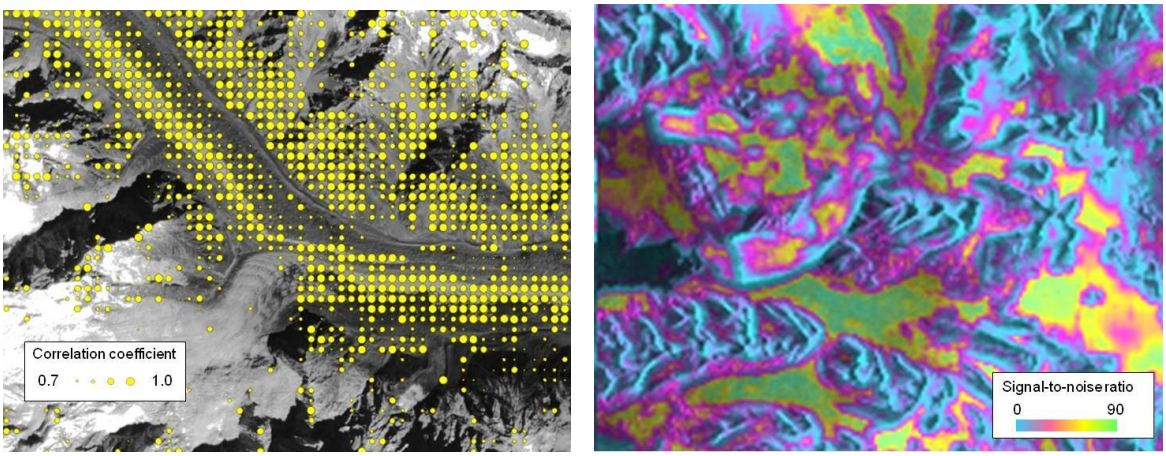

Fig 6.8: Left: Cross-correlation coefficients for a 2000-2001 Landsat ETM+ image pair over Batura glacier, Karakorum. Small circles 0.7, maximum circles 1.0, correlation coefficients < 0.7 are removed (image width: 15 km). Right: Signal-to-noise ratio (SNR) of offset-tracking between two ERS SAR images of 5 Apr and 10 May 1996 over Kronebreen, Svalbard. SNR values increase from blue over red to yellow and green (image width: 45 km). North is at top.

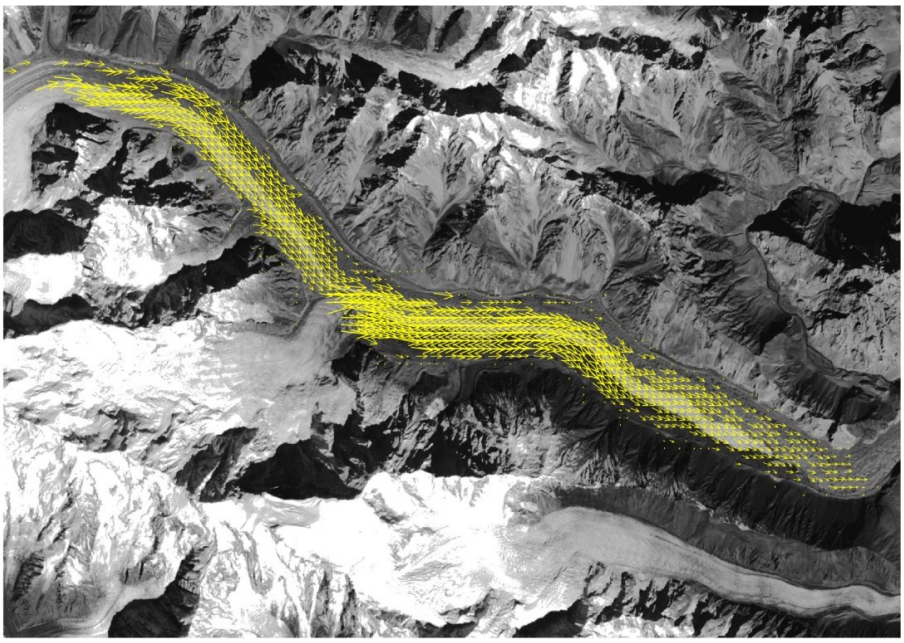

Fig. 6.9: Typical output of optical image matching after outlier filtering, displayed as vectors of velocity magnitude and direction (Batura glacier, Karakorum). North to the top. Image width: 30 km. Maximum speeds up to 140 m/yr.

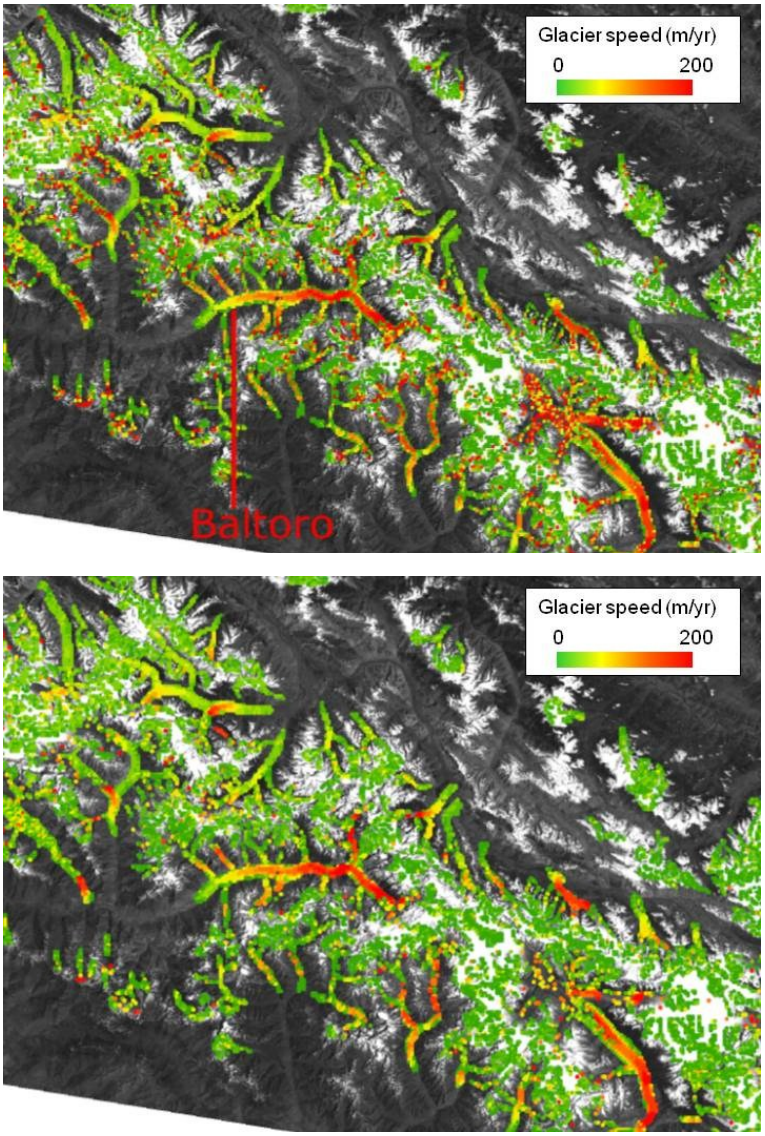

Fig. 6.10: Upper panel: Raw glacier speeds 2000-2001 as derived from a Landsat ETM+ image pair using CCF-O. Lower panel: Glacier speeds from upper panel automatically filtered using a threshold on differences between the raw measurements and a low-pass filtered version of them. Maximum speed (red) is up to 200 m / year. Image width: 170 km, North is at top.

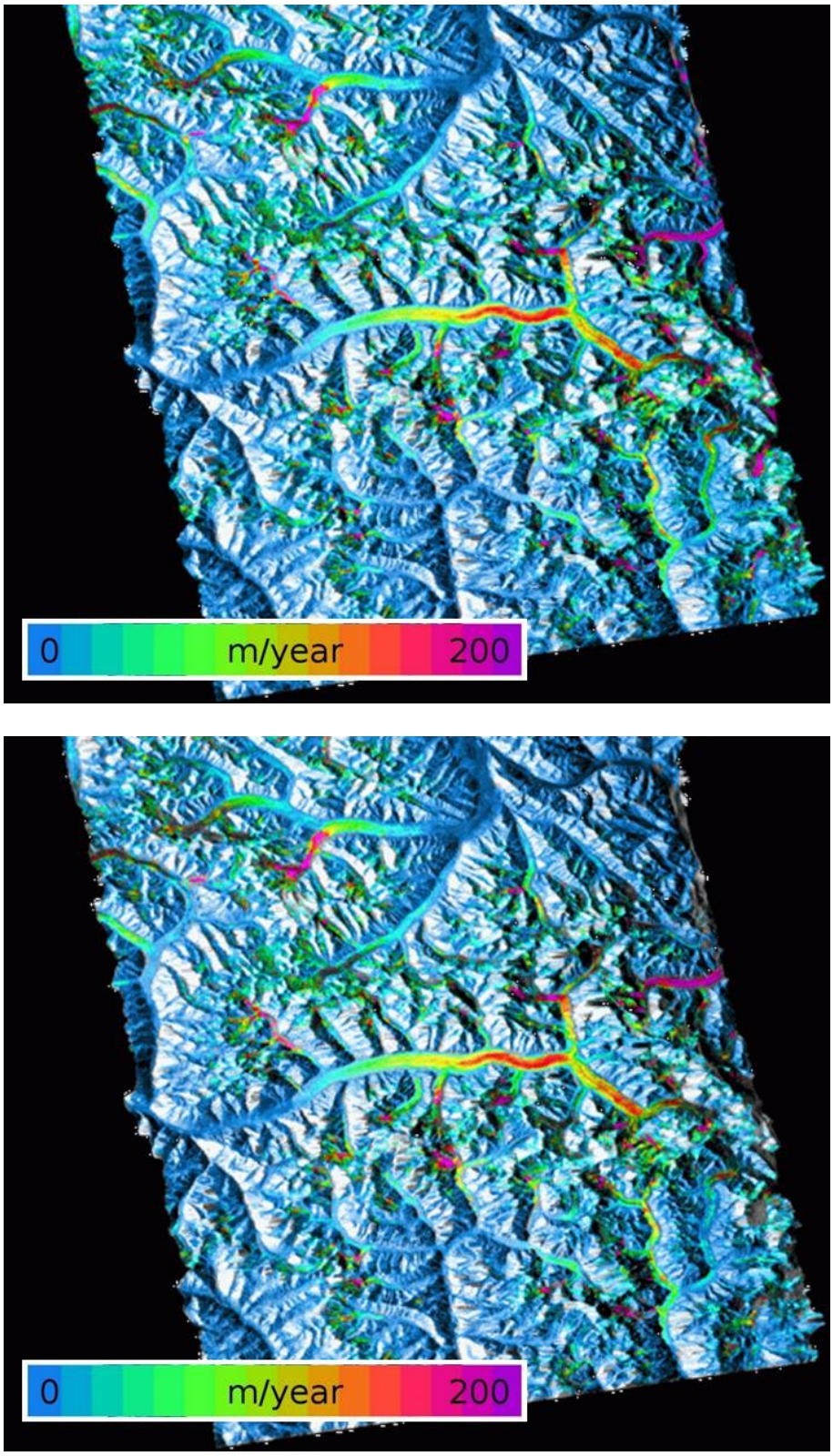

Fig. 6.11: Unfiltererd (upper panel) and filtered (lower panel) speeds from offset-tracking based on ALOS PALSAR scenes from 10.8. and 25.9. 2007 Karakorum, same region as Fig. 6.9). North to the top, image width is c. 120 km.

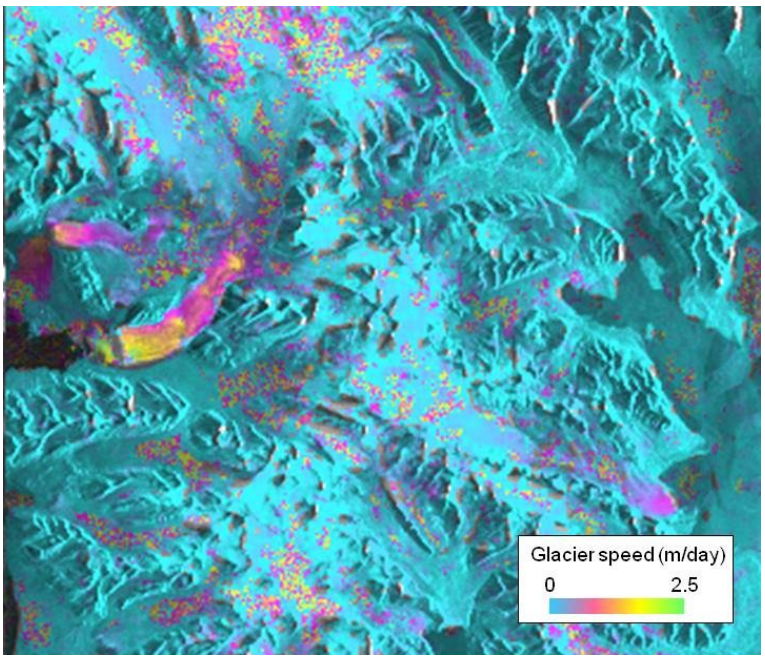

Fig. 6.12: Typical output of SAR amplitude offset-tracking without outlier filtering, displayed as velocity magnitude (Kronebreen, Svalbard). Maximum speed (yellow/green) is up to 2.5 m/d. Scene width is c. 55km, North is to the upper left.

6.5 Precision, accuracy, reliability and error budget

It is expected that the actual error budget is in practice and in most cases not necessarily dominated by the algorithm itself. Rather, the error budget of glacier displacement measurements from optical and SAR intensity offset-tracking, or SAR interferometry consists of:

- the algorithm precision;
- image co-registration, including baseline estimation for SAR interferometry (to be checked over stable terrain; accuracy close to matching precision possible);
- geometric sensor noise (theoretical image-to-image registration error; sub-pixel level, but often larger than algorithm precision);
- surface changes and transformations (i.e. representativeness of surface features for ice particle displacement; e.g. influence of different illuminations, shift of surface features; sub-pixel or pixel level);
- mismatches due to similar but not corresponding features (e.g. self-similar ogives, crevasses or seracs; errors of many pixels possible);
- ability of post-processing procedures to eliminate measurement noise and mismatches.

In summary, the accuracy of individual glacier displacement measurements from repeat satellite data using optical/SAR offset-tracking is on the order of one pixel, with areas with better accuracy, but also areas and points of much lower accuracy. Typical achievable accuracy in displacement measurements using SAR data is ≥ 0.2 pixels in slant-range and azimuth direction. Reliability, or outliers, are frequent and require special attention. By far the most accurate precision is obtained with InSAR but only for coherent regions.

6.6 Performance and intercomparison of methods

Temporal decorrelation of the radar signal due to snow fall, snow drift and melting is the main obstacle for InSAR applications over snow and ice (Rott and Siegel, 1997). Therefore, one or three-day repeat-pass data for the ERS-1/2 mission have so far been the main data source for InSAR applications in glaciology, in particular for studies of glaciers and ice streams. However, three-day repeat-pass data were only available during the ice missions in 1991, 1994 and 2011, and one-day repeat-pass data were only acquired during the years 1995-1999, when ERS-1 and ERS-2 operated in tandem. There are options to mitigate or bypass the problem of poor coherence by applying offset-tracking techniques for retrieving ice motion.

Strengths and weaknesses of the different techniques for ice motion retrieval are summarized in Table 6.1. DInSAR provides the highest accuracy, but temporal decorrelation often inhibits the application, in particular in case of multi-day time spans. Decorrelation in zones of strong ice deformation (e.g. along glacier margins) is also a problem, impairing phase unwrapping and thus prohibiting to find a solution for ice velocity even in the coherent parts. The offset-tracking techniques deliver two components of the velocity vector (slant range and azimuth) and can measure shifts at fractions of a pixel (Strozzi et al., 2002; de Lange et al., 2007). The accuracy of velocity measurement can be improved by using SAR data of longer time spans if the features are stable. In case of tracking of complex data (*speckle tracking* or *coherence tracking*) a certain degree of coherence is required. However, phase unwrapping is not necessary so that decorrelation gaps can be bridged. Complex signal based cross-correlation can also be applied in areas without obvious amplitude features which is often the case in accumulation areas. On the other hand, it can be applied also in case of complete absence of coherence. Luckman et al. (2007) studied the potential of InSAR and offset-tracking for Himalayan glaciers using ERS SAR data and found the two methods to be highly complementary, depending on flow rate and surface type. Offset-tracking by ERS and Envisat ASAR is impaired by the relative low spatial resolution compared to the new X-band SAR sensors. This prohibits the application in zones of strong shear and deformation. Hence, the new high resolution X-band SAR sensors are very attractive tools for ice motion mapping by means of tracking techniques, but are restricted to local regions.

	INSAR	**SAR offset tracking**	**Optical offset tracking**
Velocity component	LOS only	LOS (slant range) and along track	Two-dimensional horizontal in chosen projection
Accuracy of displace-ment	Fractions of wavelength: ~1 – 5 mm slant range at C-band (0.4 - 1.8 m/yr) Depends on coherence etc.	~ 0.5 - 1 m (ERS, ASAR, ALOS) ~ 0.1-0.2 m (TerraSAR-X Stripmap)	*~ 0.3 pixels (5-10 m for Landsat, 5 m for ASTER)*
Typical time interval	1, 3 days (ERS) (5 weeks on ice sheet plateau with slow motion)	n *11 days (TerraSAR-X Stripmap) n *35 days (ERS, ASAR) n *46 (ALOS PALSAR)	Months to years
Main constraints	- Loss of coherence - No sensitivity to motion along track (single pass)	- Lack of stable amplitude or complex features - Lower sensitivity than InSAR	-Lack of visual contrast (snow, shadow) - clouds

Table 6.1: Comparison of InSAR and offset-tracking techniques.

6.7 Practical considerations

The purpose of the algorithms and processing chains is to allow for a high degree of automation over large areas. In offset tracking, operator intervention can be useful, but is not necessary, for accepting the stable ground co-registration, setting the matching template sizes, and choosing a matching algorithm. For a final processing scheme it may be useful to apply two complementary algorithms, or different parameterisations of one algorithm, and compare their results, automatically (or by an operator) and to select an optimal output or combine it from the different results. This processing step can only be designed in a further version of the ATBD, after algorithm selection. It is expected that SAR interferometry will not be considered for production but only for validation, because current and future planned SAR missions with a global-scale acquisition strategy have a repeat cycle of several days.

References

Abermann, J., Fischer, A., Lambrecht, A. and Geist, T. (2010): On the potential of very high-resolution repeat DEMs in glacial and periglacial environments. The Cryosphere, 4, 53-65.

Abshire, J.B., Sun, X.L., Riris, H., Sirota, J.M., McGarry, J.F., Palm, S., Yi, D.H. and Liiva, P. (2005): Geoscience Laser Altimeter System (GLAS) on the ICESat mission: On-orbit measurement performance, Geophysical Research Letters, 32, L21S02, 1-4.

Albert, T.H. (2002): Evaluation of remote sensing techniques for ice-area classification applied to the tropical Quelccaya Ice Cap, Peru. Polar Geography, 26 (3), 210-226.

Andreassen, L.M. (1999): Comparing traditional mass balance measurements with long-term volume change extracted from topographical maps: a case study of Storbreen glacier in Jotunheimen, Norway, for the period 1940–1997. Geografiska Annaler, 81A (4), 467-476.

Andreassen, L.M., Paul, F., Kääb, A. and Hausberg, J.E. (2008): Landsat-derived glacier inventory for Jotunheimen, Norway, and deduced glacier changes since the 1930s. The Cryosphere, 2, 131-145.

Aniya, M., Sato, H., Naruse, R., Skvarca, P. and Casassa, G. (1996): The use of satellite and airborne imagery to inventory outlet glaciers of the Southern Patagonia Icefield, South America. Photogrammetric Engineering and Remote Sensing, 62, 1361-1369.

Atwood, D., Meyer, F. and Arendt, A. (2010): Using L-band SAR coherence to delineate glacier extent. Canadian Journal of Remote Sensing, 36, S186-S195.

Bamber, J. (1987): Internal reflecting horizons in Spitsbergen glaciers. Annals of Glaciology, 9, 5-10.

Bamber, J. (1994): Ice-Sheet Altimeter Processing Scheme. International Journal of Remote Sensing, 15 (4), 925-938.

Bamber, J. (1995): Analysis of satellite-altimeter height measurements above continental ice sheets. Journal of Glaciology, 41 (137), 206-206.

Bayr, K. J., Hall, D.K. and Kovalick, W.M. (1994): Observations on glaciers in the eastern Austrian Alps using satellite data. International Journal of Remote Sensing, 15, 1733-1742.

Berthier, E., Arnaud, Y., Vincent, C. and Rémy, F. (2006): Biases of SRTM in high-mountain areas: Implications for the monitoring of glacier volume changes. Geophys. Res. Lett., 33, L08502.

Berthier, E., Arnaud, Y., Kumar, R., Ahmad, S., Wagnon, P. and Chevallier, P. (2007): Remote sensing estimates of glacier mass balances in the Himachal Pradesh (Western Himalaya, India). Remote Sensing of Environment, 108, 327-338.

Berthier, E. and Toutin, T. (2008): SPOT5-HRS digital elevation models and the monitoring of glacier elevation changes in North-West Canada and South-East Alaska. Remote Sensing of Environment, 112, 2443-2454.

Berthier, E., Schiefer E., Clarke, G.K.C.,Menounos, B. and Rémy, F. (2010): Contribution of Alaskan glaciers to sea-level rise derived from satellite imagery. Nature Geoscience, 3 (2), 92-95.

Binaghi, E., Madella, P., Montesano, M.P. and Rampini, A. (1997): Fuzzy contextual classification of multisource remote sensing images. IEEE Transactions on Geoscience and Remote Sensing, GE-35 (2), 326-339.

Bishop, M.P., Barry, R.G., Bush, A.B.G., Copeland, L., Dwyer, J.L., Fountain, A.G., Haeberli, W., Hall, D.K., Kääb, A., Kargel, J.S., Molnia, B.F., Olsenholler, J.A., Paul, F.,

Raup, B.H., Shroder, J.F., Trabant, D.C., Wessels, R. (2004): Global Land Ice Measurements from Space (GLIMS): Remote sensing and GIS investigations of the Earth's cryosphere. Geocarto International, 19 (2), 57-85.

Bouillon, A., Bernard, M., Gigord, P., Orsoni, A., Rudowski, V. and Baudoin, A. (2006): SPOT 5 HRS geometric performances: Using block adjustment as a key issue to improve quality of DEM generation. ISPRS Journal of Photogrammetry and Remote Sensing, 60, 134-146.

Brenner, A.C., Bindschadler, R.A., Thomas, R.H. and Zwally, H.J. (1983): Slope-induced errors in radar altimetry over continental ice sheets. Journal of Geophysical Research: Oceans, 88, 1617-1623.

Brenner, A., Zwally, H., Bentley, C., Csatho, B., Harding, D., Hofton, M., Minster, B., Roberts, L., Saba, J. and Thomas R.H., Yi, D. (2003): Derivation of Range and Range Distributions From Laser Pulse Waveform Analysis for Surface Elevations, Roughness, Slope, and Vegetation Heights, Geoscience Laser Altimeter System (GLAS). Algorithm theoretical basis document 4.1, NASA Goddard Space Flight Center.

Brenner, A.C., DiMarzio, J.R. and Zwally, H.J. (2007): Precision and accuracy of satellite radar and laser altimeter data over the continental ice sheets. IEEE Transactions on Geoscience and Remote Sensing, 45, 321-331.

Brooks, R.L., Campbell, W.J., Ramseier, R.O., Stanley, H.R. and Zwally, H.J. (1978): Ice sheet topography by satellite altimetry. Nature, 274, 539-543.

Brown G. S. (1977): The average impulse response of a rough surface and its applications. IEEE Transactions on Antennas Propagation, AP-25, 67-74.

Chavez, P. (1988): An improved dark-object subtraction technique for at- mospheric scattering correction of multispectral data. Remote Sensing of Environment, 24, 459-479.

Cox, L.H. and March, R.S. (2004): Comparison of geodetic and glaciologicalmass-balance techniques, Gulkana Glacier, Alaska, USA. Journal of Glaciology, 50 (170), 363-370.

Davis, C. H. (1996): Comparison of Ice-Sheet Satellite Altimeter Retracking Algorithms. IEEE Transactions on Geoscience and Remote Sensing, 34, (1), 229-236.

Davis, C. H. and Moore, R. K. (1993): A combined surface- and volume-scattering model for ice-sheet radar altimetry. Journal of Glaciology, 39 (133), 675-686.

Davis, C. H. and Poznyak, V. I. (1993): The depth of penetration in Antarctic firn at 10 GHz. IEEE Transactions on Geoscience and Remote Sensing, 31 (5), 1107-1111.

Debella-Gilo, M. and Kääb, A. (in press): Locally adaptive template sizes in matching repeat images of Earth surface mass movements. ISPRS Journal of Photogrammetry and Remote Sensing.

Derauw D. (1999): DInSAR and coherence tracking applied to glaciology: The example of Shirase Glacier. *Proceedings FRINGE'99*, Liège, Belgium, 1999.

DMK/DPK (Deutschschweizerische Mathematikkommission/Physikkommision) (1977): Formeln und Tafeln. Mathematik - Statistik - Physik. Zürich, Orell Füssli Verlag.

Dowdeswell, J.A. and Evans, S. (2004): Investigations of the form and flow of ice sheets and glaciers using radio-echo sounding. Institute of Physics, Publishing Reports on Progress in Physics, 67, 1821-1861.

Dozier, J. (1989): Spectral signature of alpine snow cover from Landsat 5 TM. Remote Sensing of Environment, 28, 9-22.

Duda, D.P., Spinhirne, J.D. and Eloranta, EW. (2001): Atmospheric multiple scattering effects on GLAS altimetry. I. Calculations of single pulse bias. IEEE Transactions on Geoscience and Remote Sensing, 39(1), 92 -101.

Elachi, C. (1988): Spaceborne Radar Remote Sensing: Applications and Techniques. IEEE Press, New York.

Elsberg, D.H., W.D. Harrison, K.A. Echelmeyer and R.M. Krimmel (2001): Quantifying the effects of climate and surface change on glacier mass balance. Journal of Glaciology, 47 (159), 649-658.

ESA Online News Bulletin (2007): Sentinel-3 The Ocean and Medium-Resolution Land Mission for GMES Operational Services, ESA Bulletin 131.

Evans, S. (1965): Dielectric properties of ice and snow - a review. Journal of Glaciology, 5 (42), 773-792.

Farr, T. G., Rosen, P. A., Caro, E., Crippen, R., Duren, R., Hensley, S., Kobrick, M., Paller, M., Rodriguez, E., Roth, L., Seal, D., Shaffer, S., Shimada, J., Umland, J.,Werner, M., Oskin, M., Burbank, D. and Alsdorf, D. (2007): The Shuttle Radar Topography Mission. Rev. Geophys., 45, RG2004.

Fitch, A.J., Kadyrov, A., Christmas, W.J. and Kittler, J. (2002): Orientation correlation. British Machine Vision Conference, 133-142.

Frey, H. Paul, F. and Strozzi, T. (in revision): Compilation of a glacier inventory for the western Himalayas from satellite data: Methods, challenges and results. Remote Sensing of Environment.

Ferguson, A.C., Davis, C.H. and Cavanaugh, J.E. (2004): An autoregressive model for analysis of ice sheet elevation change time series. IEEE Transactions on Geoscience and Remote Sensing, 42 (11), 2426-2436.

Fricker, HA., Borsa, A., Minster, B., Carabajal, C., Quinn, K. and Bills, B. (2005): Assessment of ICESat performance at the Salar de Uyuni, Bolivia. Geophysical Research Letters, 32 (L21S06), 1-5.

Fu L-L. and Cazenave, A. (2001): Satellite Altimetry and Earth Science, Academic Press, International Geophysics Series, 69, ISBN- 0-12-269454-3.

Fujisada, H., Bailey, G., Kelly, G., Hara, S. and Abrams, M. (2005): ASTER DEM performance. IEEE Transactions on Geoscience and Remote Sensing, 43, 2707-2714.

Fujita, S., Shiralshi, M. and Mac, S. (1992): Measurement on the microwave-dielectric constant of ice by the standing wave method. In: N. Maeno and T. Hondoh (Editors), Physics and Chemistry of Ice. Univ. Press. Sapporo, 415-421.

Förstner, W. (1982): On the geometric precision of digital image correlation. ISPRS Symposium Mathematical Models, Accuracy Aspects and Quality Control, 176-189.

Förstner, W. (2000): Image preprocessing for feature extraction in digital intensity, color and range images. In: A. Dermanis, A. Grün and F. Sansò (Eds.), Geomatic Methods for the Analysis of Data in the Earth Sciences. Lecture Notes in Earth Sciences. Springer. 165-189.

Gardner, A.S., Moholdt, G., Wouters, B., Wolken, G., Burgess, D. Sharp, M., Cogley, J., Braun, C. and Labine, C. (2011): Sharply increased mass loss from glaciers and ice caps in the Canadian Arctic Archipelago. Nature, 473, 357-360.

Geist, T., E. Lutz and J. Stötter. (2003): Airborne laser scanning technology and its potential for applications in glaciology. *In Proceedings of the ISPRSWorkshop on 3-D Reconstruction from Airborne Laserscanner and INSAR Data*. Dresden, International Society for Photogrammetry and Remote Sensing, 101-106.

Geist, T., Elvehøy, H., Jackson, M. and Stötter, J. (2005): Investigations on intra-annual elevation changes using multi-temporal airborne laser scanning data: case study Engabreen, Norway. Annals of Glaciology, 42, 195-201.

Gjermundsen, E.F., Mathieu, R., Kääb, A., Chinn, T., Fitzharris, B. and Hagen, J.O. (2011): Assessment of multispectral glacier mapping methods and derivation of glacier area changes, 1978-2002, in the central Southern Alps, New Zealand, from ASTER satellite data, field survey and existing inventory data. Journal of Glaciology, 57 (204), 667-683.

Glaciers_cci (2011a): User Requirements Document (URD): Prepared by the Glaciers_cci consortium, 45 pp.

Glaciers_cci (2011b): Product Specifications Document (PSD): Prepared by the Glaciers_cci consortium, 43 pp.

Glaciers_cci (2011c): Data Access Requirements Document (DARD): Prepared by the Glaciers_cci consortium, 46 pp.

Haeberli, W. (2006): Integrated perception of glacier changes: a challenge of historical dimensions. In: Knight, P.G. (ed.): Glacier science and environmental change. Oxford: Blackwell Publishing, 423-430.

Hagen, J.O., Eiken, T., Kohler, J. and Melvold, K. (2005): Geometry changes on Svalbard glaciers: mass-balance or dynamic response? Annals of Glacioliology, 42, 255-261.

Hall, D.K., Chang, A.T.C. and Siddalingaiah, H. (1988): Reflectances of glaciers as calculated using Landsat 5 Thematic Mapper data. Remote Sensing of Environment, 25, 311-321.

Hall, D.K., Williams, R.S., Barton, J.S. Sigurdsson, O. Smith, L.C. and Garvin, J.B. (2000): Evaluation of remote-sensing techniques to measure decadal-scale changes of Hofsjokull ice cap, Iceland. Journal of Glaciology, 46 (154), 375-388.

Hanssen, R.F. 2001. Radar Interferometry. Kluwer Academic Publ., Dordrecht.

Heid, T. and Kääb, A. (2011b): Worldwide widespread decadal-scale decrease of glacier speed revealed using repeat optical satellite images. The Cryosphere Discussion, 5, 3025-3051.

Heid, T. and Kääb, A. (2011a): Evaluation of different image matching methods for deriving glacier surface displacements globally from optical satellite imagery. Remote Sensing and Environment, under revision.

Hirano, A., Welch, R. and Lang, H. (2003): Mapping from ASTER stereo image data: DEM validation and accuracy assessment. ISPRS Journal of Photogrammetry and Remote Sensing, 57, 356-370.

Howat, I.M., Smith, B.E., Joughin, I. and Scambos, T.A. (2008): Rates of southeast Greenland ice volume loss from combined ICESat and ASTER observations. Geophysical Research Letters, 35, L17505.

Huss, M., Bauder, A. and Funk, M. (2009): Homogenization of long term mass-balance time series. Annals of Glaciology, 50 (50), 198-206.

Huss, M. (2011): Present and future contribution of glaciers to runoff from macroscale drainage basins in Europe. Water Resources Research, 47, W07511.

IGOS (2007): Integrated Global Observing Strategy Cryosphere theme report - For the monitoring of our environment from space and from Earth. Geneva: World Meteorological Organization. WMO/TD-No. 1405, 100 pp.

Iwasaki, A. and Fujisada, H. (2005): ASTER geometric performance, Geoscience and Remote Sensing. IEEE Transactions on Geoscience and Remote Sensing, 43, 2700-2706.

Jacobs, J.D., Simms, E.L. and Simms, A. (1997): Recession of the southern part of Barnes Ice Cap, Baffin Island, Canada, between 1961 and 1993, determined from digital mapping of Landsat TM. Journal of Glaciology, 43 (143), 98-102.

JPL (2011): ASTER spectral library Version 2.0. Online at: http://speclib.jpl.nasa.gov/

Kaufmann, V. and Ladstädter, R. (2003): Quantitative analysis of rock glacier creep by means of digital photogrammetry using multi-temporal aerial photographs: two case studies in the Austrian Alps. Eighth International Conference on Permafrost. 1. Balkema. 525-530.

Korona, J., Berthier, E., Bernard, M., Rémy, F. and Thouvenot, E. (2009): SPIRIT. SPOT 5 stereoscopic survey of Polar Ice: Reference Images and Topographies during the fourth

International Polar Year (2007-2009): ISPRS Journal of Photogrammetry and Remote Sensing, 64, 204-212.

Kovacs, A., Gow, A. J. and Morey, R.M. (1995): The in-situ dielectric constant of polar firn revisited. Cold Regions Science and Technology, 23 (3), 245-256.

Kääb, A. and Vollmer, M. (2000): Surface geometry, thickness changes and flow fields on creeping mountain permafrost: automatic extraction by digital image analysis. Permafrost and Periglacial Processes. 11(4), 315-326.

Kääb, A., Paul, F., Maisch, M., Hoelzle, M. and Haeberli, W. (2002): The new remote-sensing-derived Swiss glacier inventory: II. First Results. Annals of Glaciology, 34, 362-366.

Kääb, A., Huggel, C., Paul, F., Wessels, R., Raup, B., Kieffer, H. and Kargel, J. (2002): Glacier monitoring from ASTER imagery: Accuracy and Applications. *Proceedings of EARSeL-LISSIG Workshop Observing our Cryosphere from Space*, 2,43-53.

Kääb, A., Huggel, C., Fischer, L., Guex, S., Paul, F., Roer, I., Salzmann, N., Schlaefli, S., Schmutz, K., Schneider, D., Strozzi, T. and Weidmann, W. (2005): Remote sensing of glacier- and permafrost-related hazards in high mountains: an overview. Natural Hazards and Earth System Sciences, 5, 527-554.

Kääb, A. (2005): Remote Sensing of Mountain Glaciers and Permafrost Creep. Schriftenreihe Physische Geographie. Glaziologie und Geomorphodynamik. 48. University of Zurich, Zurich.

Kääb, A. (2008): Glacier Volume Changes Using ASTER Satellite Stereo and ICESat GLAS Laser Altimetry, A Test Study on Edgeya, Eastern Svalbard, IEEE Transactions on Geoscience and Remote Sensing, 46, 2823-2830.

Kwok, R., Siegert, M.J. and Carsey, F.D. (2000) Ice motion over Lake Vostok, Antarctica: constraints on inferences regarding the accreted ice. Journal of Glaciology, 46 (155), 689-694.

Larsen, C.F., Motyka, R.J., Arendt, A.A., Echelmeyer, K.A. and Geissler, P.E. (2007): Glacier changes in southeast Alaska and northwest British Columbia and contribution to sea level rise. Journal of Geophysical Research-Earth Surface, 112, F01007.

Le Bris, R., Paul, F., Frey, H. and Bolch, T. (2011): A new satellite-derived glacier inventory for western Alaska. Annals of Glaciology, 52 (59), 135-143.

Leprince, S., Ayoub, F., Klinger, Y. and Avouac, J.P. (2007): Co-Registration of Optically Sensed Images and Correlation (COSI-Corr): an operational methodology for ground deformation measurements. IGARSS: 2007 IEEE International Geoscience and Remote Sensing Symposium, Vols 1-12, 1943-1946.

Li, S. and Sturm, M. (2002): Patterns of wind-drifted snow on the Alaskan Arctic Slope detected with ERS-1 interferometric SAR. Journal of Glaciology, 48 (163), 495-504.

Lillesand, T., Kiefer, R. and Chipman, J. (2004): Remote Sensing and Image Interpretation, 5 editon, John Wiley & Sons, Inc., Hoboken, NJ.

Maetzler, C. (1987): Applications of the interaction of microwaves with natural snow cover. Remote Sensing Reviews, 2, 259-387.

Maetzler, C. (1996) Microwave permittivity of dry snow, IEEE Transactions on Geoscience and Remote Sensing, 34 (2), 573-581.

Maetzler, C. (1998): Improved Born approximation for scattering of radiation in a granular medium. Journal of Applied Physics, 83 (11), 6111-6117.

Maetzler, C. (2006): Thermal Microwave Radiation: Applications for Remote Sensing. Stevenage, U.K.: Institute of Engineering and Technology, 52, ch. 5, Microwave dielectric properties of ice, 455-462.

Maetzler, C. and Wegmueller, U. (1987): Dielectric properties of freshwater ice at microwave frequencies. Journal of Applied Physics, 20, 1623-1630.

Martin, T.V., Zwally, H.J., Brenner A.C. and Bindschadler R.A. (1983): Analysis and retracking of continental ice sheet radar altimetry wave-forms. Journal of Geophysical Research, 88, 1608-1616.

Mavrocordatos C., Berruti B., Aguirre M. and Drinkwater M. (2007): The Sentinel-3 mission and its Topography element. *Proceeding of IEEE IGARSS 2007*, Barcelona, Spain.

Moholdt, G., Hagen, J.O., Eiken, T. and Schuler, T.V. (2010a): Geometric changes and mass balance of the Austfonna ice cap, Svalbard. The Cryosphere, 4, 21-34.

Moholdt, G., Nuth, C., Hagen, J.O. and Kohler, J. (2010b): Recent elevation changes of Svalbard glaciers derived from ICESat laser altimetry. Remote Sensing of Environment, 114 (11), 2756-2767.

Mohr, J.J. and Madsen, S.N. (1996) Multi-pass interferometry for studies of glacier dynamics, ESA Workshop Applicat. ERS SAR Interferometry: FRINGE'96: Univ. Zurich.

Moore, J.C., Paelli, A., Ludwig, F., Blatter, H., Jania, J., Gadek, B., Glowacki, P., Mochnacki, D. and Isaksson, E. (1999): High-resolution hydrothermal structure of Hansbreen, Spitsbergen, mapped by ground-penetrating radar. Journal of Glaciology, 45 (151), 524-532.

Müller, K. (2011): Microwave penetration in polar snow and ice: Implications for GPR and SAR, PhD Thesis: Department of Geosciences, University of Oslo.

Nuth, C., Moholdt, G., Kohler, J., Hagen, J.O. and Kääb, A. (2010): Svalbard glacier elevation changes and contribution to sea level rise. Journal of Geophysical Research, 115 (F1), F01008.

Nuth, C. and Kääb, A. (2011): Co-registration and bias corrections of satellite elevation data sets for quantifying glacier thickness change. The Cryosphere, 5, 271-290.

Nuth C., Schuler T.V., Kohler J., Altena B. and Hagen J.O. (*in press*): Estimating the long term calving flux of Kronebreen, Svalbard, from geodetic elevation changes and mass balance modelling, Journal of Glaciology.

Paul, F. (2001): Evaluation of different methods for glacier mapping using Landsat TM. EARSeL Workshop on Remote Sensing of Land Ice and Snow, Dresden, 16.-17.6.2000. EARSeL eProceedings, 1, 239-245.

Paul, F. (2002): Changes in glacier area in Tyrol, Austria, between 1969 and 1992 derived from Landsat 5 TM and Austrian Glacier Inventory data. International Journal of Remote Sensing, 23 (4), 787-799.

Paul, F. (2008): Calculation of glacier elevation changes with SRTM: is there an elevation-dependent bias? Journal of Glaciology, 54 (188), 945-946.

Paul, F. (2010): Towards a global glacier inventory from satellite data. Geographica Helvetica, 65 (2), 103-112.

Paul, F. and Kääb, A. (2005): Perspectives on the production of a glacier inventory from multispectral satellite data in the Canadian Arctic: Cumberland Peninsula, Baffin Island. Annals of Glaciology, 42, 59-66.

Paul, F. and Haeberli, W. (2008): Spatial variability of glacier elevation changes in the Swiss Alps obtained from two digital elevation models, Geophysical Research Letters, 35, L21502.

Paul, F. and Andreassen, L.M. (2009): A new glacier inventory for the Svartisen region, Norway, from Landsat ETM+ data: challenges and change assessment. Journal of Glaciology, 55 (192), 607-618.

Paul, F. and Hendriks, J. (2010): Optical remote sensing of glaciers. In: Pellikka, P. and Rees, W.G (Eds.)., Remote Sensing of Glaciers - Techniques for Topographic, Spatial and Thematic Mapping of Glaciers. CRC Press, Taylor and Francis Group, Leiden, 137-152.

Paul, F., Kääb, A., Maisch, M., Kellenberger, T. and Haeberli, W. (2002): The new remote-sensing-derived Swiss glacier inventory: I. Methods. Annals of Glaciology, 34, 355-361.

Paul, F., Huggel, C., Kääb, A. and Kellenberger, T. (2003): Comparison of TM-derived glacier areas with higher resolution data sets. *EARSeL Workshop on Remote Sensing of Land Ice and Snow, Bern, 11.-13.3.2002*. EARSeL eProceedings, 2, 15-21.

Paul, F., Huggel, C. and Kääb, A. (2004): Combining satellite multispectral image data and a digital elevation model for mapping of debris-covered glaciers. Remote Sensing of Environment, 89 (4), 510-518.

Paul, F., Barry, R., Cogley, G., Frey, H., Haeberli, W., Ohmura, A., Ommanney, S., Raup, B., Rivera, A., Zemp, M. (2009): Recommendations for the compilation of glacier inventory data from digital sources. Annals of Glaciology, 50 (53), 119-126.

Paul, F. and Hendriks, J. (2010): Optical remote sensing of glaciers. In: Pellikka, P. and Rees, W.G (Eds.)., Remote Sensing of Glaciers - Techniques for Topographic, Spatial and Thematic Mapping of Glaciers. CRC Press, Taylor and Francis Group, Leiden, 137-152.

Paul, F., Andreassen, L.M. and Winsvold, S.H. (2011): A new glacier inventory for the Jostedalsbreen region, Norway, from Landsat TM scenes of 2006 and changes since 1966. Annals of Glaciology, 52 (59), 144-153

Paul, F., Frey, H. and Le Bris, R. (in press): A new glacier inventory for the European Alps from Landsat TM scenes of 2003: Challenges and results. Annals of Glaciology, 52 (59).

Pritchard, H., Murray, T., Luckman, A., Strozzi, T and Barr, S. (2005): Glacier surge dynamics of Sortebræ, east Greenland, from synthetic aperture radar feature tracking. Journal of Geophysical Research, 110, F03005.

Pritchard, H.D., Arthern, R.J., Vaughan, D.G. and Edwards, L.A. (2009): Extensive dynamic thinning on the margins of the Greenland and Antarctic ice sheets. Nature, 461, 971-975.

Quincey, D.J. and Glasser, N.F. (2009): Morphological and ice-dynamical changes on the Tasman Glacier, New Zealand, 1990-2007. Global and Planetary Change, 68(3), 185-197.

Qunzhu, Z., Meisheng, C., Xuezhi, F., Fengxian, L., Xianzhang, C. and Wenkuna, S. (1983): A study of spectral reflection characteristics for snow, ice and water in the north of China. IAHS, 145, 451-462.

Rabus, B., Eineder, M., Roth, A. and Bamler, R. (2003): The shuttle radar topography mission - a new class of digital elevation models acquired by spaceborne radar. ISPRS Journal of Photogrammetry and Remote Sensing, 57, 241-262.

Racoviteanu, A.E., Williams, M.W. and Barry, R.G. (2008): Optical remote sensing of glacier characteristics: a review with focus on the Himalaya. Sensors, 8, 3355-3383.

Racoviteanu, A.E., Paul, F., Raup, B., Khalsa, S.J.S. and Armstrong, R. (2009): Challenges in glacier mapping from space: recommendations from the Global Land Ice Measurements from Space (GLIMS) initiative. Annals of Glaciology, 50 (53), 53-69.

Remy, F., Mazzega, P., Houry, S., Brossier, C. and Minster, J.F. (1989): Mapping of the topography of continental ice by inversion of satellite-altimeter data. Journal of Glaciology, 35 (119), 98-107.

Ridley, J.K. and Partington K.C. (1988): A model of satellite radar altimeter return from ice sheets. International Journal of Remote Sensing, 9 (4), 601-624.

Rignot, E., Echelmeyer, K. and Krabill, W. (2001): Penetration depth of interferometric synthetic-aperture radar signals in snow and ice, Geophysical Research Letters, 28, 3501-3504.

Rignot, E., Rivera, A. and Casassa, G. (2003): Contribution of the Patagonia Icefields of South America to sea level rise. Science, 302, 434-437.

Rodriguez, E., Morris, C.S. and Belz, J.E. (2006): A global assessment of the SRTM performance. Photogrammetric Engineering and Remote Sensing, 72, 249-260.

Roemer, S., Legresy, B., Horwath, M. and Dietrich, R. (2007): Refined analysis of radar altimetry data applied to the region of the subglacial Lake Vostok/Antarctica. Remote Sensing of Environment, 106, 269-284.

Rosen, P. A., Hensley, S., Joughin, I. R., Li, F. K., Madsen, S. N., Rodriguez, E. and Goldstein, R. M. (2000): Synthetic aperture radar interferometry - Invited paper, Proceedings IEEE, 88, 333-382.

Rosmorduc, V., Benveniste, J., Bronner, E., Dinardo, S., Lauret, O., Maheu, C., Milagro, M. and Picot, N. (2011): Radar Altimeter Tutorial, J. Benveniste, N. Picot, Editors.

Rott, H., Sturm, K. and Miller, H. (1993): Active and passive microwave signatures of Antarctic firn by means of field measurements and satellite data. Annals of Glaciology, 17, 337-343.

Rott, H. and Markl, G. (1989): Improved snow and glacier monitoring by the Landsat Thematic Mapper. *Proceedings of a workshop on Landsat Themaic Mapper applications*, ESA, SP-1102, 3-12.

Rott, H. and Siegel, A. (1997): Glaciological Studies in the Alps and in Antarctica Using ERS Interferometric SAR. ERS SAR Interferometry, *Proceedings of ESA Fringe 96 Workshop*, Zürich Oct. 1996. ESA SP 406, II, 149-159.

Rott, H., Stuefer, M., Siegel, A., Skvarca, P. and Eckstaller, A. (1998) Mass fluxes and dynamics of Moreno Glacier, Southern Patagonia Icefield. Geoph. Res. Letters, 25 (9), 1407-1410.

Rott, H., Müller, F., Nagler, T. and Floricioiu, D. (2010): The imbalance of glaciers after disintegration of Larsen B ice shelf, Antarctic Peninsula. The Cryosphere. 4, 1607–1633, 2010.

Sauber, J., Molnia, B., Carabajal, C., Luthcke, S. and Muskett, R. (2005): Ice elevations and surface change on the Malaspina Glacier, Alaska, Geophysical Research Letters, 32, L23S01.

Scambos, T.A., Dutkiewicz, M.J., Wilson, J.C. and Bindschadler, R.A. (1992): Application of image cross-correlation to the measurement of glacier velocity using satellite image data. Remote Sensing of Environment, 42 (3), 177-186.

Schenk, T. (1999): Digital Photogrammetry, 1, TerraScience, Laurelville, Ohio.

Scherler, D., Leprince, S. and Strecker, M.R. (2008): Glacier-surface velocities in alpine terrain from optical satellite imagery - Accuracy improvement and quality assessment. Remote Sensing of Environment, 112 (10), 3806-3819.

Schiefer, E., Menounos, B. and Wheate, R. (2007): Recent volume loss of British Columbian glaciers, Canada. Geophysical Research Letteers, 34, L16503.

Schutz, B.E., Zwally, H.J., Shuman, C.A., Hanock, D. and DiMarzio, J.P. (2005): Overview of the ICESat Mission. Geophysical Research Letters, 32, L21S01.

Scott, J.B.T., Nienow, P., Mair, D., Parry, V., Morris, E. and Wingham, D.J. (2006): Importance of seasonal and annual layers in controlling backscatter to radar altimeters across the percolation zone of an ice sheet. Geophysical Research Letters, 33, L24502.

Shepherd, A., Wingham, D., Ridout, A. and Muir, A. (2010): Initial Assessment of CryoSat-2 Performance over Continental Ice. Proc. of American Geophysical Union, Fall Meeting 2010.

Shukla, A., M.K. Arora and R.P. Gupta (2011): Synergistic approach for mapping debris-covered glaciers using optical-thermal remote sensing data with inputs from geomorphometric parameters. Remote Sensing of Environment, 114 (7), 1378-1387.

Sidjak, R.W. and Wheate, R.D. (1999): Glacier mapping of the Illecillewaet icefield, British Columbia, Canada, using, Landsat TM and digital elevation data. International Journal of Remote Sensing, 20, 273-284.

Sihvola, A.H. and Kong, J.A. (1988): Effective permittivity of dielectric mixtures. IEEE Transactions on Geoscience and Remote Sensing, 26 (4), 420-429.

Skvarca, P., Raup, B. and De Angelis, H. (2003): Recent behaviour of Glaciar Upsala, a fast-flowing calving glacier in Lago Argentino, southern Patagonia. Annals of Glaciology. 36, 184-188.

Slobbe, D.C., Lindenbergh, R.C. and Ditmar, P. (2008): Estimation of volume change rates of Greenland's ice sheet from ICESat data using overlapping footprints. Remote Sensing of Environment, 112, 4204-4213.

Sneep, M. and Ubach, W. (2005): Direct measurement of the Rayleigh scattering cross section in various gases. Journal of Quantitative Spectroscopy and Radiative Transfer, 92 (3), 293-310.

Strozzi, T., Wegmüller, U. and Maetzler, C. (1999): Mapping wet snow with SAR interferometry. International Journal of Remote Sensing, 20 (12), 2395-2403.

Strozzi T., Murray, T., Wegmüller, U. and Werner, C. (2002): Glacier Motion Estimation Using SAR Offset-Tracking Procedures. IEEE Transactions on Geoscience and Remote Sensing, 40 (11), 2384-2391.

Strozzi, T., Paul, F. and Kääb, A. (2010): Glacier mapping with ALOS PALSAR data within the ESA GlobGlacier project. Proceedings of the ESA Living Planet Symposium, 28 June - 2 July 2010, Bergen, Norway, ESA SP-686.

Stuefer, M. (1999) Investigations on mass balance and dynamics of Moreno Glacier based on field measurements and satellite imagery. PhD Thesis, Univ. of Innsbruck, Austria.

Thibert, E., Blanc, R., Vincent, C. and Eckert, N. (2008): Glaciological and volumetric mass-balance measurements: error analysis over 51 years for Glacier de Sarennes, French Alps. Journal of Glaciology, 54 (186), 522-532.

Toutin, T. (2002): Three-dimensional topographic mapping with ASTER stereo data in rugged topography. IEEE Transactions on Geoscience of Remote Sensing, 40, 2241-2247.

Toutin, T. (2004): Review article: Geometric processing of remote sensing images: models, algorithms and methods. International Journal of Remote Sensing, 25, 1893-1924.

Toutin, T. (2008): ASTER DEMs for geomatic and geoscientific applications: a review. International Journal of Remote Sensing, 29, 1855-1875.

Tsang, L., Kong, J.A. and Shin, R.T. (1985): Theory of Microwave Remote Sensing. NewYork: Wiley-Interscience.

Ulaby, F.T., Moore, R.K. and Fung, A.K., Microwave remote sensing: active and passive, Addison-Wesley Publishing Company, London [etc.], (1982).

Warren, S.G. and Brandt, R.E. (2008): Optical constants of ice from the ultraviolet to the microwave: a revised compilation. Journal of Geophysical Research, 113, D14220.

Wen, B., Tsang, L., Winebrenner, D.P. and Ishimaru, A. (1990): Dense medium radiative transfer theory: comparison with experiment and application to microwave remote sensing and polarimetry. IEEE Transactions on Geoscience and Remote Sensing, 28 (1), 46-59.

West, R., Tsang, L. and Winebrenner, D.P. (1993): Dense medium radiative transfer theory for two scattering layers with a Rayleigh distribution of particle sizes. IEEE Transactions on Geoscience and Remote Sensing, 31 (2), 426-437.

WGMS (1989): World glacier inventory - Status 1988. In: Haeberli, W., Bösch, H., Scherler, K., Østrem, G. and Wallén, C. C. (eds.), IAHS (ICSI) / UNEP / UNESCO, World Glacier Monitoring Service, Zurich, Switzerland: 458 pp.

Wilson, J. and Gallant, J. (2000): Terrain Analysis, Principles and Applications, John Wiley & Sons, Inc., New York.

Wingham, D.J., Rapley, C.G. and Griffiths, H. (1986): New techniques in satellite altimeter tracking systems, Proc. IGARSS'86, 1, 185-190.

Wingham, D.J. (1995): The limiting resolution of ice-sheet elevations derived from pulse-limited satellite altimetry. Journal of Glaciology, 41 (138), 413-422.

Wingham, D.J., Ridout, A.J., Scharroo, R., Arthern, R.J. and Shum, CK. (1998): Antarctic elevation change from 1992 to 1996. Science, 282, 456-458.

Zemp, M., Paul, F., Hoelzle, M. and Haeberli, W. (2008): Alpine glacier fluctuations 1850-2000: An overview and spatio-temporal analysis of available data and its representativity. In: Orlove, B., Wiegandt, E. and Luckman, B. (eds.): Darkening Peaks: Glacier Retreat, Science, and Society. University of California Press, Berkeley and Los Angeles, 152-167.

Wu, Q. X. (1995): A correlation-relaxation-labelling framework for computing optical flow-Template matching from a new perspective. IEEE Transactions on Pattern Analysis and Machine Intelligence, 17, 843-853.

Zappa, M. and Kan, C. (2007): Extreme heat and runoff extremes in the Swiss Alps. Natural Hazards and Earth System Sciences, 7, 375-389.

Zebker, H.A. and Villasenor, J. (1992): Decorrelation in interferometric radar echos. IEEE Transactions on Geoscience and Remote Sensing, 30(5), 950-959.

Zlotnicki, V., Fu, L.L. and Patzert, W. (1989): Seasonal variability in global sea level observed with Geosat altimetry. Journal of Geophysical Research, 94, C12, 17959-18237.

Zwally, H.J., Brenner, A.C., Major, J.A., Bindschadler, R.A. and Marsh, J.G. (1989): Growth of Greenland Ice-Sheet - Measurement. Science, 246, 1587-1589.

Zwally, H.J., Schutz, B., Abdalati, W., Absihre, J., Bentley, C., Brenner, A., et al. (2002): ICESat's lasar measurements of polar ice, atmosphere, ocean and land. Journal of Geodynamics, 34, 405-445.

Zwally, H., Schutz, R., Bentley, C., Bufton, J., Herring, T., Minster, J., Spinhirne, J. and Thomas, R. (2010a): GLAS/ICESat L2 Global ElevationData V031, Febuary 2003 to November 2009, Digital Media.

Zwally, H., Schutz, R., Bentley, C., Bufton, J., Herring, T., Minster, J., Spinhirne, J. and Thomas., R. (2010b): GLAS/ICESat L2 Global Land Surface Altimetry Data V531, Febuary 2003 to November 2009, Digital Media.

Abbreviations

ALOS	Advanced Land Observing Satellite
AOI	Area Of Interest
ASAR	Advanced SAR
ASTER	Advanced Spaceborne Thermal Emission and Reflection radiometer
CC	Correlation Coefficient
CCF	Cross Correlation in the Frequency domain
CGIAR	The Consultative Group on International Agricultural Research
CRL	Correlation Relaxation Labelling
GCP	Ground Control Point
GIS	Geographic Information System
GLIMS	Global Land Ice Measurements from Space
GNSS	Global Navigation Satellite System
GTN-G	Global Terrestrial Networks - Glaciers
DARD	Data Access Requirement Document
DEM	Digital Elevation Model
DInSAR	Differential InSAR
DMRT	Dense Medium Radiative Transfer
DN	Digital Number
DOS	Dark Object Subtraction
ECV	Essential Climate Variable
ERS	European Remote-sensing Satellite
ETM+	Enhanced Thematic Mapper plus
FCDR	Fundamental Climate Data Record
InSAR	Interferometric repeat-pass SAR
kHz	kilo Hertz
LIDAR	Laser Detection and Ranging
LOS	Line Of Sight
LRM	Low Resolution Mode
NED	National DEM
NCC	Normailized Cross-Correlation
NIR	Near-InfraRed part of the electromagnetic spectrum
NDSI	Normalized Difference Snow Index
NDVI	Normalized Difference Vegetation Index
PALSAR	Phased Array type L-band SAR

PCA	Principle Component Analysis
PSD	Product Specifications Document
RADAR	Radio Detection And Ranging
RGB	Red Green Blue
RMSE	Root Mean Square Error
RSS	Root Sum of Squares
SAR	Synthetic Aperture Radar
SB-SAR	Satellite-Borne repeat pass SAR
SNR	Signal-to-Noise Ratio
SPOT	System Pour l'Observation de la Terre
SRTM	Shuttle Radar Topography Mission
SWIR	Short Wave InfraRed
THz	Tera Hertz
TOA	Top of Atmosphere
TM	Thematic Mapper
URD	User Requirement Document
USGS	United States Geological Survey
UTM	Universal Transverse Mercator
VIS	VISible part of the electromagnetic spectrum
VNIR	Visible to Near-InfraRed part of the electromagnetic spectrum
WGI	World Glacier Inventory
WGMS	World Glacier Monitoring Service

Deleted:

The Ice, Cloud and land Elevation Satellite (ICESat) carrying the Geoscience Laser Altimeter System (GLAS) was launched in 2003. The acquisition strategy was reduced because of the abrupt failure of the first of three lasers. However, the mission surpassed the initial goal of a three year campaign by two years and it acquired nearly 2 billion elevation points before failure of the final laser in October 2009 (cci_del23_atbdv0_111201fp.dochttp://icesat.gsfc.nasa.gov). ICESat contained three lasers, each with two telescopes one infra-red (1024 nanometers) and one visible green (532 nanometers) for the land surface and atmosphere, respectively. The laser pulses at 40 Hz which translates into a separation distance on Earth's surface of ~170 m between each footprint. ICESat averaged 2-3 acquisitions per year repeating similar reference tracks within a few hundred metres in the arctic. The amount of data is also much larger in the arctic as compared to the equator due to the polar orbiting strategy of the satellite. Full details of the ICESat mission can be found in Zwally et al. (2002) and Schutz et al. (2005).